Title
Magnetotransport in Two-Dimensional Materials

Permalink
https://escholarship.org/uc/item/99j8d291

Author
Shi, Yanmeng

Publication Date
2016

Peer reviewed|Thesis/dissertation

UNIVERSITY OF CALIFORNIA
RIVERSIDE

Magnetotransport in Two-Dimensional Materials

A Dissertation submitted in partial satisfaction
of the requirements for the degree of

Doctor of Philosophy

in

Physics

by

Yanmeng Shi

December 2016

Dissertation Committee:

    Dr. Chun Ning Lau, Chairperson
    Dr. Shan-Wen Tsai
    Dr. Nathaniel Gabor

The Dissertation of Yanmeng Shi is approved:

_____

_____

_____
                                    Committee Chairperson

University of California, Riverside

Acknowledgments

Five years is not a short period of time; yet after five years at UCR and this research group, they still feel fresh to me, as I have learned new things every day during the pursuit of my physics PhD. Five years ago, I was struggling to build my first usable device and scratching my head trying to figure out the mysterious gate leakage problem occurring on my every single device. Looking back, I feel fortunate to have joined UCR and professor Jeanie Lau's research group, where I made the phase transition from a student to an independent researcher, which would be impossible without the help and support of many people.

First and foremost, I owe a great deal of gratitude to my research advisor, professor Jeanie Lau. It is my honor to work with and for her. She is not only my research mentor, but also a role model for me. She is always respectful and patient to every student in her group. Even for simple physics questions, she always gives detailed explanation. I acknowledge her for her five-year support and help on my projects. I benefited from every discussion with her. Every time she went to the lab and talked about my experiment, I made some progress. Without her guidance, I could not have accomplished the works that I am proud of. I also thank her for keeping a friendly and creative environment in her group. In particular, I thank Jeanie for her understanding, advice and support for my special situation when graduation approaches. Most importantly, I thank her teaching me the "good taste" of science.

I feel fortunate that I have met so many nice and knowledgeable professors in UCR. I thank Dr. Bipin Desai, Dr. Chandra Varma, Dr. Ernest Ma, Dr. Shan-Wen Tsai,

Dr. Vivek Aji, Dr. Roya Zandi, Dr. Marc Bockrath for the physics lectures they gave. In particular, I thank Dr. Shan-Wen Tsai and Dr. Nathaniel Gabor for their precious time to serve as members of my defense committee.

I'm very grateful that I have met so many friendly and helpful group members in Jeanie's group. I benefited a lot from former group members. I acknowledge Dr. Hang Zhang, Dr. Lei Jing, Dr. Zeng Zhao, Dr. Fenglin Wang for their help of my experiments. In particular, I would like to thank Dr. Jhao-Wun Huang for teaching me fabrication techniques when I joined the group. Special thanks to Dr. Yongjin Lee, who made significant contributions to the bilayer graphene paper published in *Physical Review Letters*, and taught me current annealing and measurement techniques. The trips to Tallahassee with him were very pleasant. I have learned form him not only experimental knowledge, but also enthusiasm for physics.

I am also thankful to our current group members, Kevin Myhro, Petr Stepanov, Son Tran, Jiawei Yang, Yulu Liu and Dmitry Shcherbakov for their help. I would like to acknowledge Nathaniel Gillgren, who is co-first author of the phosphorene paper, which was published in *2D Materials*. Nate is not just a good collaborator, but also a great friend. Special thanks to Shi Che, who has made great contributions to the bi- and tetra-layer graphene projects. Shi is very helpful and productive, and has a good grasp of physics. The time working with him benefited me a lot. I also thank our postdoc, Dr. Ruoyu Chen, who joined the group recently. Though I have only worked with him for a few months, I learned much from his insight of physics and experience in the lab. I also would like to thank all

the undergraduate students Ziqi Pi, Timothy Espiritu, Jason Wu, who worked with me and provided nice graphene and boron nitride flakes.

I want to thank our collaborators, in particular, Dr. Dmitry Smirnov at National High Magnetic Field Laboratory for his valuable assistance during our visits there, Dr. Fan Zhang at University of Texas Dallas for his theoretical support on bilayer graphene, Dr. Roger Lake and his student Supeng Ge for their theoretical calculations of tetralayer graphene, and Dr. Yafis Barlas for his help to understand the data of tetralayer graphene. I also thank Dr. Jing Shi and his student Dr. Zhiyong Wang for providing us single crystal material Bi_2Se_3.

I also feel fortunate that I met so many friendly and helpful classmates and friends here during my PhD life: Shaolong Chen, Weimin Zhou, Chi Tang, Zhisheng Lin, Yi Wu, Yadong Xu, Changtao Hou, Supeng Ge, Shanshan Su, Dr. Bin Cheng, Dr. Cheng Pan, Dr. Yong Wu, Dr. Peng Wang, Dr. Tengfei Miao and many others. Special thanks to Yadong and Changtao for being nice roommates.

Lastly, but most importantly, I am grateful to my parents and brothers for their love and support through my entire life. Special thanks to my wife, Shang Li, for her understanding and support as I pursue my dreams.

To my parents.

ABSTRACT OF THE DISSERTATION

Magnetotransport in Two-Dimensional Materials

by

Yanmeng Shi

Doctor of Philosophy, Graduate Program in Physics
University of California, Riverside, December 2016
Dr. Chun Ning Lau, Chairperson

The study of two-dimensional (2D) materials began with the seminal work of experimental isolation and fabrication of monolayer graphene field-effect transistors by the Manchester group in 2004, and has remained one of the frontiers of condensed matter physics ever since. Mono- and few-layer graphene, which host chiral charge carriers with competing symmetries (valley, spin and orbital), have proved to be fascinating platforms for investigating the quantum Hall (QH) physics. Research efforts were soon extended to other 2D materials such as transition metal dicalcogenides (TMD). One such material is phosphorene (mono- or few-layer black phosphorous), which has attracted much attention due to its large direct band gap and high mobility. This thesis describes our comprehensive transport studies of bi- and tetra-layer graphene, as well as few-layer phosphorene (FLP).

By fabricating devices that are either suspended or encapsulated within hexagonal boron nitride (hBN) layers, we are able to reduce disorders and achieve high quality devices. In suspended bilayer graphene (BLG) devices, we observe both integer and fractional QH states. The interplay between symmetries and electric and magnetic fields gives rise to two

distinct phases of the QH state at filling factor $\nu = 1$, with different pseudospin and real spin polarizations, and different energy gaps. Moreover, the $\nu = 2/3$ fractional QH state and a feature at $\nu = 1/2$ are only resolved at finite electric field and large magnetic field. These findings provide insight into the competing symmetries in BLG.

We also present our transport studies of hBN-encapsulated tetralayer graphene devices, of which the band structure can be decomposed into two BLG-like bands. Unlike mono-, bi- and tri-layer graphene, which display sharp resistance peaks at the charge neutrality point (CNP), we observe a local resistance minimum at the CNP, flanked by three resistance peaks at higher charge densities. Such non-monotonic dependence on density is attributed to the trigonal warping that induces Lifshitz transitions as a function of charge density and electric field. In the QH regime, we observe rich Landau level (LL) crossing patterns between the two BLG-like bands. A perpendicular electric field breaks the inversion symmetry of tetralayer graphene, lifting the valley degeneracy of the LLs. By fitting the calculated LL spectra to the crossing features in our experimental data, we are able to obtain the values of hopping parameters and determine the symmetries of the LLs. These works provide us with the insight of the band structure of tetralayer graphene, the effects of remote hopping terms, as well as the importance of the interplay between competing symmetries and applied electric and magnetic fields.

Finally, in hBN-encapsulated FLP devices, we report the observations of weak localization (WL), from which the dephasing lengths could be extracted to be $\sim 30-100$ nm, and exhibit power-law dependences on temperature and charge density. We conclude that

the dominant source of phase-relaxation is the electron-electron interactions, shedding light onto the understanding of the scattering mechanisms in FLP devices at low temperatures.

The studies of 2D materials constitute one of the most active frontiers of condensed matter research. Our results provide insight into the quantum transport properties of the 2D electron gas (2DEG) systems in Bernal-stacked bi- and tetra-layer graphene and FLP devices. The techniques of fabricating high quality devices enable us to explore other 2D materials as well. Novel physical phenomena such as the QH effect in few-layer graphene with other stacking orders, *e.g.* rhombohedral-stacking order, need further experimental studies. The integer and fractional QH effect in FLP devices await further explorations as well.

Contents

List of Figures

List of Tables

Chapter 1

The Rise of Graphene and Beyond-graphene Two-dimensional Materials

1.1 A brief history of graphene

Carbon, the 15th most abundant element in the earth's crust, exists in many allotrope forms: diamond, graphite, fullerene (C_{60}), carbon natotube and so on [2]. The newest member, graphene, which consists of a single layer of carbon atoms arranged in a honeycomb lattice structure, is a single atomic layer of graphite. It has been presumed to be unstable against thermal fluctuations, thus does not exist in a free state [3]. Graphene could serve as a two-dimensional (2D) building block for other carbon allotropes [1]: it can be wrapped to form a zero-dimensional (0D) C_{60}, rolled up to form a one-dimensional (1D)
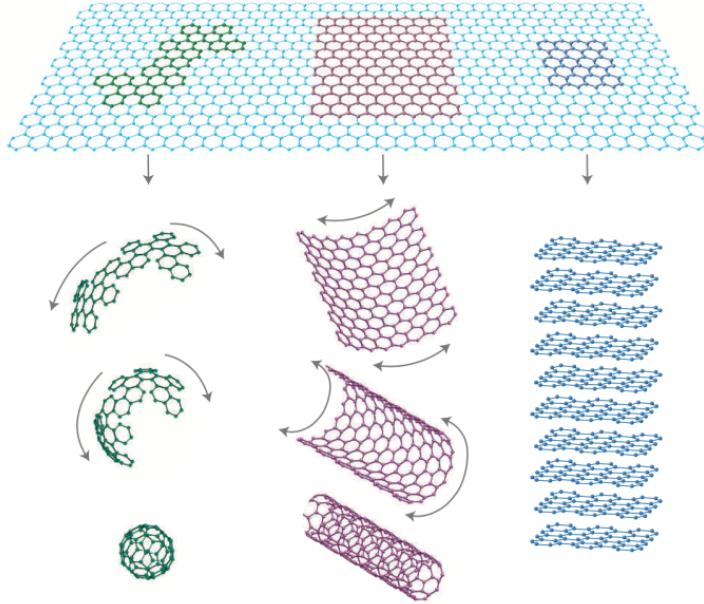
Figure 1.1: Schematic of graphene building C$_{60}$, carbon nanotube and 3D graphite. Image adapted from Ref. [1]

nanotude, or stacked up to form a three-dimensional (3D) graphite (Fig. 1.1). The band structure of single-layer graphene was first calculated using the tight binding theory in 1947 by P.R. Wallace as a toy model to study the properties of graphite [4]. Later, the model of graphene has been used for the theoretical study of the electronic properties of carbon nanotubes and was hugely successful [5].

After the discovery of carbon nanotubes in 1991 [6], the research community has attempted to isolate graphene experimentally. In 2004, the seminal work from the group of A. Geim and K. Novoselov at the University of Manchester titled "*Electric Field Effect in Atomically Thin Carbon Films*" was published in *Science*, reporting graphene-based field-effect transistors [3]. This work was the first to report the isolation of single-layer graphene on insulating substrates and its transport properties. Surprisingly, this amazing

experiment feat was achieved by using a piece of scotch tape to exfoliate bulk graphite onto Si/SiO$_2$ substrates and an optical microscope to identify the number of layers through optical contrast. These techniques are simple and cheap, compared to the advanced growth of conventional 2D electron gas (2DEG) systems based on GaAs/AlGaAs semiconductor heterostructures.

In 2005, two groups from the University of Manchester and Columbia University independently reported the observations of the unconventional (so called "half-integer") quantum Hall effect (QHE) in graphene, which revealed its linear energy dispersion, and demonstrated its true 2D nature [7, 8]. Since then, the field of graphene research has undergone explosive growth. For instance, researchers have demonstrated that graphene affords superior electronic properties compared to the conventional 2DEG systems, due to its linear energy dispersion, ambipolar transport behavior and high mobility up to 1×10^6 cm^2/Vs that enables the observations of unconventional integer [7, 8] and fractional QHE [9–11]. Moreover, graphene's compelling material properties, $e.g.$ high optical transparency [12], high mechanical strength [13] and high thermal conductivity [14] etc., render it an ideal platform for the optical, scanned probe, mechanical and thermal measurements and applications.

1.2   Introduction to black phosphorous

After the isolation of graphene, tremendous efforts were focused on its potential to replace silicon in electronic applications. However, due to its gapless energy dispersion, graphene is not directly suitable for digital electronics. Researchers soon started to explore
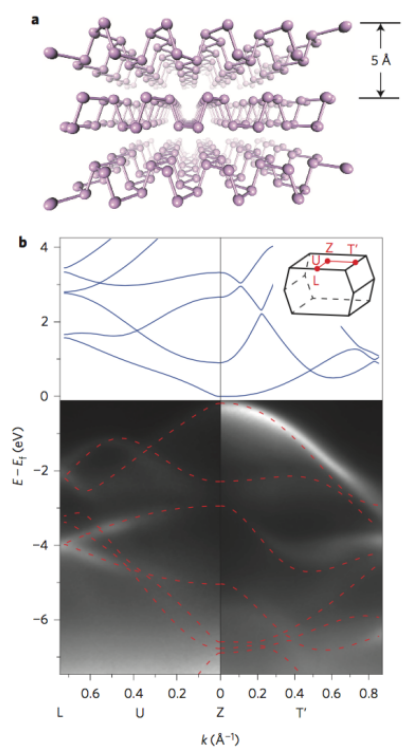
Figure 1.2: (a) Crystal structure of black phosphorous. (b) Band structure of black phosphorous mapped by angle-resolved photoemeission spectroscopy. Image adapted from Ref. [15]

other 2D materials such as transition metal dicalcogenides (TMD), *e.g.* MoS_2, WS_2, etc. [16].

One of the latest additions to the family of 2D materials is phosphorene, which is single- or few-atomic-layer black phosphorus (BP) [15]. BP is the most stable allotrope of elemental phosphorus, consisting of layers held together by weak van der Waals forces. Within each layer, the phosphorus atoms are arranged in a puckered structure (Fig. 1.2a). It has recently piqued the interest of the scientific community due to its high mobility [17], direct band gap that is tunable by thickness or strain [17–23], and large in-plane anisotropy [23,24]. Unlike graphene, single-layer phosphorene is a semiconductor with a direct bandgap ~ 2 eV; with each added layer, the gap is reduced, eventually reaching ~ 0.3 eV [21] in the bulk limit (Fig. 1.2b). The direct band gap and high mobility make BP a highly attractive candidate for electronic, thermal and optoelectronic applications, as well as a model system for interesting physics such as the QHE [25] and emergence of topological orders under a large electric field [26, 27].

Using the same scotch tape method, phosphorene can be exfoliated by peeling thin flakes form bulk crystal and transferred onto substrates. The first generation of few-layer phosphorene (FLP) devices were fabricated on Si/SiO_2 substrates, with reported hole mobility $\sim 300 - 1000$ cm^2/Vs [15]. Recent experiments have pushed the charge carrier mobility up to $\sim 45,000$ cm^2/Vs at low temperatures by using hexagonal boron nitride (hBN) as substrates, enabling the observations of Shubnikov-de Haas oscillation [25, 28, 29], and more recently the QHE [25].

1.3 Thesis outline

Over the past 5 years, I have worked on the electronic transport studies of 2D materials including graphene and FLP. The thesis is organized as follows. Chapter 2 describes the tight binding model and its applications to calculate the band structures of mono-, bi- and tetra-layer graphene. The quantum corrections to the classical transport, including weak localization, Shubnikov-de Haas oscillation and the QHE, will also be briefly introduced. Chapter 3 discusses the methods of device fabrication, including the techniques to fabricate dual-gated suspended graphene devices, and graphene and FLP devices that are encapsulated between hBN sheets. Chapter 4 presents our work on dual-gated suspended bilayer graphene (BLG) devices. In high quality suspended BLG devices, we observe two distinct phases of the QH state at filling factor $\nu = 1$: a layer polarized state that has a larger energy gap, and a layer coherent state with a smaller energy gap. The $\nu = 2/3$ fractional QH state as well as a feature at $\nu = 1/2$ are only resolved at finite electric field and large magnetic field. The work on hBN-encapsulated tetralayer graphene devices will be discussed in chapter 5, where we report the observations of trigonal warping in tetralayer graphene, and rich Landau level (LL) crossings between two BLG-like bands with different effective masses. We also obtain the hopping parameters by computing the LL spectra and comparing with the experimental data. In chapter 6, I will present our wok on hBN-encapsulated FLP devices. From weak localization, we extract the dephasing lengths, which exhibit power-law dependence on temperature and charge density. Finally, in chapter 7, I will summarize the thesis with a brief conclusion and outlook for future work.

Chapter 2

The Tight Binding Calculations of Graphene and Quantum Transport

In this chapter, I will describe the theoretical background of my projects. This chapter starts with a brief introduction of the tight binding model, followed by its applications to mono-, bi-, and tetra-layer graphene. Subsequently, I will discuss the concept of weak localization, which is a quantum correction to the classical conductivity due to the wave nature of quantum particles, and the quantum Hall effect (QHE).

2.1 The tight binding model

The tight binding (TB) method [30,31] is a widely-used technique to calculate the electronic band structures of crystals. Its underlying assumption is that electrons in crystals are tightly bound to the atoms, hence the name *tight binding*. Under this assumption, an electron is only affected by the potential of its original atom, and the potential due to all

other atoms in the crystal is very small and can be considered as a perturbation. Therefore, the wave function of electrons can be expressed as a superposition of the electronic wave functions of each isolated atom located on the lattice sites. Interactions between electrons are neglected. Despite its simplicity, TB method is very powerful for understanding single particle phenomena in condensed matter material, and has been proven to be a good starting point even for a strong correlated system.

Let's consider a crystal with total N unit cells. In each unit cell, there are M atomic orbitals ϕ_m, where $m = 1, 2, \ldots M$. For isolated atoms, these are s, p, d, f etc. orbitals. The Bloch wave at given $\mathbf{k}$ and $\mathbf{r}$ can be expanded based on these atomic orbitals

$$\Phi_m(\mathbf{k}, \mathbf{r}) = \frac{1}{\sqrt{N}} \sum_{i=1}^{N} e^{i\mathbf{k}\cdot\mathbf{R}_{mi}} \phi_m(\mathbf{r} - \mathbf{R}_{mi}) \tag{2.1}$$

where N is the total number of unit cells in the crystal, i denotes the ith unit cell. $\mathbf{R}_{mi}$ is the positional vector of mth orbital in the ith unit cell.

A more general electronic wave function can be expressed as a linear superposition of the Bloch wave functions

$$\Psi_j(\mathbf{k}, \mathbf{r}) = \sum_{m=1}^{M} a_{jm} \Phi_m(\mathbf{k}, \mathbf{r}) \tag{2.2}$$

where a_{jm} is the expansion coefficient. There are a total of M different energy bands. The energy of the jth band E_j can be calculated by

$$E_j(\mathbf{k}) = \frac{<\Psi_j|H|\Psi_j>}{<\Psi_j|\Psi_j>} \tag{2.3}$$

where H is the Hamiltonian. By substituting equation 2.2, it gives

$$E_j(\mathbf{k}) = \frac{\sum_{p,q}^{M} a_{jp}^* a_{jq}^* <\Phi_p|H|\Phi_q>}{\sum_{p,q}^{M} a_{jp}^* a_{jq}^* <\Phi_p|\Phi_q>} \tag{2.4}$$

This equation leads to the generalized eigenvalue equation

$$Ha_j = E_j Sa_j \tag{2.5}$$

where H and S are transfer integral matrix and overlap integral matrix, respectively. The elements of these two matrices are defined by

$$H_{pq} = <\Phi_p|H|\Phi_q>, \quad S_{pq} = <\Phi_p|\Phi_q> \tag{2.6}$$

The band energies E_j can be determined by solving the secular equation

$$det(H - E_j S) = 0 \tag{2.7}$$

where det denotes the determinant of the matrix. The number of solutions is M, which is the total number of atomic orbitals in each unit cell.

2.2 Electronic properties of graphene

2.2.1 Monolayer graphene

Each monolayer graphene (MLG) consists of carbon atoms in a honeycomb lattice [3]. Each carbon atom has six electrons: two core electrons, and four valance electrons that occupy $2s$, $2p_x$, $2p_y$, $2p_z$ orbitals. Interestingly, the $2s$, $2p_x$, $2p_y$ orbitals are sp^2 hybridized to form robust σ bonds with the nearest neighbors in the graphene plane. The remaining $2p_z$ orbital oriented perpendicular to the MLG plane forms π bonds with the adjacent carbon atoms, and determines the electronic properties of MLG in the low energy regime.

The honeycomb lattice consists of two identical sublattices [4], labeled as sublattice A and sublattice B, as indicated by the blue and red circles, respectively, in Fig. 2.1a. The

9
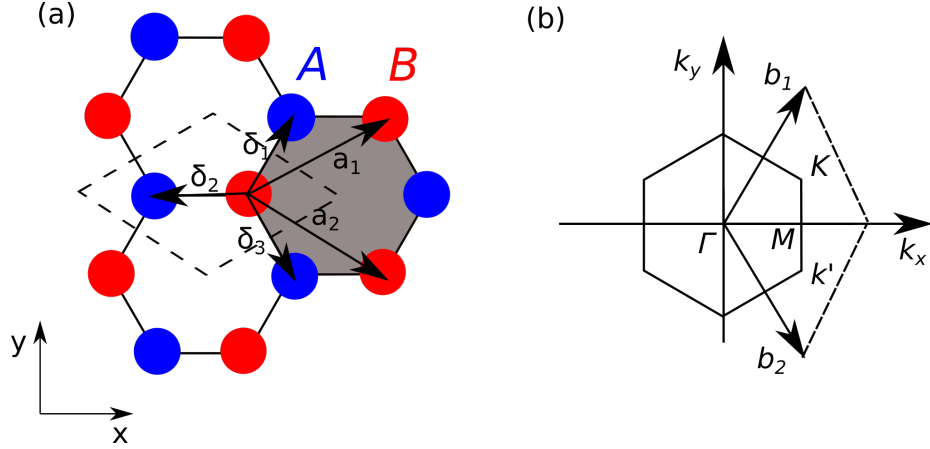
Figure 2.1: Crystal structure and BZ of MLG. (a) The honeycomb lattice of monolayer graphene in real space. Sublattices A and B are indicated by blue and red circles, respectively. (b) Reciprocal lattice of MLG. Γ, K and M are high symmetry points.

primitive lattice vectors are defined as

$$\vec{a_1} = (\frac{\sqrt{3}a}{2}, \frac{a}{2}), \quad \vec{a_2} = (\frac{\sqrt{3}a}{2}, -\frac{a}{2}) \tag{2.8}$$

where a is the lattice constant. The distance between two nearest carbon atoms in graphene is a_{c-c}=1.42 Å [31], and $a = a_{c-c} \times \sqrt{3} = 2.46$ Å. A unit cell is indicated by the dashed rhombus in Fig. 2.1a, and consists of two atoms, atom A and atom B. As shown in Fig. 2.1b, the reciprocal lattice vectors are calculated to be

$$\vec{b_1} = \frac{2\pi}{a}(\frac{1}{\sqrt{3}}, 1), \quad \vec{b_2} = \frac{2\pi}{a}(\frac{1}{\sqrt{3}}, -1) \tag{2.9}$$

The Brillouin zone (BZ) of MLG is shown in Fig. 2.1b. The corners of the BZ are known as K and K', often referred to as the Dirac points. In pristine graphene, the Fermi energy is at the Dirac points.

The band structure of MLG can be calculated via the TB method, as introduced in section 2.1 [4]. In the case of MLG, we consider two atomic orbitals per unit cell, which

are $2p_z$'s from atom A and atom B. The atomic orbitals are labeled as ϕ_A and ϕ_B. By substituting into the equation 2.6, we obtain the diagonal elements of H

$$H_{AA} = \epsilon = \frac{1}{N} \sum_{i=1}^{N} < \phi_A(r - R_{Ai})|H|\phi_A(r - R_{Ai}) > \tag{2.10}$$

and $H_{AA} = H_{BB}$ since these two sublattices are identical.

The off-diagonal elements of the transfer integral matrix H represent the hopping energies between orbitals in A and B lattice sites, and if only the nearest neighbors are considered, they can be written as

$$H_{AB} = H_{BA}^* = \frac{1}{N} \sum_{i=1}^{N} \sum_{l=1}^{3} e^{i\mathbf{k}\cdot\boldsymbol{\delta}_l} < \phi_A(\mathbf{r} - \mathbf{R}_{Ai})|H|\phi_B(\mathbf{r} - \mathbf{R}_{Ai} - \boldsymbol{\delta}_l) > \tag{2.11}$$

where $\boldsymbol{\delta}_l$ are positional vectors of the nearest $B(A)$ atoms relative to $A(B)$ atoms as shown in Fig. 2.1a. They are defined as

$$\boldsymbol{\delta}_1 = (\frac{a}{2\sqrt{3}}, \frac{a}{2}), \quad \boldsymbol{\delta}_2 = (\frac{a}{2\sqrt{3}}, -\frac{a}{2}), \quad \boldsymbol{\delta}_3 = (-\frac{a}{\sqrt{3}}, 0) \tag{2.12}$$

H_{AB} can be simplified as $H_{AB} = -\gamma_0 f(\mathbf{k})$ where the hopping parameter is defined as $\gamma_0 = < \phi_A|H|\phi_B >$ and for graphene it is ~ 3 eV. The nearest hopping function $f(\mathbf{k})$ is defined as $f(\mathbf{k}) = \sum_{l=1}^{3} e^{i\mathbf{k}\cdot\boldsymbol{\delta}_l}$. Similarly, we can obtain the elements of the overlap integral matrix S: $S_{AA} = S_{BB} = 1$, $S_{AB} = S_{BA}^* = s_0 f(\mathbf{k})$, where $s_0 = < \phi_A|\phi_B >$ describes the probability of non-zero overlap between the nearest lattice sites and is ~ 0.129 for MLG.

Therefore, the matrices H and S can be written as

$$H = \begin{pmatrix} \epsilon & -\gamma_0 f(\mathbf{k}) \\ -\gamma_0 f^*(\mathbf{k}) & \epsilon \end{pmatrix}, \quad S = \begin{pmatrix} 1 & s_0 f(\mathbf{k}) \\ s_0 f^*(\mathbf{k}) & 1 \end{pmatrix} \tag{2.13}$$

where $\epsilon = 0$ for intrinsic MLG. By solving the secular equation 2.7, the eigenvalues are

$$E_\pm = \frac{\pm\gamma_0|f(\mathbf{k})|}{1 \mp s_0|f(\mathbf{k})|} \tag{2.14}$$

11

where E_+ and E_- correspond to the conduction band and valance band, respectively.

At the Dirac points, function $f(\mathbf{k})$ is zero. These two K points, also referred to as valleys, are the crossing points between the conduction and valance bands. At these points, the energy eigenvalues are degenerate. In the low energy regime, S_{AB} can be ignored, therefore the effective Hamiltonian H can be written as

$$H_\xi = v_F \begin{pmatrix} 0 & \xi p_x - ip_y \\ \xi p_x + ip_y & 0 \end{pmatrix} \tag{2.15}$$

where the index $\xi = \pm 1$ denotes the valleys, yielding the eigenvalues

$$E_\pm \approx \pm v_F |\mathbf{q}| \tag{2.16}$$

where $\mathbf{q} = \mathbf{K} - \mathbf{k}$. v_F is the Fermi velocity $v_F = \frac{\sqrt{3}a\gamma_0}{2\hbar} \approx 1 \times 10^6 \mathrm{m/s}$. Therefore, close to the Dirac points, the energy has a linear dispersion with momentum, and electrons travel at an effective speed of light v_F.

If we look at the equation 2.15 more closely, it is analogous to the Dirac equation with using Pauli spin matrices in sublattices A and B. Therefore, it is useful to introduce the concept of pseudospin [31]. If all charges are located on sublattice A, then it could be viewed as a pseudospin "up" state; while if all charges located on sublattice B, then it could be viewed as a pseudospin "down" state. In general, however, the charge state is a superposition of "up" and "down" states, similar to real spin. In this case, pseudospin is another quantum number for graphene.
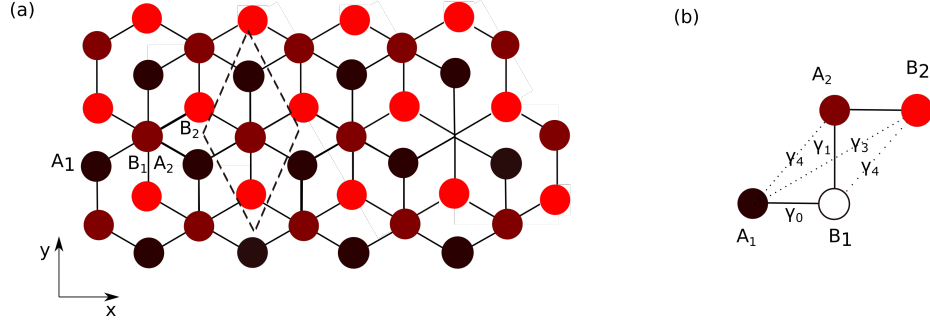
Figure 2.2: Crystal structure of BLG. (a) Top view of the honeycomb lattice of bilayer graphene in real space. Sublattice A_1 from bottom layer is labeled as black circles, the dimer sites B_1 from the bottom layer and A_2 from the top layer as brown circles, sublattice B_2 from top layer as red circles. (b) A unit cell of BLG. Dashed lines indicate the hopping between interlayer atoms. γ_0 is the hopping energy between the sublattice atoms in the same layer. γ_1 is the interlayer hopping within the dimer bonds.

2.2.2 Bernal-stacked bilayer graphene

Bilayer graphene (BLG) consists of two MLG sheets. In Bernal-stacked BLG, the atoms are arranged so that one sublattice atom from the top layer is located right in the center of the hexagon of the bottom layer, while the other sublattice atom from the top layer is located exactly on the atom from the bottom layer [31]. As shown in Fig. 2.2a, atoms A_1 (black) and B_1 are from the bottom layer. Atoms A_2 and B_2 (red) are from the top layer. Atom A_2 stacks right on top of atom B_1, forming *dimerbonds*. Each unit cell in BLG consists of these four atoms. The dashed rhombus in Fig. 2.2a indicates a unit cell of BLG, which is shown in the cross-sectional view in Fig. 2.2b

By repeating the same procedure for MLG, and only considering the hopping terms between the nearest intralayer and interlayer atoms, we can obtain the transfer integral

13

matrix

$$
H = \begin{pmatrix} \epsilon_{A_1} & -\gamma_0 f(\mathbf{k}) & 0 & 0 \\ -\gamma_0 f^*(\mathbf{k}) & \epsilon_{B_1} & \gamma_1 & 0 \\ 0 & \gamma_1 & \epsilon_{A_2} & -\gamma_0 f(\mathbf{k}) \\ 0 & 0 & -\gamma_0 f^*(\mathbf{k}) & \epsilon_{B_2} \end{pmatrix} \tag{2.17}
$$

where $\gamma_0 = <\phi_{A_1}|H|\phi_{B_1}> = <\phi_{A_2}|H|\phi_{B_2}>$ is the hopping energy between intralayer sublattice atoms, $\gamma_1 = <\phi_{B_1}|H|\phi_{A_2}>$ the hopping energy between the nearest interlayer atoms B_1 and A_2. In the low energy regime, we can approximate the overlap integral matrix to be an identity matrix since the overlap probability is small, and approximate $\epsilon_{A_1} = \epsilon_{B_1} = \epsilon_{A_2} = \epsilon_{B_2} = 0$. By solving the secular equation, we can obtain the eigenvalues of the bands

$$
E_{\pm}^{\alpha} = \pm \frac{\gamma_1}{2} \left(\sqrt{1 + \frac{4\gamma_0^2 |f(\mathbf{k})|^2}{\gamma_1^2}} + \alpha \right) \tag{2.18}
$$

where the $+$ and $-$ signs refer to the conduction and valance bands, respectively, the $\alpha = \pm 1$ denotes the higher and lower energy bands. At the K points, $f(\mathbf{k})$ is zero. For the lower energy band, when $\alpha = $ -1, $E_{\pm} = 0$. For the higher band, $\alpha = $1, $E_{\pm} = \pm\gamma_1$, and is separated from the lower bands by γ_1 due to the hopping term within the dimer bonds, *i.e.* between B_1 and A_2. In principle, one can also consider remoter hopping terms, such as γ_4 between the dimer and non-dimer atoms, and γ_3 between the non-dimer atoms, as shown in Fig. 2.2b. However, the effects of these terms are small and are often ignored. Fig. 2.3 shows the low energy bands of BLG. The conduction and valance bands touch at the K points. Different from MLG, BLG has a parabolic energy dispersion near the K points.
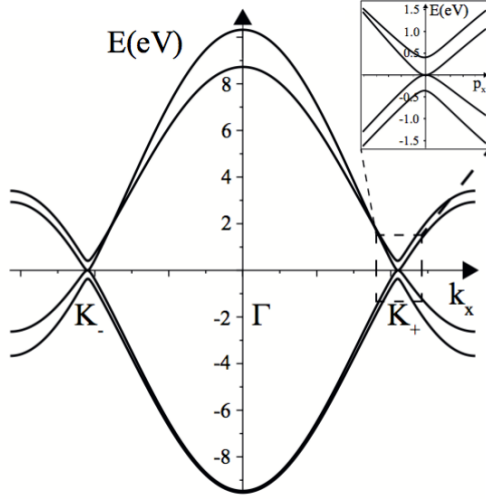
Figure 2.3: Low energy bands of BLG by tight binding calculation with the parameters: $\gamma_0 = 3.033$ev, $\gamma_1 = 0.381$ev at k_y=0. $K_{\pm}$ are the Dirac points. Image adapted from Ref. [31].

For both MLG and BLG, the conduction and valance bands touch at the K points due to the inversion symmetry, leading to gapless band structures. In BLG, the higher energy bands originate from the dimer sites, and the lower energy bands, which are relevant for the transport experiments, arise from the atoms A_1 and B_2. In this case, the valley symmetry is roughly equivalent to the layer symmetry for BLG in the low energy regime. Therefore, applying an out-of-plane electric field $E_{\perp}$ breaks the layer symmetry, and hence the valley symmetry, thus opens an energy gap at the K points.

The opening of the band gap can be confirmed by the TB calculation. Under a perpendicular electric field, the atoms from the top layer and the bottom layer have an

energy difference $\triangle$. Therefore, the effective Hamiltonian can be written as

$$
H = \begin{pmatrix}
\frac{\triangle}{2} & -\gamma_0 f(\mathbf{k}) & 0 & 0 \\
-\gamma_0 f^*(\mathbf{k}) & \frac{\triangle}{2} & \gamma_1 & 0 \\
0 & \gamma_1 & -\frac{\triangle}{2} & -\gamma_0 f(\mathbf{k}) \\
0 & 0 & -\gamma_0 f^*(\mathbf{k}) & -\frac{\triangle}{2}
\end{pmatrix}
\tag{2.19}
$$

where $\epsilon_{A_1} = \epsilon_{B_1} = \frac{\triangle}{2}$ and $\epsilon_{A_2} = \epsilon_{B_2} = -\frac{\triangle}{2}$. The eigenvalues of the secular equation are

$$
E_{\pm}^{\alpha} = \pm \left(\frac{\triangle^2}{4} + \gamma_0^2 |f(\mathbf{k})|^2 + \frac{\gamma_1}{2} \left\{ 1 + \alpha \sqrt{1 + \frac{4\gamma_0^2 |f(\mathbf{k})|^2}{\gamma_1^2} + \frac{4\gamma_0^2 \triangle^2 |f(\mathbf{k})|^2}{\gamma_1^4}} \right\} \right)^{\frac{1}{2}}
\tag{2.20}
$$

At the K points, the function $f(\mathbf{k}) = 0$. Therefore, in the low energy regime, the band opens an energy gap of the magnitude $\triangle$ in the vicinity of the K points. As shown in Fig. 2.4, this gap has a shape of "Mexican hat". Experimentally, we can tune the electric field by gating, therefore, this gap is gate tunable.

2.2.3 Bernal-stacked tetralayer graphene

Multi-layer graphene with layer number $N > 10$ is thought to be graphite. However, the electronic properties of graphene with layers $N > 3$ are still of significant interest. In this section, I will discuss the lattice structure and band structure of Bernal- or ABAB-stacked tetralayer graphene.

Among the possible stacking orders, ABAB- and ABCA-stacking orders of tetralayer graphene are observed experimentally [33, 34]. The tight binding model for multi-layer graphene is much more complicated than that of MLG and BLG, since we need to consider more hopping parameters to include the *next-nearest* interlayer couplings [35]. Bernal-stacked tetralayer graphene can be considered as two stacked bilayer graphene. The unit
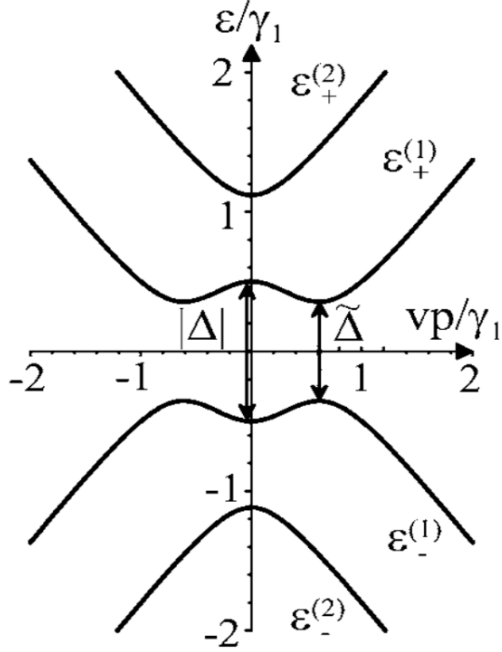
Figure 2.4: Low energy bands of BLG in the presence of an electric field at the K points. For clarity, a large potential difference $\triangle = \gamma_1$ is used. Image adapted from Ref. [32]

cell of tetralayer graphene, as shown in Fig. 2.5, includes eight atoms, two sublattice atoms from each layer, and possesses the inversion symmetry $(x, y, z) \leftrightarrow (-x, -y, -z)$ with the inversion center denoted by the red dot. In addition to the hopping parameters considered in BLG, we also need to take into account the *next-nearest* interlayer hopping parameters γ_2 and γ_5 as shown in Fig. 2.5 by dashed lines. γ_2 is the hopping energy between atoms A_1 and A_3, atoms B_2 and B_4. γ_5 is the hopping energy between atoms B_1 and B_3, atoms A_2 and A_4.

To study the band structure of tetralayer graphene, we start with the effective Hamiltonian described in Ref. [35]. The Bloch wave functions of A and B sublattices are labeled as $|A_j>$ and $|B_j>$, where j indicates the layer number. Therefore, a suitable basis is $|A_1>, |B_1>; |A_2>, |B_2>; |A_3>, |B_3>; |A_4>, |B_4>$. With these basis wave functions,
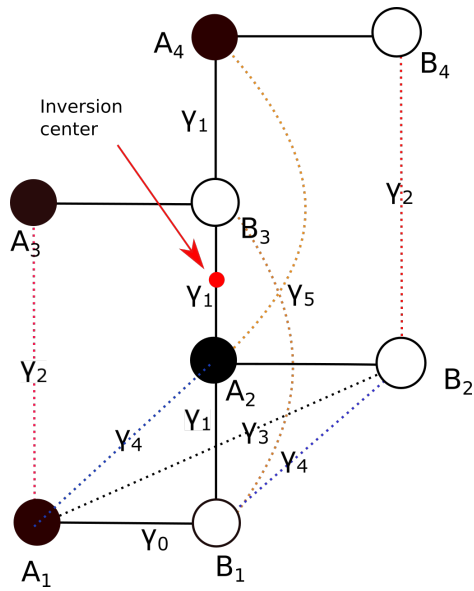
Figure 2.5: Schematic of the unit cell of Bernal-stacked tetralayer graphene. Horizontal solid black lines indicate the nearest coupling γ_0 within sublattices A and B in each layer. Vertical solid lines indicate the nearest layer coupling γ_1 within the dimer sites. Dashed lines indicate the interlayer couplings. γ_2(red dashed line) is the hopping parameter between the stacked non-dimer sites. γ_5 is the hopping parameter between the stacked dimer sites.

the effective Hamiltonian could be written as

$$H = \begin{pmatrix} H_B & W \\ W' & H_B \end{pmatrix} \tag{2.21}$$

where H_B is the effective Hamiltonian of BLG

$$H_B = \begin{pmatrix} 0 & v_F\pi & -v_4\pi^+ & v_3\pi \\ v_F\pi^+ & \triangle' & \gamma_1 & -v_4\pi^+ \\ -v_4\pi & \gamma_1 & \triangle' & v_F\pi \\ v_3\pi^+ & -v_4\pi & v_F\pi^+ & 0 \end{pmatrix} \tag{2.22}$$

where $v_F = \frac{\sqrt{3}a\gamma_0}{2\hbar}$ is the Fermi verlocity, $v_3 = \frac{\sqrt{3}a\gamma_3}{2\hbar}$, $v_4 = \frac{\sqrt{3}a\gamma_4}{2\hbar}$. $\triangle'$ is the energy difference between the dimer and non-dimer sites. $\pi = \xi p_x + ip_y$, where the index $\xi = \pm 1$ represents two valley K_ξ points. W and W' in equation 2.21 are the interactions between the two BLG blocks, and can be written as

$$W = \begin{pmatrix} \frac{\gamma_2}{2} & 0 & 0 & 0 \\ 0 & \frac{\gamma_5}{2} & 0 & 0 \\ -v_4\pi & \gamma_1 & \frac{\gamma_5}{2} & 0 \\ v_3\pi^+ & -v_4\pi & 0 & \frac{\gamma_2}{2} \end{pmatrix}, W' = \begin{pmatrix} \frac{\gamma_2}{2} & 0 & -v_4\pi^+ & v_3\pi \\ 0 & \frac{\gamma_5}{2} & \gamma_1 & -v_4\pi^+ \\ 0 & 0 & \frac{\gamma_5}{2} & 0 \\ 0 & 0 & 0 & \frac{\gamma_2}{2} \end{pmatrix} \tag{2.23}$$

By diagonalizing the effective Hamiltonian, we can obtain the band structure of tetralayer graphene. Due to the inversion symmetry that tetralayer graphene possesses, the valley degeneracy is never broken at zero electric field. Fig. 2.6 shows the numerically calculated low energy bands near the K points at zero electric field. The band structure includes two BLG-like parabolic bands with light effective mass (b) and heavy effective mass (B).

19
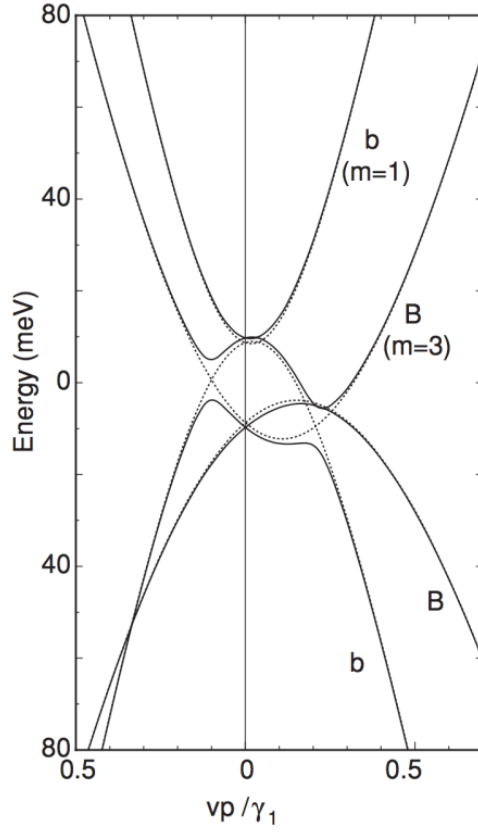
Figure 2.6: Low energy bands of tetralayer graphene at the K points calculated with full parameters included in the absence of electric field. b(m=1) and B(m=3) indicate the energy bands with light and heavy effective masses, respectively. The dotted lines are the results without considering γ_2 and γ_5. Image adapted from Ref. [35]
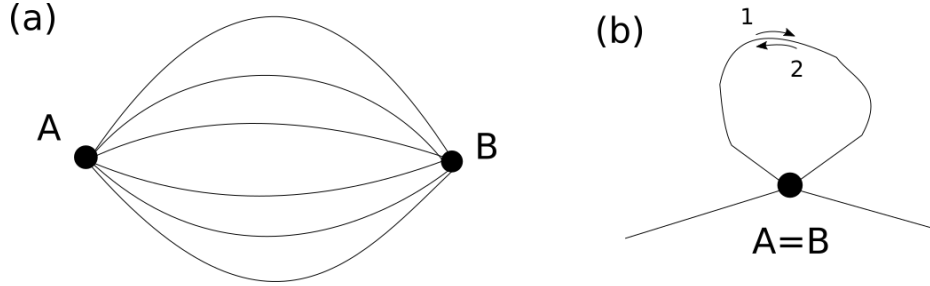
Figure 2.7: Schematics of weak localization. (a) Transport of an electron from point A to point B in the diffusive regime. (b) Enhanced backscattering that leads to weak localization

2.3   Weak localization

Weak localization (WL) is a quantum phenomenon due to the wave nature of quantum particles [36, 37]. In a weakly disordered electronic system, electrons traveling from point A to point B, collide elastically into the impurities that are randomly distributed in the system, as shown in Fig. 2.7a. Due to the multiple scatterings, an electron can travel from point A to point B in many paths (Fig. 2.7a). In classical picture, the total probability that the electron travels from A to B is simply the summation of the probability in each path $P_{total} = \sum_i P_i$, where P_i is the probability in path i. However, quantum mechanically, we need to sum the probability amplitudes rather than the probabilities

$$P_{total} = |\sum A_i|^2 = \sum |A_i|^2 + \sum_{i \neq j} |A_i A_j^*| \tag{2.24}$$

where A_i is the probability amplitude in path i. The first term corresponds to the classical picture, while the second term describes the interferences between different paths, arising from the wave nature of electrons. The latter term averages to zero at high temperature or when coherence length is short.
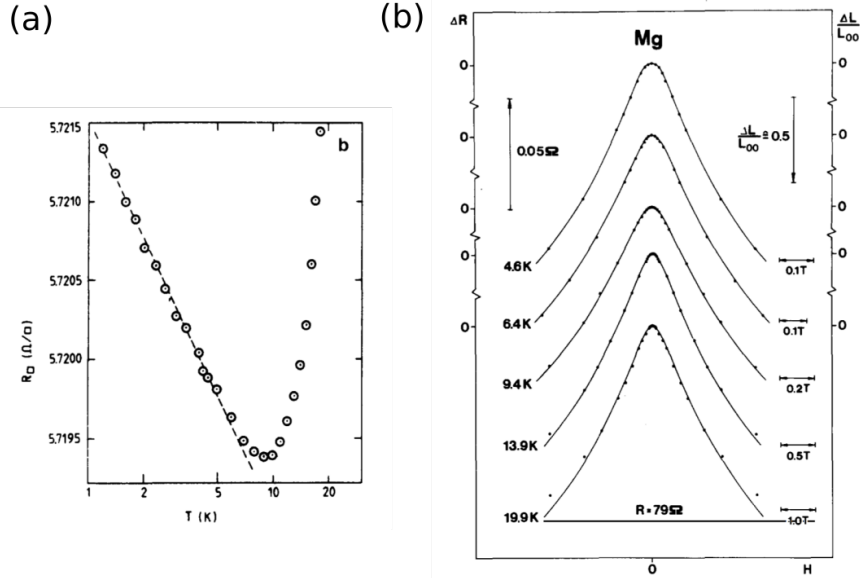
Figure 2.8: Experimental signatures of WL in 2D films. (a) Resistance of a thin disordered AuPd film as a function of temperature. (b) Magnetoresistance of a thin Mg film as a function magnetic field at different temperatures. Image adapted from Ref. [38]

However, one special situation warrants attention, *i.e.* when the electron returns back to its original starting point. In this case, there is always a corresponding time-reversed path, *i.e.* the time-reversed path traces the trajectory of the original path, but in the opposite direction (Fig. 2.7b). Among these time-reserved paths, electrons accumulate opposite phases. Therefore, the probability amplitudes A_1 and A_2 have the same magnitude $|A|$ and coherent. This coherence leads to the constructive interference, so $P_{total} = |A_1|^2 + |A_2|^2 + |A_1 A_2^*| + |A_2 A_1^*| = 4|A|^2$. Thus, the probability for the electron to return its original starting point doubles than that in classical picture. This phenomenon is referred to as *enhanced backstattering* [38]. Since the resistivity of the electronic system is relevant to the transmission probability, enhanced backscattering leads to an additional term to the classical resistivity.
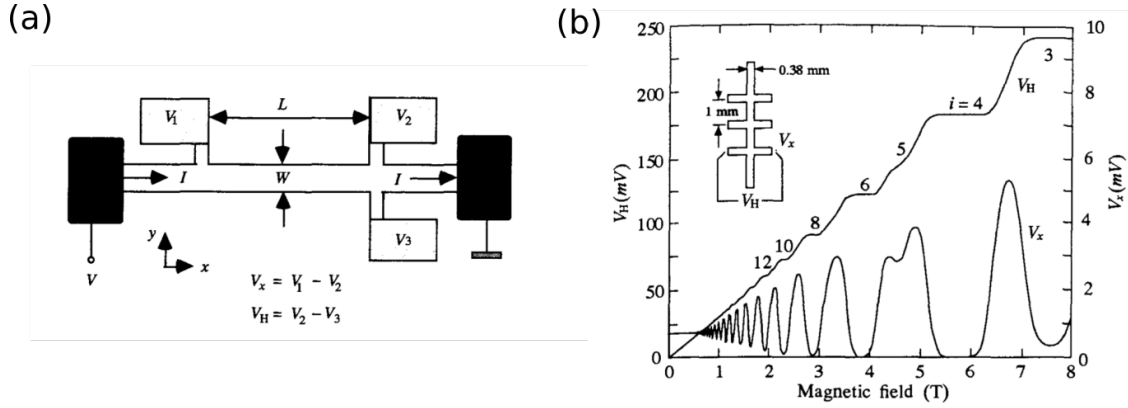
Figure 2.9: Quantum Hall effect in a conventional 2DEG. (a) Rectangular Hall bar to measure magnetoresistance. The direction of magnetic field is in z-direction, perpendicular to the plane of the conductor. (b) Measured longitudinal and transverse voltages of a modulation-doped GaAs thin film at $T = 1.2$ K, with current source $I = 25.5$ μA. Image adapted from [39]

Two experimental signatures of weak localization are the dependence of resistivity on temperature and magnetic field [38]. At a high temperature, the quantum coherence is destroyed, and the resistivity of the system will decrease to that of classical value, as shown in Fig. 2.8a, where resistivity decreases with increasing temperature below a characteristic temperature. Another way to study weak localization is to apply a perpendicular magnetic field that breaks the time-reversal symmetry. For a closed path, the magnetic field B introduces an extra phase term $\phi = \frac{2\pi\Phi}{\Phi_0}$, where Φ is the magnetic flux enclosed within the loop and $\Phi_0 = \frac{h}{e}$ is the flux quantum. With the extra phases, enhanced backscattering is reduced and eventually the classical value is recovered, as shown in Fig. 2.8b.

2.4 Quantum Hall effect

For a 2DEG system in the classical Hall effect regime [30], as shown in Fig. 2.9a, the source current I_x is injected from source to drain electrodes. From the Drude model, electron deflection due to the Lorentz force causes a potential difference to build up in the transverse direction. The current density $\vec{J}$ is related to the electric field $\vec{E}$ by

$$\begin{pmatrix} J_x \\ J_y \end{pmatrix} = \begin{pmatrix} \sigma_{xx} & \sigma_{xy} \\ \sigma_{yx} & \sigma_{yy} \end{pmatrix} \begin{pmatrix} E_x \\ E_y \end{pmatrix} \tag{2.25}$$

where $\sigma_{xx} = \sigma_{yy}$, $\sigma_{xy} = -\sigma_{yx}$, and can be calculated from the measured longitudinal resistivity ρ_{xx} and the transverse resistivity ρ_{xy} by

$$\sigma_{xx} = \frac{\rho_{xx}}{\rho_{xx}^2 + \rho_{xy}^2}, \quad \sigma_{xy} = \frac{\rho_{xy}}{\rho_{xx}^2 + \rho_{xy}^2} \tag{2.26}$$

In a cleaner sample at lower temperatures, the 2DEG can go to the quantum Hall (QH) regime [40], where the energies of cyclotron orbits are quantized to discrete levels, called Landau levels (LLs) [41]. In low magnetic fields, ρ_{xx} displays the so-called Shubnikov-de Haas oscillation as the Fermi level fills successive LLs [30]. In high B fields, transverse conductivity σ_{xy} starts to be quantized (Fig. 2.9b). Each transverse conductivity plateau has an integer quantum conducatnce $\nu e^2/h$, where ν is the filling factor, meaning the total number of filled LLs. At each plateau, the corresponding longitudinal resistivity is vanishing. The precise quantization of σ_{xy} gives rise to the name quantum Hall effect. In the QHE regime, the confining potential, resulting from the finite size of the samples, gives rise to the chiral 1D channels that are topologically protected from back scattering, thus allowing dissipationless transport [30].
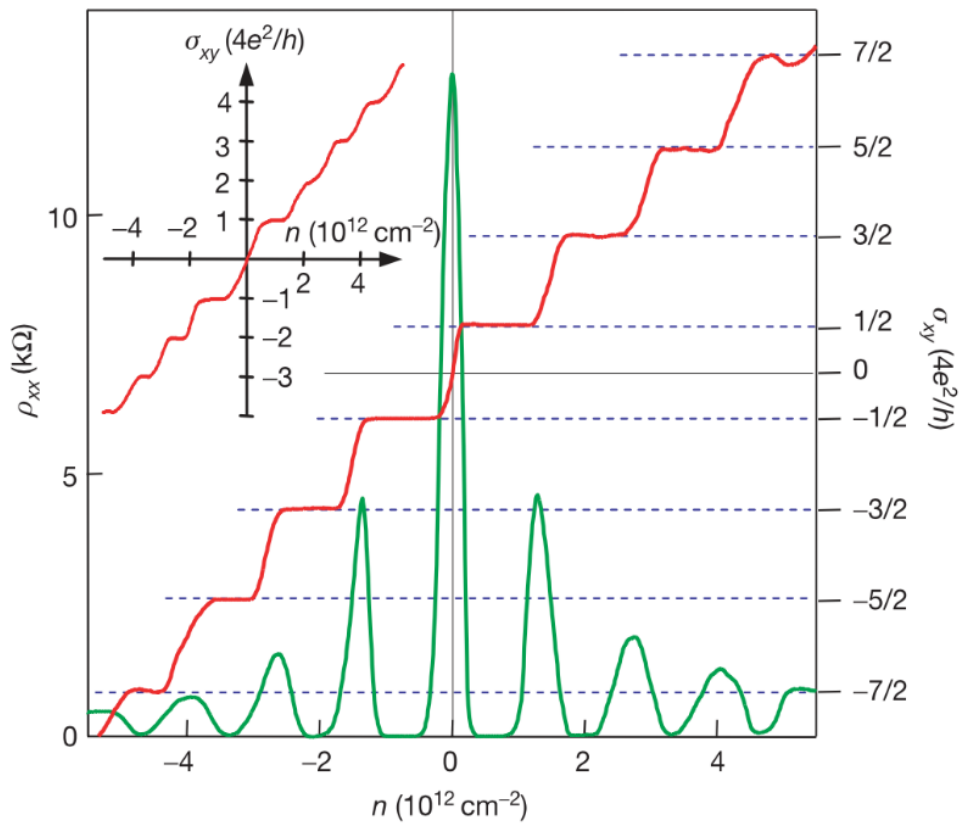
Figure 2.10: Half-integer QHE in MLG. Measured longitudinal resistivity ρ_{xx} and calculated transverse conductivity σ_{xy}. Measurement is taken at $B = 14$ T and $T = 4$ K. Image adapted from [7]

In a conventional 2DEG, energies of LLs are $E_N = \hbar\omega_c(N+\frac{1}{2})$ and equally spaced, and $\sigma_{xy} = \nu\frac{e^2}{h}$. In contrast, MLG's LL spectrum is

$$E_N = sgn(N)\sqrt{2\hbar|N|eB}, \quad N = 0, \pm1, \pm2, \ldots \tag{2.27}$$

where N is the LL index. The LL at $E_N = 0$ is distinctive and a result of the Dirac nature of the energy band. The measured longitudinal resistivity and transverse conductivity σ_{xy} are shown in Fig. 2.10. The quantized conductivity plateaus appear at

$$\sigma_{xy} = 4\frac{e^2}{h}(N + \frac{1}{2}) \tag{2.28}$$

where $\nu = 4(N + \frac{1}{2})$ is the filling factor. The prefactor 4 comes from the four-fold degeneracy including valley and real spin degeneracy of each LL. This $\frac{1}{2}$ shift is due to the Berry's phase, as a result of the precession of the pseudospin during the cyclotron motions of Dirac fermions. Therefore, the filling factors of the integer QH states in MLG are $\ldots, -6, -2, 2, 6 \ldots$ [7,8]. At a higher magnetic field, the four-fold degeneracy could be lifted, leading to the symmetry-broken QH states.

For BLG, the energies of the LLs are

$$E_N = sgn(N)\hbar\omega_c\sqrt{N(N-1)}, \quad N = 0, \pm1, \pm2, \ldots \tag{2.29}$$

where the cyclotron frequency $\omega_c = eB/m^*$, and $m^* = \gamma_1/2v_F^2 \approx 0.03m_e$ is the effective mass of electrons in BLG [31]. Each LL is also four-fold degenerate, except that at $E_N = 0$, where the zero-LL is eight-fold degenerate, due to the additional $N = 0$ and $N = 1$ orbital degeneracy. Fig. 2.11 shows the experimental QHE in BLG. The sequences of the filling factors are $\ldots, -8, -4, 4, 8, \ldots$ [42]. As discussed above, the valley symmetry in BLG is
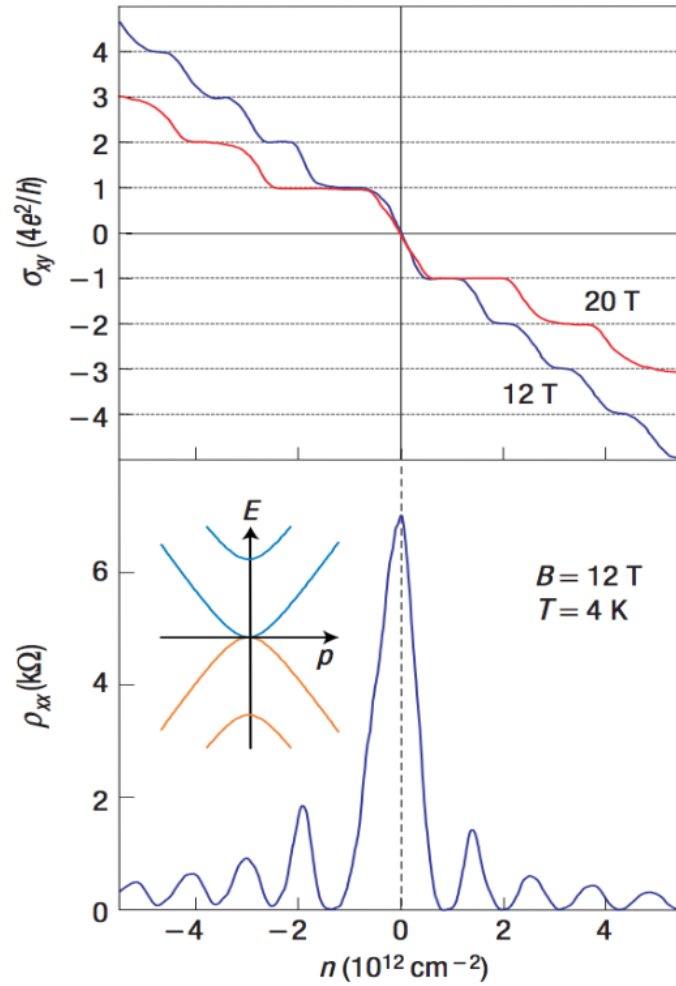
Figure 2.11: QHE in BLG. Measured longitudinal resistivity ρ_{xx} and calculated transverse conductivity σ_{xy} as a function of carrier density in BLG. Image adapted from [42]
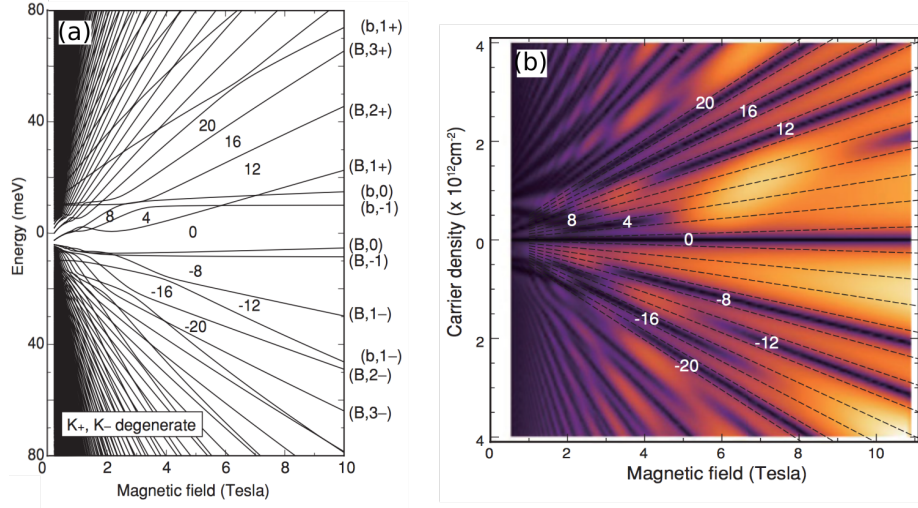
Figure 2.12: (a) Calculated LL spectrum of tetralayer graphene at zero electric field. (b) Density of states as a function of B field and charge density calculated from (a). Numbers represent the quantized Hall conductivity in units of e^2/h. Image adapted from Ref. [35]

equivalent to the layer symmetry in the low energy regime and it can be broken by a perpendicular electric field as well as electronic interactions. A high magnetic field can be used to break the real spin and orbital symmetries. These symmetry-broken states will be discussed in chapter 4.

The LL spectrum of tetralayer graphene in a uniform and perpendicular magnetic field can be calculated by using LLs' wavefunctions as a basis [35]. π and π^+ coincide with the raising and lowering operators in the basis of LLs' wavefunctions [35]. As shown in Fig. 2.12a, the LL bands can be construed as a combination of two BLG-like LL bands with light (b) and heavy (B) effective masses. The orbital degeneracy of the lowest LL of each BLG-like band is lifted by the magnetic field. Therefore, the 16-fold degenerate zero-LL is split into four energy bands, each with real spin degeneracy as well as valley degeneracy. Fig. 2.12b shows the calculated two-dimensional plot of density of states as a function of

magnetic field and charge density. The numbers in Fig. 2.12(a-b) represent the quantized

Hall conductivity in units of e^2/h. Each LL is four-fold degenerate, due to the spin and

valley degeneracy.

Chapter 3

Device Fabrication

As an experimentalist, I always strive to fabricate high quality devices. Fabrication of devices is a vital component in experimental research, because the intrinsic physics can only be revealed in devices with low impurities and disorders. The first generation of two-dimensional (2D) devices consist of flakes on Si/SiO_2 substrates coupled with metal contacts [3, 7, 8]. However, due to the roughness of SiO_2 surface and large number of dangling bonds, the flakes are inhomogeneously doped, leading to the formation of electron-hole puddles [43], thus limiting the quality and mobility of devices. The research community has since made great strides to reduce the substrate induced impurities and improve devices' quality.

During my five-year tenure as a PhD student, I have witnessed and partaken in the development of these efforts. To reduce the effects of the substrates, the first idea is to remove them [10, 11]. By removing SiO_2, the mobility of suspended graphene devices improves by orders of magnitude, which will be discussed in section 3.1. Alternatively to

reduce substrate induced electron-hole puddles, one may try to use different substrates. Hexagonal boron nitride (hBN) is a layered material with a honeycomb lattice structure, and B and N atoms occupying two sublattices. It has been proven to be an ideal substrate for two dimensional materials due to its atomically flat surface and lack of dangling bonds [44]. Using hBN, we are able to fabricate sandwich heterostructures. Dry transfer technique is applied to fabricate black phosphorous (BP) devices encapsulated by hBN sheets [28], and will be discussed in section 3.2. Here, hBN not only provides a flat substrate, but also protection from degradation due to the air and moisture. The other technique referred to as the pickup technique was developed in Ref. [45], and was used to fabricate hBN-encapsulated sandwich heterostructures; here the active components (graphene or other 2D materials) never come in contact with any resist or solution, thus greatly improving the quality of devices.

3.1   Suspended graphene devices with contactless top gates

The advantages of suspended devices over those that are supported on Si/SiO_2 substrates are three-fold . Firstly, the absence of substrates eliminates the inhomogeneous potential created due to the trapped charges or corrugations, which are the mobility bottlenecks of SiO_2 supported devices [43, 46]. Secondly, current annealing, which is used to remove impurities on graphene flakes [47], is far more effective on free-standing samples than substrate-supported devices due to the absence of heat sink to substrates [10,11,43,46]. Thirdly, because of the absence of screening, electronic interaction effects are larger in suspended devices than Si/SiO_2 supported devices [48]. The interaction parameter is given
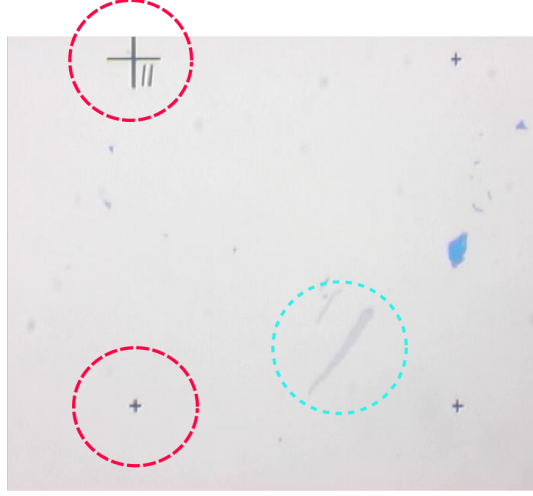
Figure 3.1: A BLG flake (blue circle) on Si/SiO$_2$ with metalized alignment marks (red circles).

as

$$\alpha \propto \frac{n^{-(p-1)/2}}{\epsilon_r} \tag{3.1}$$

where n is the charge density, p the power of energy dispersion, which depends on the layer number and stacking order of graphene. For example, $p = 1$ in single layer graphene, and 2 for bilayer graphene (BLG). ϵ_r is the dielectric constant of surrounding environment. The dielectric constant of SiO$_2$ is $\sim$ 3.9, larger than that of vacuum. Therefore, the interaction effects in free-standing graphene devices are larger than that of SiO$_2$ supported ones.

3.1.1 Fabrication of contactless top gates

To fabricate free-standing graphene devices, we first exfoliate graphene flakes from bulk Kish graphite with a piece of scotch tape, then locate the graphene flakes with an optical microscope [3]. The number of layers can be determined by the optical contrast, and confirmed by Raman spectroscopy [49]. The intensity ratio of G and 2D peaks of bilayer

graphene is ~ 1.5 [34]. For the suspended graphene project, we choose to use graphene flakes that are long and narrow as the width is limited by the length of the bridge-like top gates. Moreover, current annealing is more effective on long two-terminal devices than on multi-terminal Hall bar devices [43, 46]. After locating the graphene flakes on the chip, we spin coat one layer of methyl methacryllate (MMA) and a layer of poly methyl methacryllate (PMMA), both at the rate of 4000 rpm for 40 seconds; each layer is baked on a hotplate at 180 °C for 10 minutes. Then, we perform electron-beam lithography (EBL) to expose alignment patterns on the bilayer resist, followed by the metalization. An optical image of graphene with metalized alignment marks is shown in Fig. 3.1. The crosses in the red circles are the metalized alignment marks. The blue circle indicates the BLG strip.

Fig. 3.2 illustrates the process of fabricating contactless top gates [50]. This process includes several steps of spin coating of resists, EBL and angled e-beam evaporation. After metalizing the alignment marks and lifting-off in hot acetone at 65 °C (Fig. 3.2a), we spin coat a layer of lift-off resist (LOR) 3B, and bake the chip at 190 °C for 5 minutes. Another resist layer PMMA is spun coated on top of LOR, followed by baking at 180 °C for 10 minutes, as shown in Fig. 3.2b. We then perform EBL to define the patterns of the electrodes of top gates on the bilayer resist. The developing process after EBL includes two steps. Firstly, we dissolve the exposed PMMA in the developer MIBK for ~ 65 seconds, followed by submerging in high quality IPA, and drying by a nitrogen gun. After this step, it is necessary to check under an optical microscope if the patterns are well developed. If not, repeating the developing in MIBK may help to remove the residues of PMMA, especially if the EBL dosage is slightly lower than needed. Secondly, we submerge the chip
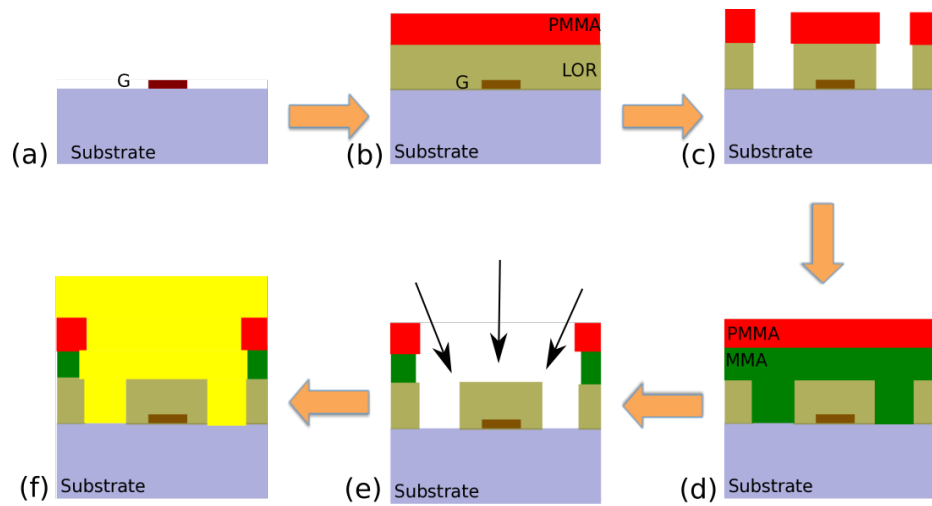
Figure 3.2: Schematics of the fabrication processes of contactless top gates. (a) A bi-layer graphene flake(dark brown) is deposited on Si/SiO$_2$ substrate. (b) Bilayer resist LOR(yellow)/PMMA(red) is spun coated on top of graphene. (c) Open windows for electrodes after EBL and developing in MIBK and MF319. (d)After removing PMMA in acetone, leaving LOR on the substrate, another bilayer resist MMA(green)/PMMA(red) is spun coated on the chip. (e) Open windows of both electrodes and suspended structure after EBL and developing in MIBK. Metals are deposited in three angles (in directions of arrows) (f) Metal Cr/Au(gold) is evaporated in directions indicated by the arrows in (e)

in MF319 to dissolve the LOR in the exposed PMMA windows for ~ 1.5 seconds. The exact duration depends on the thickness of LOR. The resultant structure is shown in Fig. 3.2c. Subsequently, the chip is put in warm acetone (65 °C) to remove the entire layer of PMMA, while leaving LOR on the substrate. The open windows in LOR are for the electrodes of the top gate.

Subsequently, we spin coat a resist bilayer MMA/PMMA on top of LOR layer, and bake the chip at 180 °C for 10 minutes after each layer as shown in Fig. 3.2d. We then perform another step of EBL, in which we define the patterns of both electrodes and bridges of top gates. After EBL, we submerge the chip in MIBK for 65 seconds to dissolve the exposed MMA/PMMA bilayer resist. The outcome is shown in Fig. 3.2e. It is worth noting that MMA dissolves faster than PMMA at the same dosage, leaving an undercut structure as shown in Fig. 3.2e. We then deposit the metal onto the chip at three angles +45°, -45° and 0°. The arrows in Fig. 3.2e indicate the three angles. The evaporations at $\pm 45°$ angles are necessary to strengthen the side walls that connect the bridge and electrode leads [50]. The structure after the three-angle evaporation is shown in Fig. 3.2f. The chip is then put in warm remover PG solvent (65°C) to lift off the unwanted metal and dried out in a critical point dryer (CPD) using high quality IPA.

Fig. 3.3 shows a typical scanning electron microscope (SEM) image of a completed suspended top gate with false colors. The green air bridge is connected with the pink electrode leads by the vertical side walls. The blue structures are anchors on top of graphene, written during the same EBL steps of top gate fabriation, so as to anchor graphene flakes onto the substrates. Otherwise, the graphene flake may be washed away or folded during
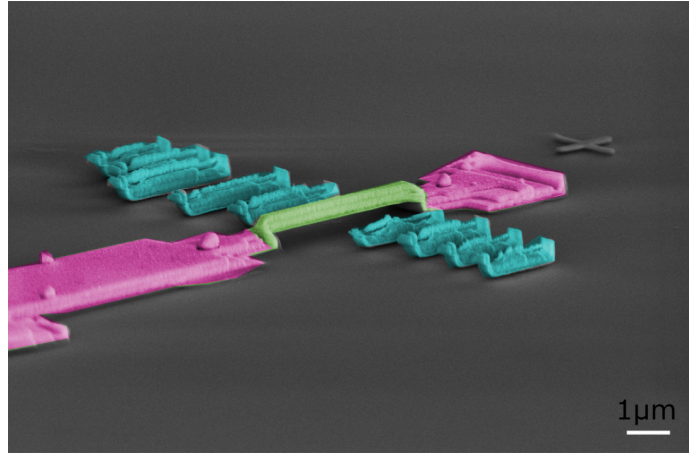
Figure 3.3: SEM image of a suspended top gate. The air bridge (green) is connected to gate electrodes (pink). The anchors (blue) are used to hold the graphene flake in place during fabrication. Scale bar: 1 μm

fabrication. The typical width of an air bridge ranges from 0.5 μm to 1.5 μm. Its length is determined by the width of graphene flake, and can be as long as 5 μm [50, 51], though we usually keep the length as short as possible so that the top gates can sustain higher voltages. The height of top gates, which is the distance from the bottom side of the air bridge to the graphene flake, is determined by the thickness of LOR. In this recipe, the height is $\sim$ 200 nm.

3.1.2 Fabrication of electrodes and suspension of devices

After completing the suspended top gates, the next step is to fabricate the contact electrodes and complete the suspension of the devices [50]. Due to the extensive chemical processings during the top gate fabrication, significant resist residues and impurities are left on the graphene flakes [50–52]. To ensure good contact between graphene and the metal

electrodes, we use O_2 annealing in a furnace to remove the impurities, in which the quartz tube is firstly cleaned by heating to 900 °C for 1 hour, so as to remove the organic residues in the quartz tube, followed by the chip at 300 °C for 2.5 hours. The flow rates of O_2 in both steps are 0.4 sccm.

After annealing, we spin coat a bilayer resist MMA/PMMA and bake the chip at 180 °C for 10 minutes after each layer, followed by the standard EBL to define the source and drain electrode patterns. The bottom resist MMA plays an important role in this step, because as discussed in last section, MMA is more sensitive to electron beams than PMMA. Therefore, after developing in MIBK, MMA will create an undercut under the PMMA layer (Fig. 3.4a). This undercut is important in two ways. Firstly, the undercut allows easy removal of Cr/Au during the lift-off procedure. Secondly, since often we need a global top gate which is fabricated before electrodes, we need to reduce the distances between the top gate and electrodes carefully while avoiding shortage. This undercut ensures that the distance between source-drain electrodes is shorter than designed, so that the top gate could extend directly above parts of electrodes to be a global gate as shown in Fig. 3.4b. After developing the exposed MMA/PMMA, we deposit Cr/Au (10/80 nm) onto the chip, followed by lifting-off in a warm (65 °C) acetone bath overnight. Then we dilute the acetone with high quality IPA repeatedly. Finally, we put the completed substrate supported devices into buffered oxide etch (BOE 6:1) for 70 seconds to partially etch SiO_2 away, as shown in Fig. 3.4c. After BOE etching, we immediately dilute BOE with DI water repeatedly, and similarly, followed by the dilution of DI water in high quality IPA for several times to prepare for critical point drying. Fig. 3.5 illustrates an example of completed suspended
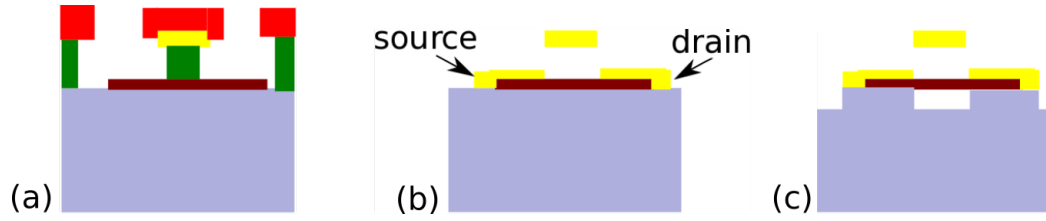
Figure 3.4: Schematics of electrodes fabrication process and suspension of devices. (a)Open windows for electrodes after dissolving PMMA(red)/MMA(green) in MIBK. (b) Completed devices with source and drain electrodes and a contactless top gate on substrate. (c) Completed suspended device with a contactless top gate after etching in BOE.

graphene devices with a suspended top gate. Using this technique, one can also fabricate suspended devices with local top gates for $p - n - p$ junctions, by varying the distances between the top gate and source/drain electrodes.

3.2 Dry transfer technique

In this section, I will discuss the techniques used to fabricate BP devices [15, 28, 53, 54]. BP is very sensitive to the air and moisture [55]. BP flakes should have no direct contact with liquid, and be protected from the air during fabrication. Initial efforts in solving this problem are to use PMMA [56] or Al_2O_3 [57] as a protective layer. Here, we use a dry transfer technique [53] to encapsulate few-layer phosphorene (FLP) between two hBN flakes, so FLP flakes never have direct contact with any liquid or the air. To avoid the degradation of BP, all exfoliation and transferring steps are finished in a glove box with an inert Ar atmosphere.
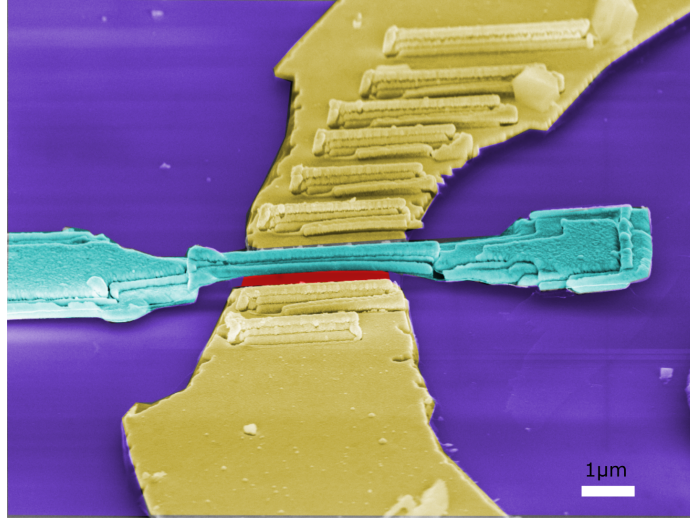
Figure 3.5: False-color SEM image of a device with a suspended top gate (light blue) above a suspended bilayer graphene (red), clamped on by source-drain electrodes (yellow) on partially etched substrates (purple). Scale bar: 1 μm

3.2.1 Assembly of hBN/FLP/hBN stack

hBN has proved to be a very flat substrate [44]. The roughness of the surface of a hBN flake is $\sim$ 100 pm when it is thicker than 15 nm, which is a factor of 3 times smaller than that of SiO_2. In addition, the absence of dangling bonds on the surface makes hBN a perfect substrate for 2D membranes. Similar to graphene, bulk hBN crystal is a layered material and can be exfoliated by scotch tape [3]. We can use thin hBN flakes to encapsulate BP flakes to create sandwich hBN/FLP/hBN heterostructures. In addition to serving as a protective layer, hBN is also a gate dielectric material owing to its large band gap $\sim$ 5.2 eV and a dielectric constant $\sim$ 3.9 [44].

To fabricate hBN/FLP/hBN sandwich heterostructures using the dry transfer technique, we first prepare a polydimethylsiloxane (PDMS) stamp [15,28,53,54]. We either use commercial or home-mixed PDMS; in the latter case PDMS with different thicknesses

can be made. We place PDMS directly onto a piece of microscope glass slide, and the adhesion between them is very strong. Then we separately exfoliate FLP and hBN flakes onto PDMS stamps with scotch tape. The trick here is to peel off the tape quickly from PDMS, since otherwise there will be very few flakes left on PDMS. After depositing the 2D crystals onto PMDS, the PDMS surface is inspected under an optical microscope. Fig. 3.6 shows the optical images of BP and hBN flakes. In the left panel, the FLP flake, indicated by the red dashed circle, is $\sim$ 15–20 nm, and appears faint due to the transparency. The middle panel displays a hBN flake on PDMS, which will be the top layer in the completed stack.

Similarly, we exfoliate hBN flakes on Si/SiO$_2$ (300 nm) substrates, followed by thermal annealing in a mixture gas of H$_2$/Ar in the furnace for 2.5 hours at 400 °C, and at the flow rates of 0.53 sccm (H$_2$) and 4.0 sccm (Ar), so as to remove the tape residues on the surfaces of hBN flakes. Atomically smooth hBN flakes that are $\sim$ 10–30 nm thick are selected to use in this project. The right panel of Fig. 3.6 displays a hBN flake on Si/SiO$_2$ substrate, that forms the bottom layer in the completed stack. hBN flakes with blue color under microscope are $\sim$ 15–30 nm thick.

Fig. 3.7 illustrates the steps of dry transfer. After exfoliating FLP on a PDMS stamp that in turn rests on a glass slide, we invert the stamp, as shown in Fig. 3.7a. Then the receiving substrate is placed on a transfer stage that can travel in X, Y and Z directions. Slowly, we lower the stamp to the receiving substrate, and align the FLP flake on the PDMS stamp with the hBN flake on the receiving substrate when the two flakes start to come into contact. We lower the stamp very slowly to reduce bubbles, until they are in complete

contact, then we start to raise the stamp up. It seems that the van der Waals force between FLP and hBN is a little weaker than that between FLP and PDMS, so the yield of a single transfer step is not 100%. The yield can be improved by slowly peeling off the FLP flake from hBN flake, and repeating the transfer step if needed, though multiple repetitions tend to produce bubbles at the FLP/hBN interface. We note that, due to the roughness and the strain applied to soft PDMS surfaces during exfoliation, the surfaces of 2D flakes on PDMS sometimes have ripples. Interestingly, after transferring these flakes onto bottom hBN flakes resting on Si/SiO_2 substrates, these ripples disappear.

After transferring the FLP flake from PDMS onto the hBN flake on SiO_2, we then invert the PDMS stamp with the hBN flake, and repeat the above transfer procedure to bring hBN and FLP into contact. We find that the success yield of transferring hBN onto FLP is 100%. An example of completed hBN/FLP/hBN stacks is shown in Fig. 3.7c, where the green area is the hBN flake on SiO_2 substrate, and at the bottom of the stack, the brown area the FLP flake, and the pink area the top hBN flake transferred from PDMS. The entire transfer procedure is performed without any resist or solvent in a glove box with an inert Ar atmosphere, so as to avoid FLP degrading from the air or moisture during assembling. The encapsulating hBN layers protect the FLP flakes from degradation during the subsequent fabrication of electrodes.
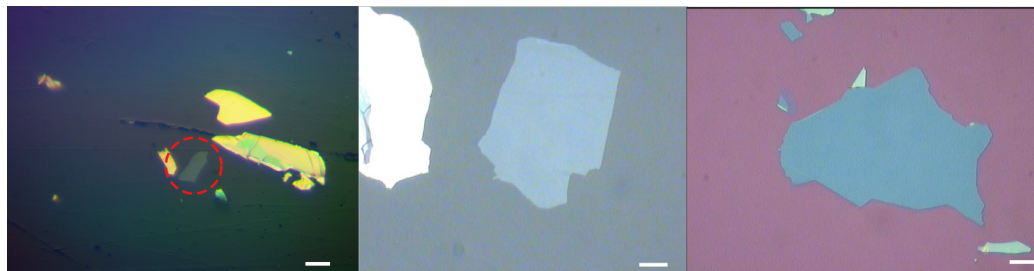
Figure 3.6: Optical images of BP and hBN flakes. From left to right: BP flake(red circle) on PMDS; hBN flake on PDMS; hBN flake on Si/SiO$_2$ substrates. Scale bar: 10 μm
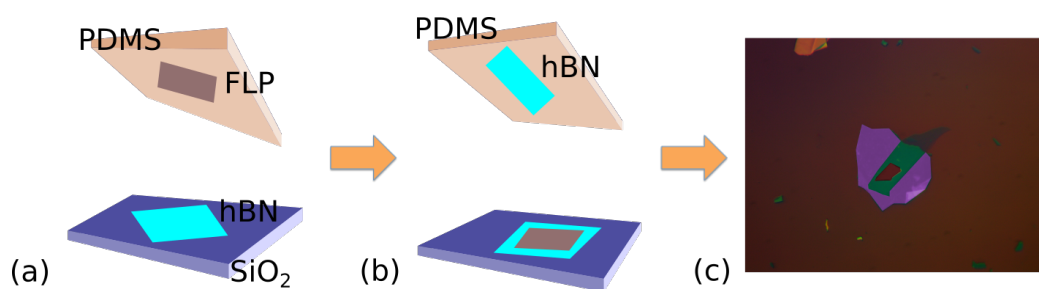
Figure 3.7: Schematics of dry transfer process. (a) FLP flake (brown) on PDMS (yellow) is lowered and put into contact with hBN (light blue) on SiO$_2$ substrate (dark blue). (b) hBN (light blue) on PDMS is put into contact with FLP/hBN stack on SiO$_2$ substrate. (c) Optical image of a completed hBN/FLP/hBN heterostructure. A FLP flake(brown) is encapsulated between top hBN (green) and bottom hBN (purple).
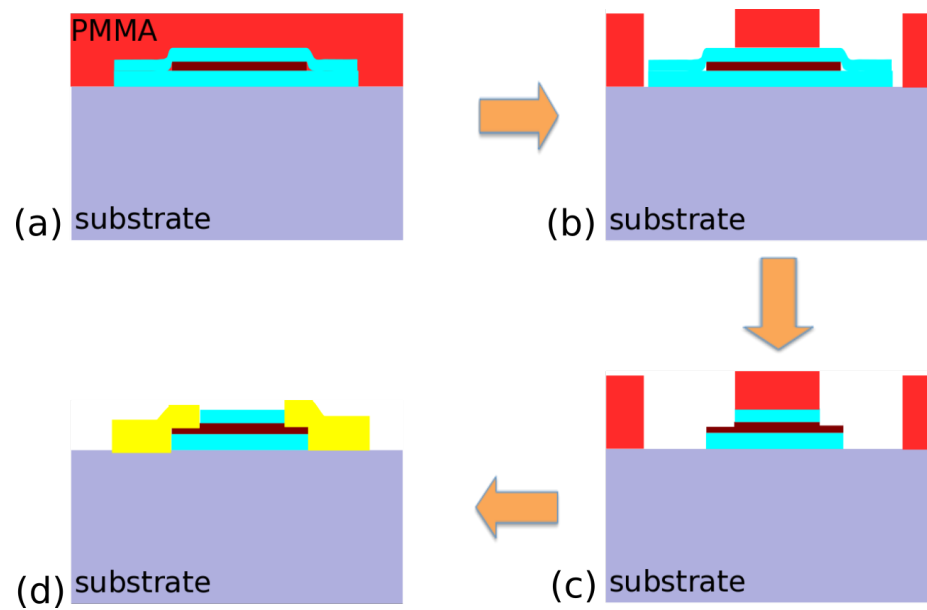
Figure 3.8: (a) Two layers of PMMA (red) are spun coated on top of hBN(light blue)/FLP(brown)/hBN stack on SiO_2 substrates (blue). (b) Open windows after EBL and developing in MIBK. (c) Exposed top hBN is etch away completely in an ICP etcher. FLP is partially etched. (d) Completed devices with deposited metal electrodes (yellow).

3.2.2 Fabrication of surface contacts

After assembling the hBN/FLP/hBN stacks, no annealing or other procedures are performed to clean the stacks. We firstly spin coat two layers of PMMA on the substrates at the rate of 4000 rpm for 45 seconds, and each layer is baked at 180 °C for 10 minutes. Then we define and metalize the alignment marks. Subsequently, we use the same recipe to spin coat and bake another two layers of PMMA. Fig. 3.8 illustrates the process of fabricating BP surface contacts. We use two layers of PMMA instead of MMA/PMMA bilayer because MMA creates an undercut structure after developing in MIBK, and it will expose larger area of stack than designed, rendering the subsequent plasma etching less controllable. We then define the electrodes by EBL, followed by developing in MIBK for 65 seconds to create windows for the electrodes, as shown in Fig. 3.8b. We put the stack into inductively coupled plasma (ICP) etcher, and etch the stack in SF_6 plasma. The pressure is 20 mTorr, and the RF/ICP generator powers are 30/300 W, respectively. We note that hBN can be etched away easily, while FLP is more robust against SF_6 plasma. To ensure that the top hBN is completely removed, we take the chip out of ICP every few seconds, depending on the thickness of top hBN flake, to check the extent of etching under an optical microscope. For a hBN flake with a thickness of 15 nm, the total etching time is ~ 10 seconds. For comparison, we also check the portion of top hBN flake that rests directly on Si/SiO_2 substrate. If this part of top hBN is etched away, we can be reasonably certain that the top hBN is removed completely and FLP flake surface is exposed. As shown in Fig. 3.8c, the partial FLP surface is exposed after etching the top hBN away. We immediately put the chip in the e-beam evaporator, so that the FLP surface is exposed to the air in less

than one minute. We evaporate Cr/Au (10/80 nm) metal onto the chip, followed by the lift-off procedure in acetone at room temperature. The schematic of a completed device is shown in Fig. 3.8d.

3.3   Resist-free transfer technique

The development of the resist-free pickup technique [45] has improved the quality of devices by orders of magnitude. The graphene flakes encapsulated between two hBN layers are very clean, since during the fabrication, graphene flakes do not contact any resist or solution. The main challenge is the bubbles' formation at the graphene/hBN interfaces. We use this pickup technique in tetralayer graphene project, which will be discussed in chapter 5.

3.3.1   Assembly of hBN/graphene/hBN stacks

To fabricate hBN/graphene/hBN heterstructures, we start with exfoliating graphene on Si/SiO_2 substrates as described in section 3.1. The exfoliating and pre-cleaning of hBN flakes on Si/SiO_2 follow the same procedures described in section 3.2.1.

In the meantime, we place a PDMS stamp on a microscope glass slide, and then spin coat a layer of poly-propylene carbonate (PPC) onto PDMS. The glass slide is then inverted and attached to a home-built micromanipulator as shown Fig.3.9a. Then the prepared glass slid and the hBN flake on Si/SiO_2 substrate are aligned and put into contact with each other by the micromanipulator. The Si/SiO_2 substrate is then heated up to 40
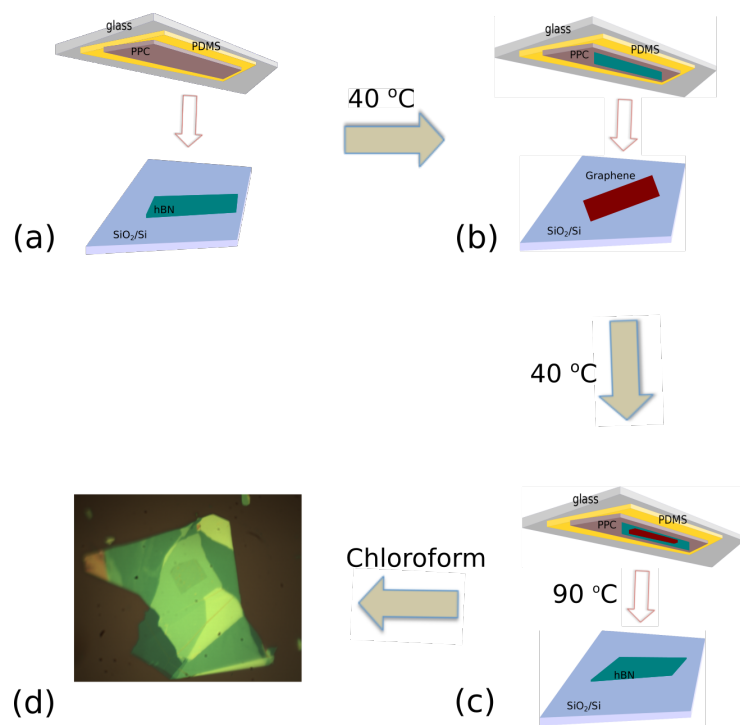
Figure 3.9: (a) A prepared microscope slide(grey) with PDMS (yellow) and PPC (brown) is used to pick up a hBN flake (green) on Si/SiO$_2$ substrate. (b) The hBN flake is used to pick up a graphene flake (deep red) on Si/SiO$_2$. (c) The hBN/graphene stack is transferred onto a hBN flake resting on Si/SiO$_2$ substrate. (d) An optical image of a completed hBN/graphene/hBN stack after removing the PPC in chloroform

°C. After reaching the desired temperature, the glass slide is lifted slowly. At this point, the hBN flake will be picked up from the Si/SiO$_2$ substrate and attached to PPC.

Then the process is repeated to pick up a chosen graphene flake on substrate, as shown in Fig 3.9b. As discussed earlier, the main challenge of this technique is to reduce the bubbles formed at the interfaces between layers. To reduce the number of bubbles, the process of bringing hBN into contact with graphene needs to proceed as slowly as possible. During my fabrication, the contact front line of hBN and graphene moves at the the rate of ~ 1 μm/min.

After picking up the graphene flake, the stack on glass slide is shown in Fig. 3.9c with the graphene/hBN stack on PPC. The last step is to transfer the stack onto the chosen hBN flake by repeating the above procedure, which should proceed slowly to reduce the bubbles' formation. Finally, the substrate is heated up to 90 °C, when PPC melts and detaches from PDMS, leaving the whole hBN/graphene/hBN stack on Si/SiO$_2$ substrate. The chip is then put into chloroform to remove PPC. The optical image of a typical stack is shown in Fig. 3.9d. The hBN/graphene/hBN stack is then annealed at 400 °C for 2.5 hours in H$_2$ (0.53 sccm) and Ar (4 sccm) mixture. We note that the annealing process could reduce the number of bubbles and make the stack more flat.

3.3.2   One-dimensional edge contact

Once encapsulated, the challenge is to make contact to the graphene sheets. One-dimensional contact has been demonstrated to be a very stable and effective approach to achieve high quality graphene devices [15, 28, 45, 53, 54].
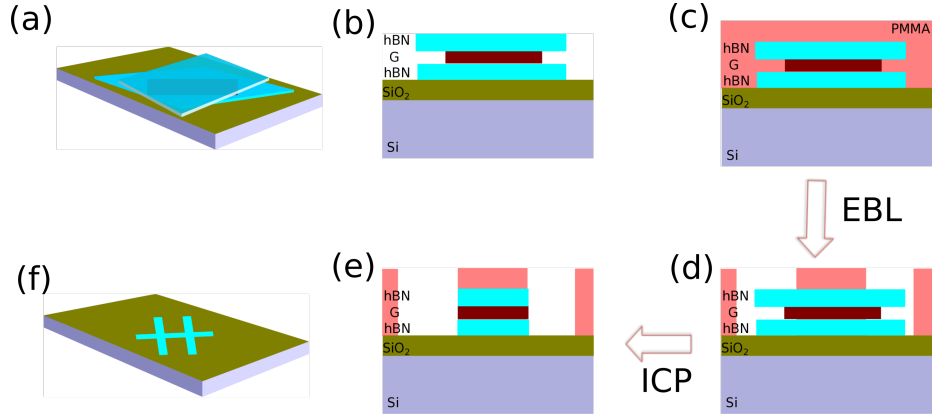
Figure 3.10: (a) A completed hBN(light blue)/G(deep red)/hBN stack on SiO$_2$ substrate. (b) The cross-sectional view of the stack in (a) (c) Two layers of PMMA (pink) are spun coated on the chip. (d) The open window of Hall bar pattern after EBL and developing in MIBK. (e) The stack is etched in ICP etcher with SF$_6$ plasma. (f) The completed Hall bar after removing the PMMA mask.

To fabricate hBN-encapsulated graphene devices, we first follow the same procedures described in section 3.2 to define metalized alignment marks. Fig 3.10 shows the process to fabricate the Hall bar geometry. Firstly, we spin coat two layers of PMMA, as shown in Fig. 3.10b. Using EBL and developing in MIBK afterwards, we define a Hall bar mask on the stack, as shown in Fig. 3.10d. Then we use the ICP etcher to etch away the exposed portion of the stack with SF$_6$ plasma, leaving a Hall bar geometry on the chip (Fig. 3.10(e-f)). The RF and ICP generator powers are 30 W and 300 W, respectively. The etching time is $\sim$ 10 seconds under the pressure of 20 mTorr. Etching time needs to be adjusted according to the thickness of the stack. Finally, we put the chip in warm acetone (65 °C) to remove the PMMA layers.
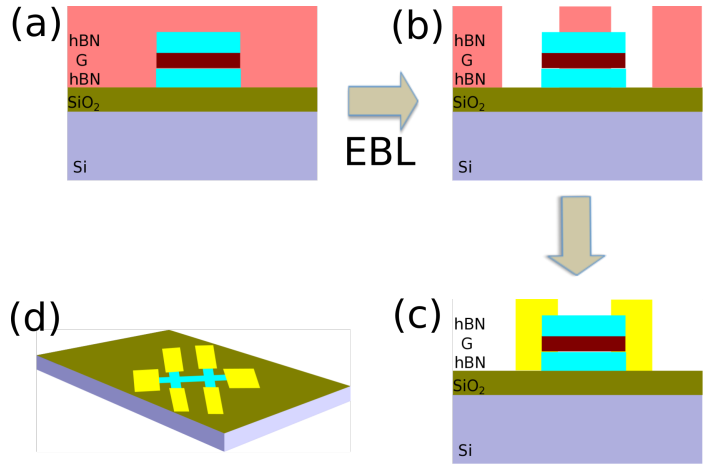
Figure 3.11: (a-c) Two layer so PMMA(pink) are spun coated on the chip. (b) The edges of the Hall bar are exposed by EBL and developing in MIBK. (c) Metal electrodes (yellow) are deposited onto the Hall bar edges. (d) Schematic of a Hall bar device with electrodes.
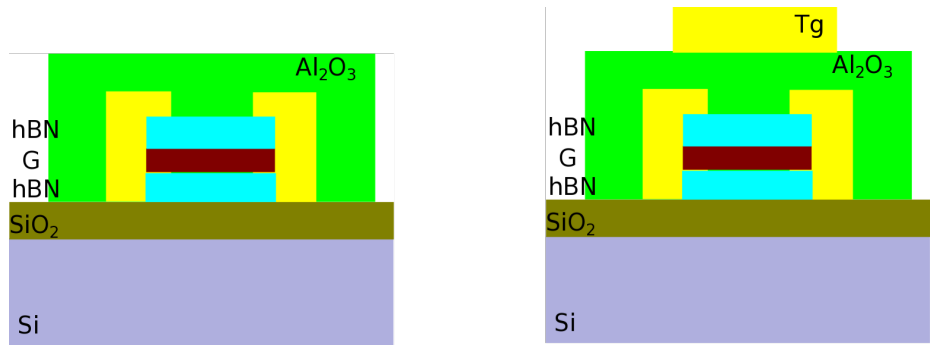
Figure 3.12: (a) A Al_2O_3 layer(green) is deposited on top of the hBN(light blue)/graphene(deep red)/hBN stack via e-beam evaporator. (b) The top gate metals are deposited on Al_2O_3

49

Fig. 3.11 shows the process of making one-dimensional edge contacts to hBN/graphene/hBN heterostructures. After fabricating the Hall bar geometry, we spin coat two layers of PMMA, as shown in Fig. 3.11a. Then, as shown in Fig. 3.11b, we use EBL to expose the edges of the Hall bar terminals. We note that a weak O_2 plasma treatment before metalization can improve the contact of devices. We put the chip in ICP, and treat the stack with O_2 plasma with RF generator power to be 30 W and ICP generator power to be 0 for ~ 10 seconds. We immediately deposit Cr/Au with thickness of 10/80 nm onto the stack with e-beam evaporator. Finally, as shown in Fig. 3.12, we repeat similar procedures to deposit an insulating layer of 50 nm Al_2O_3 on top of the stack with electrodes, followed by the deposition of top gate metals Cr/Au (10/100 nm). The final device structure is shown in Fig. 3.12.

Chapter 4

Energy Gaps and Layer Polarization of Integer and Fractional Quantum Hall States in Bilayer Graphene

Mono- and few-layer graphene are unique two dimensional electron gas (2DEG) systems with compelling electronic properties, such as chiral charge carriers and high charge mobility, and have proved to be fascinating platforms for the study of the quantum Hall (QH) physics [7, 42, 58, 59]. For Bernal- or AB-stacked bilayer graphene (BLG), the orbital, spin and valley degrees of freedom give rise to the 8-fold degeneracy in the lowest Landau level (LL) [32, 42, 60, 61], which can be broken by electronic interactions and/or single-particle perturbations, leading to the QH states at intermediate integer filling factors. As

discussed in chapter 2, at zero magnetic field $B = 0$, a perpendicular electric field $E_\perp$ breaks the inversion symmetry of BLG, inducing a gap in BLG's band structure [51, 52, 60, 62–73]; in the QH regime, the layer and valley indices are equivalent in the lowest LL, thus $E_\perp$ provides an experimental "knob" for selectively breaking the layer/valley symmetry, and inducing phase transitions among different ground states.

In this chapter, I will discuss transport measurements on high quality dual-gated suspended BLG devices with controlled layer polarization. Similar to the two phases in the well-studied QH state at filling factor $\nu = 2$ [71, 74–83], via transport spectroscopy tool [72, 83], we observe two distinct phases of the QH state at $\nu = 1$: a layer polarized state that has a larger energy gap and is stabilized by high electric field, and an interlayer coherent state with a smaller gap that is stabilized by large magnetic field. At much higher B field, we observe the $\nu = 2/3$ fractional QH state, which is only resolved when $E_\perp$ exceeds a critical value $E_{\perp c}$. A feature at $\nu = 1/2$ is also only observed at finite $E_\perp$. These results presented in this chapter highlight the importance of controlling layer polarization in understanding the interplay among quadratic band touching, spin-valley symmetry, and Coulomb interactions in the unusual QH system of BLG.

4.1   Device fabrication and characterization

We use the technique detailed in chapter 3 to fabricate dual-gated suspended BLG devices. A scanning electron microscope (SEM) image of such a device is shown in Fig. 4.1a. Each device typically has length 1.3 μm and width 1 μm. Two-terminal differential
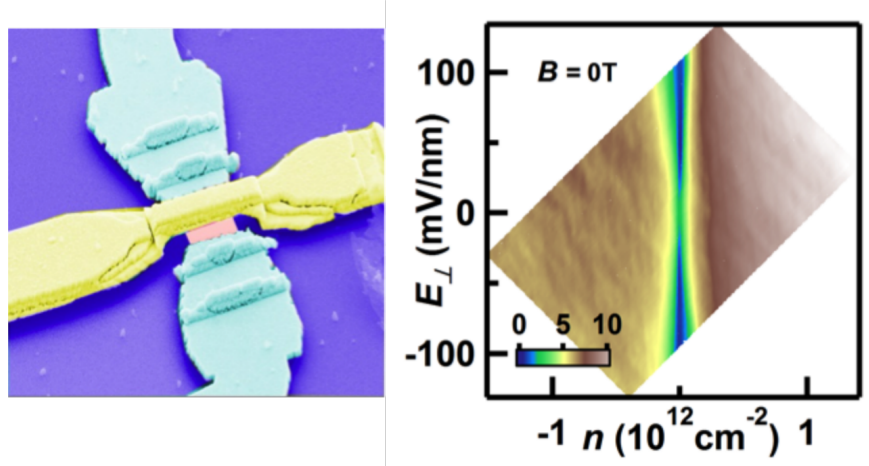
Figure 4.1: (a) A false-color SEM image of a typical device. (b) Two-terminal conductance as a function of n and $E_\perp$ at $B = 0$ T.

conductance G of the two devices are measured using the standard lock-in technique at $T = 300$ mK.

In dual-gated suspended devices, we are able to independently tune both charge carrier density n and electric field $E_\perp$ by applying top gate voltages (V_{tg}) and back gate voltages (V_{bg})

$$n = (C_{bg}V_{bg} + C_{tg}V_{tg})/e - n_0, \quad E_\perp = (C_{bg}V_{bg} - C_{tg}V_{tg})/2\epsilon_0 - E_{\perp 0} \tag{4.1}$$

where C_{tg} and C_{bg} are the capacitance per unit area of top gate and back gate, respectively, n_0 and $E_{\perp 0}$ the residue charge carrier density and induced displacement field due to disorders, and ϵ_0 the permittivity of vacuum.

Fig. 4.1b displays the two-terminal differential conductance G of our devices as a function of n and $E_\perp$ at magnetic field $B = 0$ T. From the gate voltages at which the global charge neutrality point (CNP) appears, the impurity concentration is estimated to be $< 1.5 \times 10^{10}$ cm^{-2}. At $n = 0$, G is 90 μS at $E_\perp = 0$ and decreases symmetrically with

53

$E_\perp$ of either polarity (Fig. 4.1 b), indicating the opening of a band gap due to the broken inversion symmetry [72]. We note that the very symmetric behavior of G with respect to $E_\perp$ suggests the absence of any inadvertently induced electric field (such as that arising from charge impurities).

We focus on transport of two BLG devices with field effect mobilities 12,000 and 23,000 cm^2/Vs, and quantum mobilities 30,000 and 40,000 cm^2/Vs, respectivly. Without symmetry breaking, the Hall conductivity of BLG is expected to be quantized at ± 4, ± 8, ± 12 ... e^2/h, where e is electron charge and h Planck's constant. Fig. 4.2a displays the LL fan diagram $G(n, B)$ at $E_\perp = 0$ for $B = 0$ to 4 T. LLs up to $N = 5$ with properly quantized plateaus are observed (Fig. 4.2b) at $B < 2$ T, attesting to the high quality of the device. However, no symmetry-broken QH states at -4 $< \nu <$ 4 are observed below 6 T. Interestingly, the $\nu = 6$ state is resolved at $E_\perp = 0$ prior to those of lower LLs, contrary to one's naive expectation. Its resolution may arise from disorder or suggest modified symmetry-breaking processes at higher LLs and warrants further studies.

4.2   Two distinct phases of the $\nu = 1$ state

We first focus on the $\nu = 1$ state. Fig. 4.3a plots $G(\nu, E_\perp)$ at $B = 29$ T for device 1. Even at this high field, the $\nu = 1$ state is not resolved at $E_\perp = 0$ even at $B = 29$ T, but becomes fully resolved at larger $E_\perp$ (Fig. 4.3b). $G(E_\perp)$ displays a sharp transition — from 2.5 e^2/h near $E_\perp = 0$, it drops abruptly to ~ 1 e^2/h when $|E_\perp| > \sim 10$ mV/nm (Fig. 4.3c). In fact, at $E_\perp = 36$ mV/nm, this state (and other symmetry-broken states) is resolved at
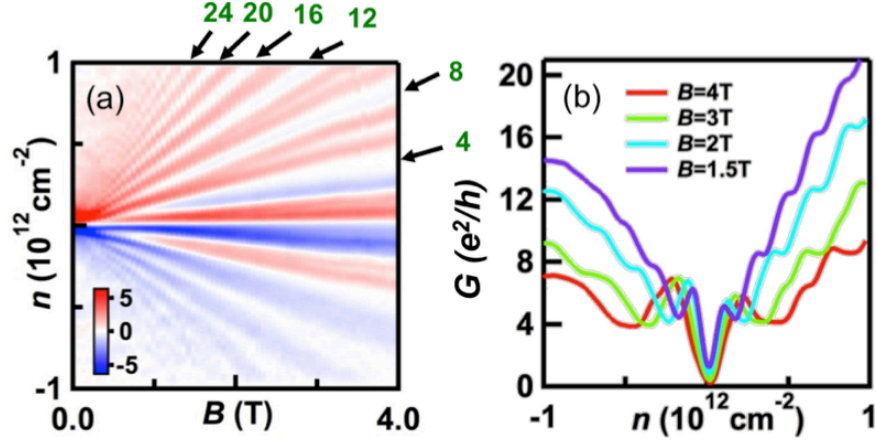
Figure 4.2: (a) Landau Fan diagram of $dG/dn(B,n)$ between $B = 0$ T and 4 T. Arrows and numbers indicate filling factors. (b) $G(n)$ line traces at $B = 1.5$ T, 2 T, 3 T and 4 T, respectively.
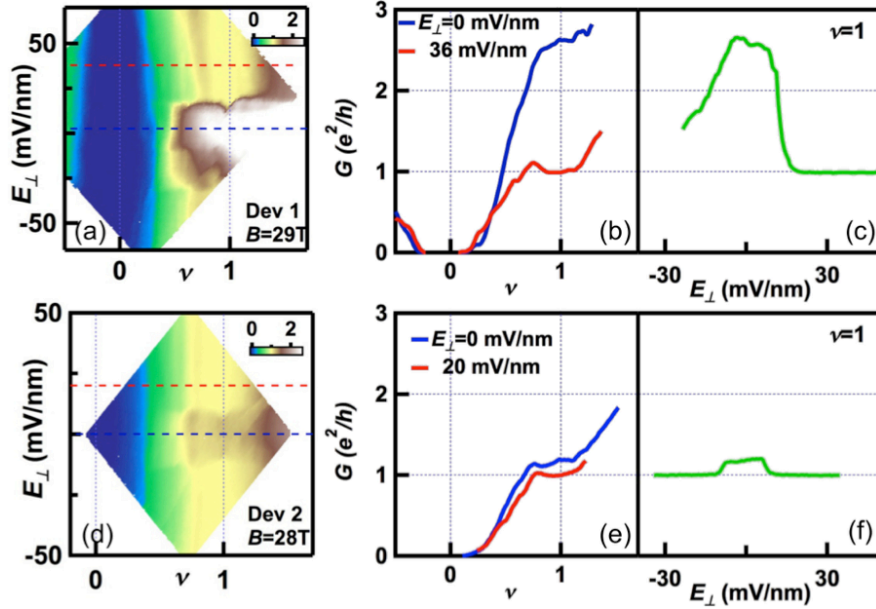
Figure 4.3: (a-c). Data from device 1 at $B = 29$ T: $G(E_\perp, \nu)$, $G(\nu)$ line traces at $E_\perp = 0$ (blue) and 36 mV/nm (red), and $G(E_\perp)$ line trace along $\nu = 1$ (green). (d-f). Data from device 2 at $B = 28$ T: $G(E_\perp, \nu)$, $G(\nu)$ line traces at $E_\perp = 0$ (blue) and 20 mV/nm (red), $G(E_\perp)$ line trace along $\nu = 1$ (green).

B as low as 3.8 T, consistent with prior reports [76], thus suggesting its layer polarization in character [84–86].

Strikingly, for device 2 with higher mobility, at $B = 28$ T, the $\nu = 1$ state is resolved at both zero and finite $E_\perp$ (Fig. 4.3d-f). Two regions with $G \sim 1 \, e^2/h$ are visible, connected by an abrupt transition as $E_\perp$ is varied (Fig. 4.3e-f). Its resolution at $E_\perp = 0$ is unexpected, and points to the formation of a hitherto unobserved $\nu = 1$ state that is layer balanced. Our observations thus suggest the existence of two distinct phases at $\nu = 1$: phase I is layer balanced, and appears at large B and near $E_\perp = 0$; phase II is layer polarized, as it is resolved at relatively small B, provided that $E_\perp$ exceeds certain critical value. The quantization of phase II is better than that of phase I, as seen in Fig. 4.3f. We note that the $\nu = 1$ states observed in previous works almost exclusively correspond to phase II, whereas phase I has not been reported before.

To explore these two distinct phases, we measure the scaling of their LL gaps on B by using the source-drain bias V as a spectroscopic tool [72,83], which has been applied to measuring the gaps of the single particle $\nu = 4$ state [72] and the two competing correlated $\nu = 2$ states in BLG [83]. Fig. 4.4a plots $G(V, E_\perp)$ for device 2. The bright white/brown area near $E_\perp = 0$ corresponds to the layer-balanced phase I, which abruptly gives way to the blue regions at larger $|E_\perp|$ that corresponds to the layer-polarized phase II. The line traces $G(V)$ at $E_\perp = 0$ and -20 mV/nm are shown in Fig. 4.4b. Both display conductance valleys, yet their widths differ considerably. The LL gaps are extracted by measuring the full width at half maximum (FWHM) of the valley, which is fitted to a Gaussian function. The resultant values are shown in Fig. 4.4c as functions of B. For the layer polarized phase
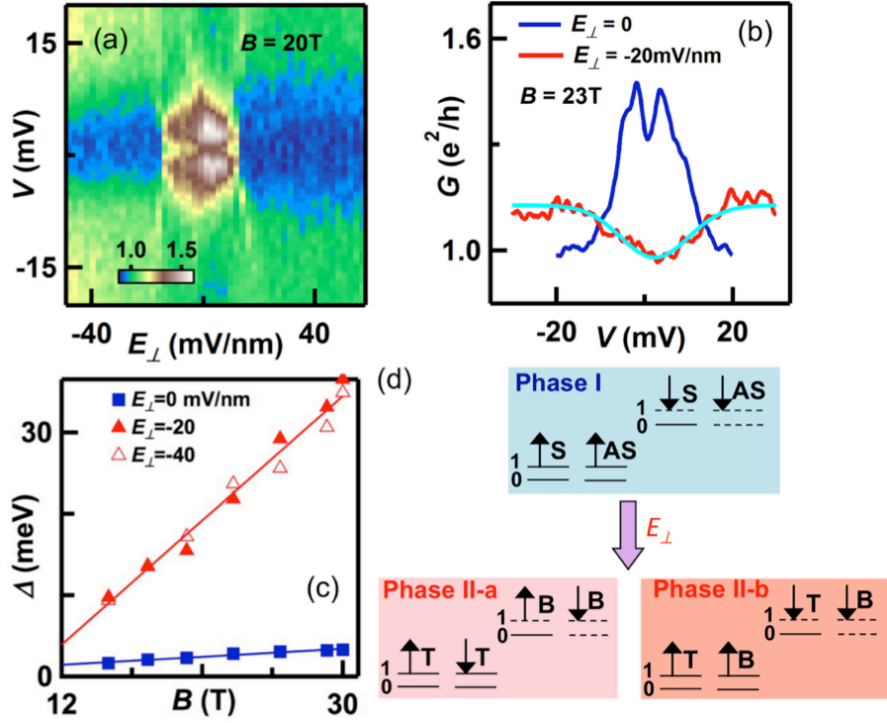
Figure 4.4: (a) $G(V, E_\perp)$ of Device 2 at $B = 20$ T. (b) $G(V)$ line traces at $E_\perp = 0$ and $E_\perp$ = -20 mV/nm at 23 T. (c) Measured LL gap $\triangle(B)$ at $E_\perp = 0$ (blue) and $E_\perp$ = -20 mV/nm and -40 mV/nm (red) respectively. (d). Schematics of electronic configurations of the different $\nu = 1$ phases. T: top layer; B: Bottom layer. S (AS): their symmetric (anti-symmetric) combination. The numbers 0 and 1 are the orbital indices. The solid (dotted) lines represent occupied (empty) levels.

II, the LL gap scales linearly with B as $\triangle_{II}(B) \sim 1.6$ meV/T, consistent with a previous work [78]. Rather unexpectedly, it appears that $\triangle_{II}$ has little or no dependence on $E_\perp$, as data at $E_\perp = $ -20 and -40 mV/nm yield almost identical results. In contrast, the LL gap of phase I at $E_\perp = 0$ is at least one order of magnitude smaller, though it also scales linearly with B as $\triangle_I(B) \sim 0.1$ meV/T.

Our experiments provide the first measurement of the LL gap for the $\nu = 1$ state with controlled $E_\perp$. The layer balanced phase I is observed here for the first time, and is most likely a coherent linear combination of the top and bottom layers, or equivalently, K and K' valleys, since it is stable at $E_\perp = 0$. Phase II is only resolved for $E_\perp > E_{\perp c}$, which is $\sim$ 15 mV/nm at $B = 20$ T, and is evidently layer polarized. Phase II is likely the one observed in singly-gated devices [76, 78] (with the possible exception of the low field data in ref. [75]). Both phases at $\nu = 1$ are interactions induced QH ferromagnetic states [78, 80, 81, 87], and correspond to filling one of the two levels in an orbital doublet (LL index $N = $ 0,1) that has the same spin-valley index. They are energetically favored by gaining exchange energies that approximately scale as $e^2/l_B^2 \sim B$ for screened Coulomb interactions. More exchange energies are gained when a LL is layer polarized, as the intra-layer exchange is generally larger than the inter-layer exchange. These two features qualitatively explain the observed linear B dependence of $\triangle_I$ and $\triangle_{II}$, their relative magnitudes $\triangle_I < \triangle_{II}$, and the better quantization of phase II.

We now discuss the microscopic nature of the two phases at $\nu = 1$. In the lowest LL, while the orbital degeneracy must be broken, the relative order and magnitude of polarizing the real spin and the layer/valley pseudospin characterize the corresponding

phase. Phase I that appears at large B and vanishing $E_\perp$ can be uniquely determined [86] (Fig. 4.4d, upper panel); the real spin polarization is maximized whereas for each occupied LL the pseudospin is layer/valley symmetric or antisymmetric. On the other hand, there are two possible candidates for phase II [76, 84, 86]. In the first scenario depicted as Phase II-a, the pseudospin may be maximized first because of the presence of large $E_\perp$, followed by the maximization of real spin in the last occupied $N = 0$ LL. Alternatively, in the second scenario of Phase II-b, which similar to that proposed in ref. [76], the real spin may be maximized first because of the presence of large B, followed by the maximization of pseudospin in the last filled $N = 0$ LL. Both candidates of phase II are pseudospin and spin polarized, albeit the former has a larger pseudospin polarization while the latter has a larger real spin polarization. Further experiments will be necessary to determine which candidate corresponds to the observed phase II and to explore the possible quantum phase transition between the two candidates.

The observation of the two phases, one appearing at small $E_\perp$ and large B and one resolved at small B and stabilized by large $E_\perp$, is reminiscent of the two competing phases of the $\nu = 2$ state [83], though with one important distinction: the gap of the layer polarized $\nu = 2$ state extrapolates a finite intercept at $B = 0$, whereas both phases of the $\nu = 1$ state appear to extrapolate vanishing gaps at $B = 0$. The former feature is consistent with the fact that the layer polarized $\nu = 2$ state survives to anomalously weak B and adiabatically connects to the spontaneous QH state in BLG at $B = 0$ with the same Hall conductivity [88] . In contrast, similar correspondence is absent for the $\nu = 1$ state, which requires a splitting between the $N = 0$ and $N = 1$ LLs and thus has no counterpart in

the $B = 0$ limit. Therefore, both phases of the $\nu = 1$ state are only resolved above their corresponding critical magnetic fields.

4.3   Fractional $\nu = 2/3$ state
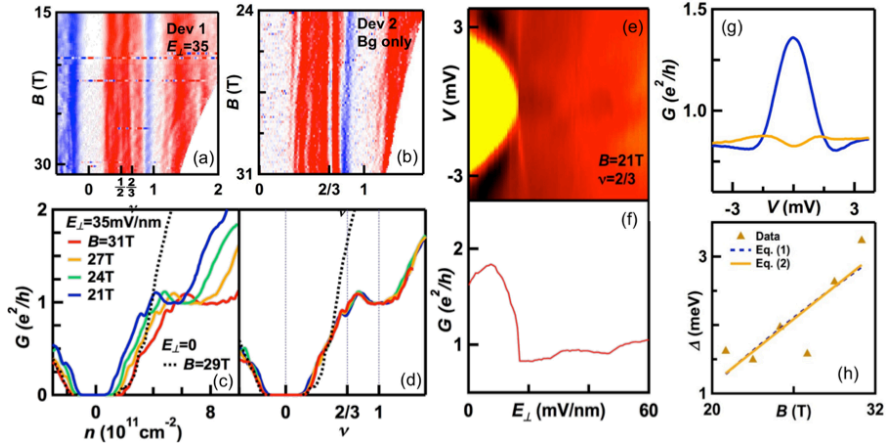
Figure 4.5: (a) $G(B, \nu)$ of device 1 at $E_\perp = 35$ mV/nm. (b) $G(B, \nu)$ of device 2 with back gate only. (c) Line traces $G(n)$ at $E_\perp = 35$ mV/nm and $B = 21$ T, 24 T, 27 T, 31 T. (d) Plotted $G(\nu)$ of the line traces in figure (c) The dot lines in figure (c) and (d) are the G data of device 1 at $E_\perp = 0$ and $B = 29$ T. (e) $G(V, E_\perp)$ of device 2 at $B = 21$ T and $\nu = 2/3$. (f) Line trace of $G(E_\perp)$ at $V = 0$. (g) Line traces of $G(V)$ at $E_\perp = 17$ mV/nm (blue) and $E_\perp = 25$ mV/nm (brown). (h) LL gap of $\nu = 2/3$ state versus B field. Symbols: data. Blue dot line and brown solid lines are fits using linear B and $\sqrt{B}$ dependences, respectively.

We now turn to the fractional QH state at $\nu = 2/3$. Similar to the $\nu = 1$ state, it is strongly dependent on $E_\perp$. At $E_\perp = 0$, it is unresolved even at the highest attainable field $B = 31$ T. However, it is resolved in the presence of an interlayer potential that breaks the inversion symmetry. Fig. 4.5a plots the differentiated conductance $dG/dn(B, \nu)$ of device 1 at $E_\perp = 35$ mV/nm. The QH plateaus appear as vertical white strips centered at various given ν. Apart from the complete lifting of the 8-fold degeneracy of the lowest LL, features between $\nu = 0$ and 1 are also observed – in particular, thin vertical strips at $\nu = 1/2$ and

2/3 are evident. These features are more clearly visible in Fig. 4.5 c, which displays the line

traces $G(n)$ curves at $B = 21$, 24, 27 and 31 T, where a small plateau at $\nu = 2/3$ appears.

These curves collapse into a single curve when plotted as $G(\nu)$ (Fig. 4.5d). This is in sharp

contrast to the line trace at $E_\perp = 0$ (Fig. 4.5c-d, dotted line), in which only $\nu = 0$ and

$\nu = 2$ plateaus are resolved (for device 1). We note that the conductance is not perfectly

quantized, presumably due to the non-zero σ_{xx} signals (common for FQH states with small

charge gaps) that are included in the two-terminal measurements.

A similar data set exhibiting the $\nu = 2/3$ QH state in device 2 is shown in Fig.

4.5b, which plots $dG/dV_{bg}(B, \nu)$ for $B = 24$ to 31 T. Here only the back gate is engaged;

thus at finite densities, partial screening by electrons on the bottom layer leads to charge

imbalance and hence finite interlayer $E_\perp$, which estimated to be ~ 35 - 45 mV/nm for the

measurement. The observation of a clear FQH state at $\nu = 2/3$ is consistent with data from

device 1, namely, the $\nu = 2/3$ state is only resolved at finite $E_\perp$, and in agreement with a

previous work [76].

To further explore the field dependence of the $\nu = 2/3$ fractional QH state, we

measure $G(V, E_\perp)$ at $B = 21$ T and $\nu = 2/3$ for device 1 (Fig. 4.5 e). At $E_\perp = 0$, $G \sim$

2 e^2/h, indicating that neither $\nu = 1$ nor $\nu = 2/3$ states are resolved, as discussed above;

as $E_\perp$ exceeds a critical value ($E_{\perp c} \sim 17$ mV/nm), G drops abruptly to ~ 0.7 e^2/h (Fig.

4.5f). Such a dramatic transition in G induced by $E_\perp$ is rather similar to that of the $\nu =$

1 state, though their critical $E_\perp$ values differ. We note that a similar $E_\perp$ induced transition

has been observed [76]; what sets our work apart is that, due to the higher resolution of our

data, what appeared as a single transition point at $E_\perp = 0$ in ref. [76] is resolved to be a

broadened plateau with well-defined $E_\perp c$ values, hence clarifying the necessity to support

the $\nu = 2/3$ state.

At $\nu = 2/3$, for $E_\perp$ below (exceeds) $E_{\perp c}$, the $G(V)$ curves display zero bias con-

ductance peaks (valleys), indicating that the fractional QH state is unresolved (resolved)

(Fig. 4.5 g). The LL gap $\triangle_{2/3}$ is extracted by measuring the FWHM of the resolved

conductance valley at different B and constant $E_\perp = 35$ mV/nm. The resultant values,

as plotted in Fig. 4.5h, are consistent with linear B dependence, with the best-fit equa-

tion, $\triangle(B) = -2.03 + 0.16B[T]$ meV. However, due to the limited range in B, a $\sqrt{B}$

dependence cannot be definitively ruled out, where the data points may also be fitted to

$\triangle(B) = -6.0 + 1.6\sqrt{(B[T])}$ meV; other functional dependence may also be possible.

In the standard picture, the FQH states arise from the quench of kinetic energy

by a strong magnetic field and the presence of electron-electron interactions. The negative

intercepts at $B=0$ reflects the former requirement. For long-range Coulomb interactions

the FQH gaps are expected to scale with $e^2/l_B \sim \sqrt{B}$. The possible linear B dependence

is related to the strong screening of Coulomb interactions that yields similar gaps scaling

with $e^2/l_B^2 \sim B$ of the integer symmetry-broken QH states in BLG. For instance, similar

linear B dependence are observed above for both phases of the $\nu = 2$ state. Future experi-

ments in higher-mobility samples at larger fields will be necessary to confirm whether there

exist multiple phases at $\nu = 2/3$ [76] and whether the composite fermions undergo similar

transitions in real spin and pseudospin polarizations to those electrons in the $N = 0$ LL of

the $\nu = 1$ state.

4.4 Compararation with previous results

Table 4.1: Experimentally measured LL gaps $\triangle_1$ and $\triangle_{2/3}$ from this and other works.

Reference	Device		$\triangle_{\nu=1}$	$\triangle_{\nu=2/3}$
[75]	Single gate on hBN		0.35 meV/T[*]	0.1 meV/T [+]
[79]	Single gate, suspended		0.1 meV/T	
[78]	Dual gates on hBN, $E_\perp$ uncontrolled		1.75 meV/T	
This Work	Dual gates, suspended	$E_\perp = 0$	0.1 meV/T (electron)	unresolved
		Finite $E_\perp$	1.64 meV/T	0.16 meV/T

[*] Estimated from Fig. 3B in Ref. [75], [+] Estimated from Fig. 3A (B=9T to 12T) in Ref. [75]

It is instructive to compare the measured gaps of the $\nu = 1$ and $\nu = 2/3$ QH states with prior results [75, 78], as summarized in Table 4.1. Prior measurements were performed on singly-gated samples, in which any finite charge density induced by the gate produces an electric field across the bilayer, due to partial screening by the layer that is closer to the gate. Such inadvertent $E_\perp$ scales linearly with charge density n; in the QH regime, $E_\perp$ (in units of mV/nm) is approximately $\sim 2.2B\nu$. Since a large B is usually required to resolve the $\nu = 1$ and 2/3 states, the inadvertently induced $E_\perp$ in singly-gated devices almost always exceeds the critical values $E_{\perp c}$ for states at both filling factors ($\sim 10 - 20$ mV/nm). In other words, singly-gated devices are almost always in phase II. As seen in Table 4.1, our $E_\perp$-controlled measurements of both the $\nu = 1$ and the $\nu = 2/3$ states at finite $E_\perp$ are in good agreement with the prior works on singly-gated devices.

An exception to the above scenario is ref. [75], which is able to resolve integer and fractional QH states at relatively small B (4 T to 12 T) in singly-gated samples; here, at a given filling factor, as B increase, n hence $E_\perp$ also increases, and the integer and fractional QH gaps likely undergo a transition between the layer coherent phase I (with a smaller gap)

and layer polarized phase II (with a larger gap), thus giving rise to an apparent superlinear dependence on B.

4.5 Possible $\nu = 1/2$ state

Finally, we note that our data exhibit a tantalizing feature at $\nu = 1/2$, which appears as a thin white band in Fig. 4.5b and a small kink in the line traces; similar to the $\nu = 2/3$ state, it disappears at $E_\perp = 0$. Simply to compare their orbital nature, the $\nu = 1/2$ state in BLG is likely similar to the $\nu = 1/2$ state in conventional GaAs/AlGaAs heterostructures, in sharp contrast to the observed $\nu = -1/2$ state in BLG which might be described by the non-Abelian Moore-Read state [77, 89]. However, in the case of GaAs/AlGaAs heterostructures, the $\nu = 1/2$ state is a Fermi liquid instead of a QH state. Since the two-terminal geometry of our devices convolves longitudinal and transverse signals, we are unable to conclusively determine whether a QH state is evident at $\nu = 1/2$ or to relate the observed dependence on $E_\perp$ to a Fermi liquid. We note that a feature at $\nu = 1/2$ state has recently been observed in singly-gated devices using a transconductance fluctuation technique [90], though its nature was similarly undetermined. Further experimental studies will be necessary to explore its dependence on $E_\perp$ and to ascertain the nature of this intriguing even-denominator state.

4.6 Conclusion

To summarize, in high mobility suspended BLG samples we observe two distinct $\nu = 1$ states and one $\nu = 2/3$ state. At $\nu = 1$, phase I is resolved at small $E_\perp$ and large B,

with a LL gap of 0.1 meV/T and possible interlayer coherence; phase II is resolved at weak B and large $E_\perp > \sim$ -10 mV/nm, with a much larger LL gap of 1.6 meV/T and at least partial layer polarization. For the $\nu = 2/3$ state, a similar dependence on $E_\perp$ is observed, though the state is only resolved for $E_\perp > \sim$ 20 mV/nm, with a LL gap that rises from 1.2 to 2.8 meV as B increases from 20 to 30 T. Our data are consistent with prior results [75,78] and can also account for the super-linear dependence of the LL gaps observed [75]

Chapter 5

Trigonal Warping and Landau Level Crossings in Boron Nitride Encapsulated Bernal-stacked Tetralayer Graphene

Few-layer graphene has proved to be a fascinating platform to study the quantum Hall (QH) physics [7,8,42,58,59,61]. Among the possible stacking orders, Bernal- or ABA-stacking is the most stable and most commonly found stacking in bulk graphite [34]. In chapter 2, we introduced the theory underlying Bernal-stacked bilayer graphene (BLG), and demonstrated that BLG has a massive parabolic energy dispersion. In chapter 4, we presented transport measurements in BLG with controlled layer polarization, and highlighted

the importance of the interplay between layer polarization and symmetries (spin, valley and orbital) to understand the unusual QH system of BLG.

How about thicker graphene? Trilayer graphene (TLG) also turns out to be exceedingly interesting. For instance, my colleagues Yongjin Lee *et al* have demonstrated the presence of an interaction-induced gap in ABC-stacked TLG [91], and Petr Stepanov *et al* have shown rich Landau level (LL) crossing patterns in ABA-stacked TLG [59]. Going one step further, here we examine the properties of tetralayer graphene. As discussed in chapter 2, the band structure of Bernal-stacked tetralayer graphene can be decomposed into two BLG-like bands with light and heavy effective masses, which are hybridized due to the *next-nearest-layer* hopping terms [35]. Additionally, the hopping term γ_3 gives rise to trigonal warping, which is responsible for the unusual transport behaviors at zero magnetic field. In the QH regime, the LLs of the two BLG-like bands give rise to rich crossing features and quantum phases.

In this chapter, I will present our studies of the quantum transport of tetralayer graphene. We observed similar results from four devices, and I will focus on the data set from one device.

5.1 Device fabrication and characterization

Hexagonal boron nitride (hBN)-encapsulated tetralayer graphene sandwich heterostructures are fabricated using the pickup technique described in chapter 3. Thick (15-30 nm) hBN flakes and tetralayer graphene sheets are obtained by mechanical exfoliation from bulk crystals. The number of layers of a graphene sheet is identified via the optical contrast
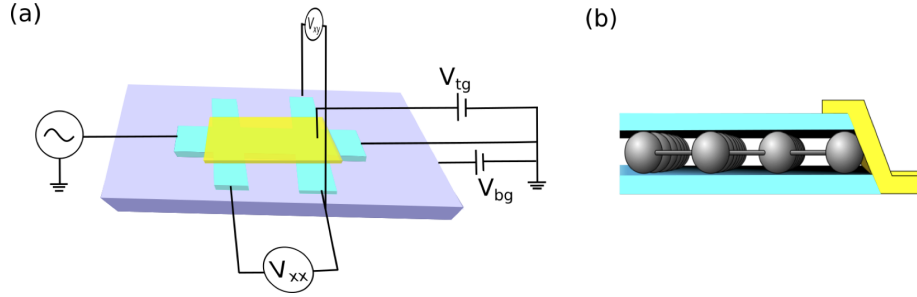
Figure 5.1: (a) Schematic of devices and measurement setup. 50 nA ac source current, provided by a SR830 lock-in amplifier, is injected from source to drain (grounded) electrodes. V_{xx} measures the longitudinal voltage drop, and V_{xy} measures the transverse voltage drop. Gate voltages V_{tg} and V_{bg} are applied by Keithley 2400 voltage source meters. (b) Schematic of one-dimensional edge contacts.

under an optical microscope [3] and Raman spectroscopy; the latter is also used to determine the stacking order of the graphene sheets. Dry pickup transfer technique is applied to assemble hBN/graphene/hBN sandwich heterostructures, followed by the standard e-beam lithography to define the Hall bar geometry and e-beam evaporation to couple to Cr/Au electrodes via one-dimensional edge contacts [45]. Finally, top gates consisting of 50 nm of Al_2O_3 gate dielectric and Cr/Au (10/80 nm) are deposited. The degenerately doped silicon substrates serve as back gates. The schematic of devices and measurement setup is shown in Fig. 5.1a. Fig. 5.1b sketches the one-dimensional edge contact between the graphene sheets and metal electrodes. To measure the devices, we inject a 50 nA ac source current at 17 Hz from the source electrode, while the drain is grounded. Two SR830 lock-in voltage amplifiers are used to measure the longitudinal (V_{xx}) and transverse (V_{xy}) voltages. Two Keithley 2400 voltage source meters are used to apply the top and back gate voltages. The
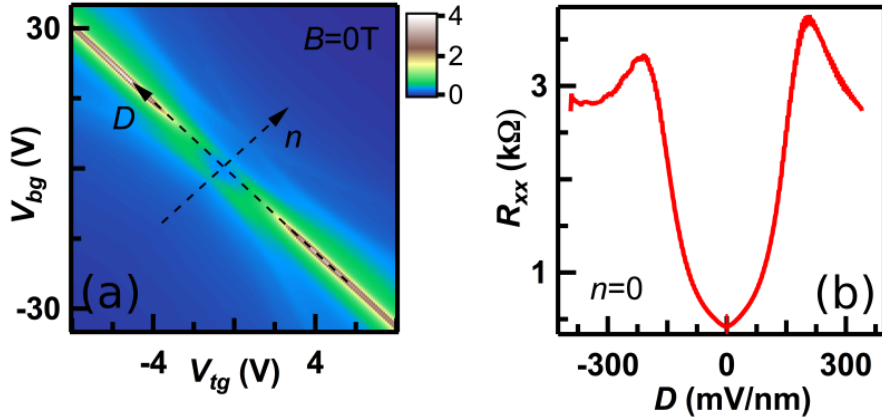
Figure 5.2: (a) Measured $R_{xx}(V_{bg}, V_{tg})$ at zero magnetic field. Dashed lines with arrows indicate the CNP ($n = 0$) and zero displacement field ($D = 0$). (b) Line trace $R_{xx}(D)$ at $n = 0$

devices are measured in a ^{3}He cryostat with base temperature 260 mK and a ^{4}He cryostat with base temperature 1.5 K.

To characterize the device, we first measure the longitudinal resistance R_{xx} as a function of top gate voltage (V_{tg}) and back gate voltage (V_{tg}) (Fig. 5.2a). The black dashed arrows illustrate the lines of $n = 0$ and $D = 0$. Fig. 5.2b shows the evolution of the resistance at the charge neutrality point (CNP) along the displacement field. At $n=0$, $R_{xx}(D)$ is non-monotonic: it firstly increases symmetrically with positive and negative displacement field, indicating the opening of a band gap due to the broken inversion symmetry, and then R_{xx} starts to decrease for larger $D >\sim \pm 170$ mV/nm. We also note that the very symmetric behavior of R_{xx} with respect to $D = 0$ suggests the absence of inadvertently induced D_0, hence indicating low disorder induced charge carrier density n_0.
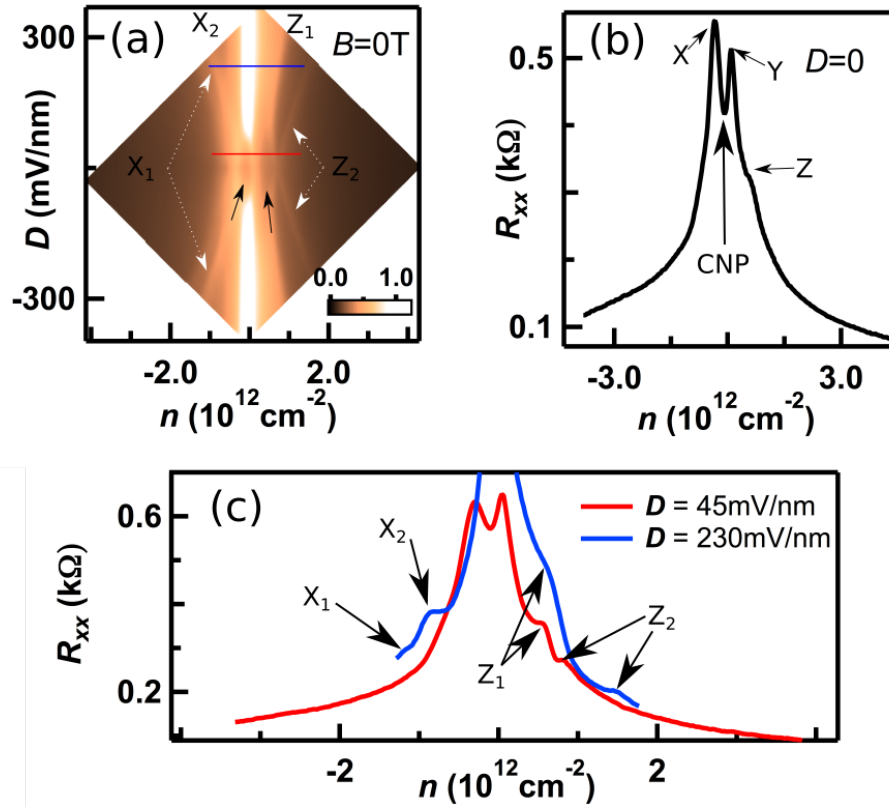
Figure 5.3: Measured $R_{xx}(n, D)$ and line traces. (a) Measured $R_{xx}(n, D)$ in kΩ. Two diamond-shaped pockets are indicated by two black arrows. Solid blue and red lines indicate the line traces plotted in (c). (b) Line trace $R_{xx}(n)$ at D=0. Three peaks are labeled as X, Y and Z. The CNP is the local resistance minimum between peaks X and Y. (c) $R_{xx}(n)$ line traces at $D = 45$ (red) and 230 mV/nm (blue), respectively.

5.2 Unusual transport behaviors at $B = 0$

To have a better view of the data at zero B field, Fig. 5.2a can be replotted as a function of charge carrier density n and displacement field D, as shown in Fig. 5.3a. We observe several unexpected features. Firstly, unlike mono-, bi- and tri-layer graphene, which display sharp resistance peaks at the CNP, $R_{xx}(n)$ of tetralayer graphene displays three peaks, which are labeled as X, Y and Z from left to right, as shown in Fig. 5.3b. Peak X is the most pronounced peak, and Z is present as a small shoulder. Surprisingly, none of these three peaks is located at the CNP. As shown in Fig. 5.3b, the CNP in fact corresponds to a local resistance minimum located between peaks X and Y, as indicated by the black arrow, as determined from the Landau fan in finite magnetic field (see section 5.3). This identification of the CNP with a local resistance minimum is very different from that in thinner graphene devices [7,59,61], where CNP corresponds to a resistance peak. Secondly, near the origin (*i.e.* close to $n = D = 0$), there are two adjacent diamond-shaped pockets, as indicated by the two black arrows in Fig. 5.3a. Thirdly, as indicated in Fig. 5.3a, peak X is split into features X_1 and X_2, and peak Z into Z_1 and Z_2 at larger displacement field. To make the evolutions more clear, we plot $R_{xx}(n)$ line traces at $D = 45$ mV/nm (red), where four peaks are present due to the splitting of peak Z, and at $D = 230$ mV/nm (blue), where resistance is sharply peaked at the CNP due to the opening of a band gap, and two new shoulders X_1 and X_2 emerge from the splitting of peak X, as shown in Fig. 5.3c.

To understande these features, we calculate the band structures of tetralayer graphene using the tight binding method detailed in chapter 2. As shown in Fig. 5.4, the band structure of tetralayer graphene can be decomposed into two BLG-like bands with
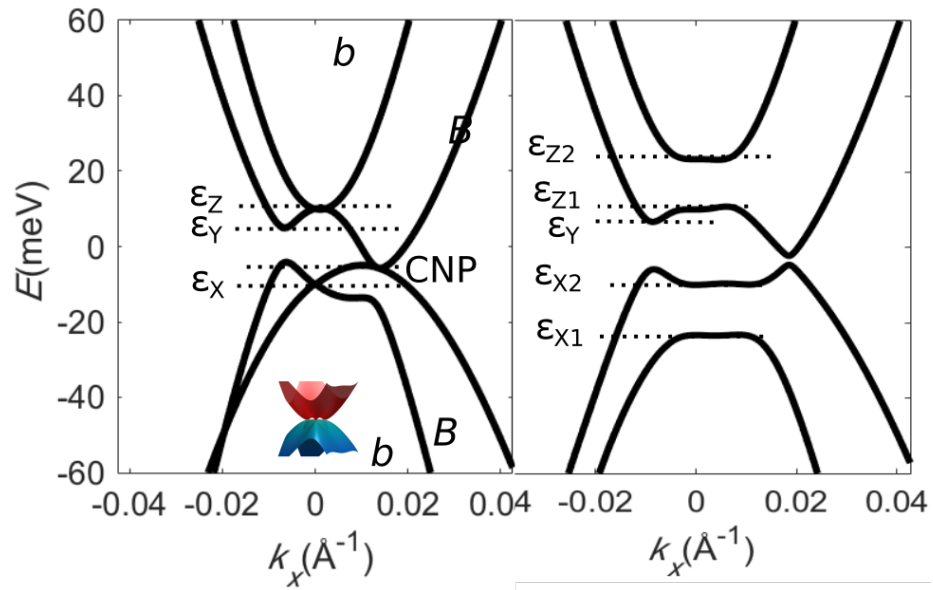
Figure 5.4: Calculated band structures of tetralayer graphene around the K point along k_y=0 at D=0 (left panel) and D=40 mV/nm (right panel). Inset: surface plot of the band structures at D=0. Trigonal warping at the K point is present. Dashed lines and letters correspond to the Fermi levels of the labeled peaks in Fig. 5.3b.
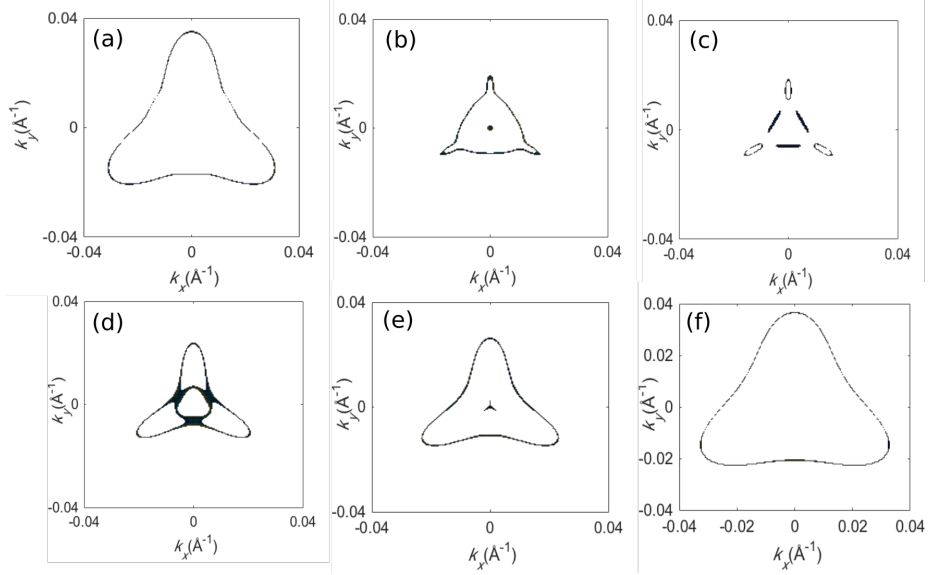
Figure 5.5: Fermi surfaces at different energies at $D=0$. (a) - (f) E_F = -40 meV, ϵ_X (-10 meV), CNP (-3.9 meV), ϵ_Y (5 meV), ϵ_Z (10.7 meV), 40 meV, respectively.

light and heavy effective masses. At finite D (Fig. 5.4 right panel), the two BLG-like bands move apart. In particular, the bottom of the light-mass conduction band moves up, whereas the top of the light-mass valance band moves down in energy, as indicated by the points X and Z in Fig. 5.4. Alignment of the Fermi level with these band edges, which host electrons with very low velocities, provides additional channels for scattering, thus leads to the resistance peaks at the corresponding charge densities.

Moreover, we note that trigonal warping is present in the band structure of tetralayer graphene. The Fermi surfaces at different Fermi energy levels are displayed in Fig. 5.5 (a-f). We attribute the peak X and peak Z in Fig. 5.2b to the Fermi level aligning with ϵ_X and ϵ_Z, respectively, which correspond to the Fermi surfaces shown in Fig. 5.5b and Fig. 5.5e. At these two levels, the topologies of the Fermi surfaces change from singly connected triangles to be elliptical pockets with a hole in the center; such a change in the
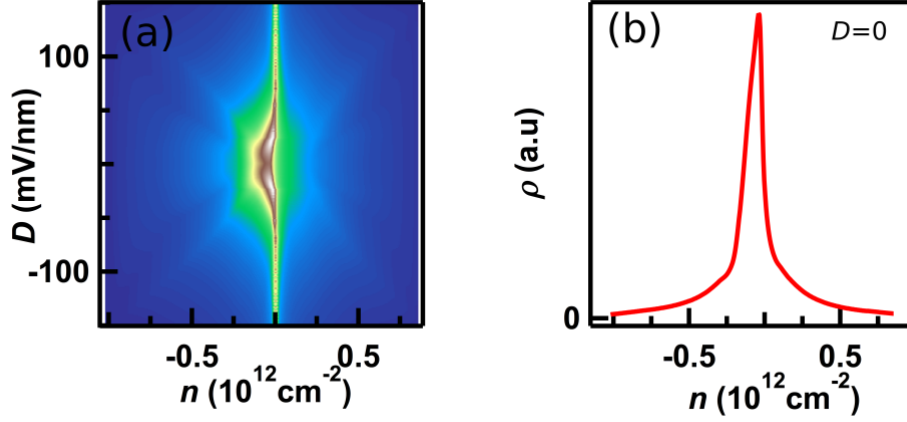
Figure 5.6: (a) Calculated resistivity $\rho(n, D)$ by the Boltzmann transport theory. The inter-band scattering is ignored. (b) Line trace $\rho(n)$ at $D=0$ from (a)

topology of Fermi surfaces is referred to as Lifshitz transitions [92], and may occur as a function of density and strain. This explanation can be confirmed by the features X_1, X_2, Z_1 and Z_2 (Fig. 5.3a) that originate from the splittings of the peaks X and Z at finite D, which in turn arise from the lifting of the accidental degeneracies of ϵ_X and ϵ_Z by D, respectively.

Peak Y can be attributed to the Fermi level aligning with the energy level ϵ_Y, when the Lifshitz transition occurs again, as shown in Fig. 5.5d. By using the Boltzmann transport theory, we are able to calculate the conductivity of tetralayer graphene, hence the resistivity as a function of charge density and displacement field, as shown in Fig. 5.6a. In the simulation, the features X_1, X_2, Z_1 and Z_2 are very well reproduced. However, only one pronounced peak is produced at $n = 0$ at $D = 0$, as shown in Fig. 5.6b, suggesting that additional effects are needed to account for these features.
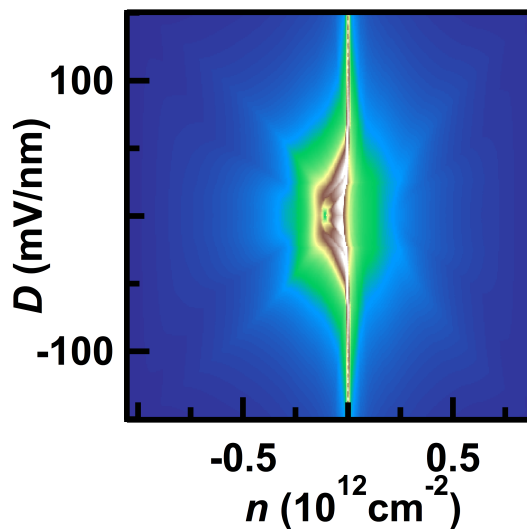
Figure 5.7: Calculated $\rho(n, D)$ with the inter-band scattering included.

Fig. 5.7 displays the simulation with the inter-band scattering included, which produces a local resistivity minimum, suggesting that the inter-band scattering may play an important role in the transport of tetralayer graphene.

5.3 Landau level crossings in tetralayer graphene

For a 2DEG system in a magnetic field that is perpendicular to the plane, electrons' cyclotron orbitals coalesce into LLs. Fig. 5.8 plots the measured longitudinal resistance $R_{xx}(n, B)$ at D=0. All integer QH states at filling factor -8 < ν < 8 as well as the single-particle QH states at -40 < ν < 40 are resolved up to 12 T, indicating the high quality of devices. The filling factors of single-particle QH states jump by 4 as a result of four-fold (valley and spin) degeneracy of each LL. This Landau phase diagram can be construed as
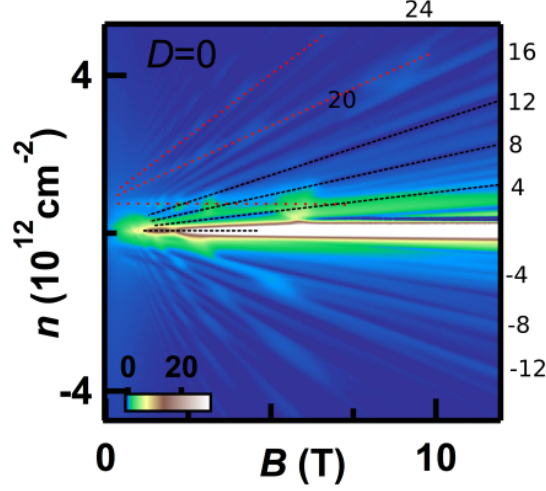
Figure 5.8: Measured $R_{xx}(n, B)$ in kΩ at $D=0$. Numbers indicate the filling factors. Red and black dotted lines are for eye guide of the Landau fan diagrams of light- and heavy-mass BLG-like bands, respectively.

an overlap of two BLG-like bands, fanning out from two different origins, as shown by the red (light mass) and black (heavy mass) dotted lines. This overlap is straightforward to understand since the band structure of tetralayer graphene can be decomposed into two BLG-like bands with different effective masses that are relatively shifted to each other in energy, corresponding to the shift of the fan origins. The heavy-mass diagram fans out from $(n, B) = (0, 0)$, while the light-mass fans out from $(n, B) = (0.78 \times 10^{12}$ cm^{-2}, 0).

To quantitatively account for the Landau fan diagram, we calculate tetarlayer graphene's LL spectrum using the effective mass model, assuming spinless particles, as shown in Fig. 5.9. The fitting parameters are chosen to match the experimental LL crossing points, and are as follows: $\gamma_0 = 3$ eV, $\gamma_1 = 0.39$ eV, $\gamma_3 = 0.3$ eV, $\gamma_4 = 0.04$ eV, $\gamma_2 =$ -16 meV, $\gamma_5 = 60$ meV, $\delta_{AB} = 40.8$ meV, $\delta = 2$ meV. The γ's are Slonczewski-Weiss-McClure parameters of graphite [35, 93], δ_{AB} the potential difference between dimer-site and non-
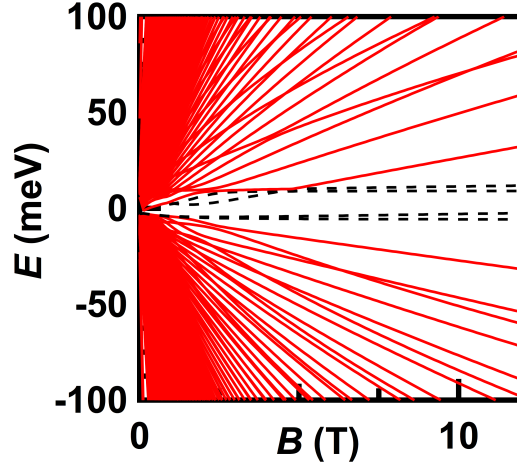
Figure 5.9: Calculated LL spectrum using the effective mass model. LLs from two valleys overlap on each other. The balck dotted line indicate the lowest LLs of two BLG-like bands

dimer-site atoms, and δ the potential difference between the two middle layers and the outside layers. To keep the spatial inversion symmetry, exactly the same δ's are applied to the two middle layers. We introduce a cutoff in LL index $N = 100$, which is enough to obtain the features at low energy regime. As expected, due to the inversion symmetry of the lattice, the valley degeneracy of each LL is not broken. In Fig. 5.9, the LLs are labeled as (b or B, $N_\pm$), where b and B represent the BLG-like bands with light and heavy effective masses, respectively. $N_\pm$ denotes the LL indices. The orbital degeneracies of zero-LLs of two BLG-like bands are weakly split by remote hopping parameters, labeled as (b or B, 0 or -1), with the splitting proportional to B field, as indicated by the black dotted lines in Fig. 5.9. This calculated LL spectrum can explain the experimental data (Fig. 5.8) very well by comparing the LL crossing points' positions. Therefore, the two BLG-like bands in tetralayer graphene's band structures give rise to the rich crossing features.
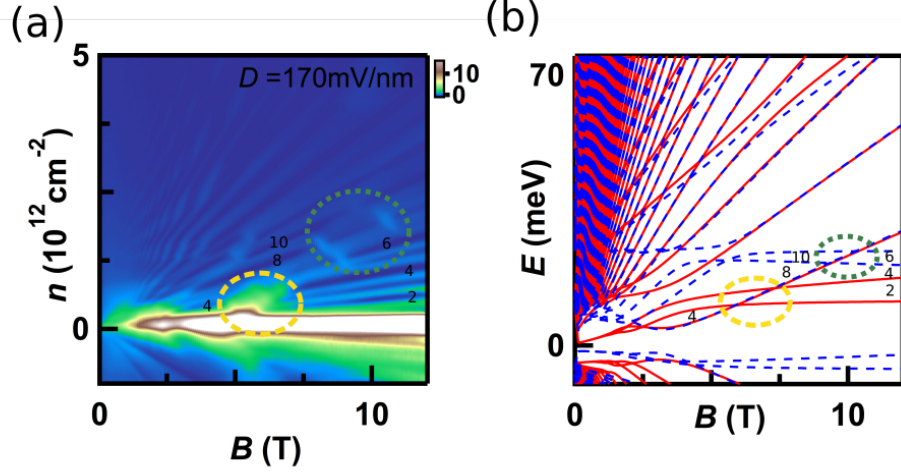
Figure 5.10: (a) Measured $R_{xx}(n, B)$ at $D = 170$ mV/nm. (b) Calculated LL spectrum at $\triangle = 45$ meV. Red solid and blue dashed lines indicate the LLs from the K and K' points, respectively. Yellow and green dotted rings indicate two crossing features that match with each other in experimental and calculated results. Numbers indicate the filling factors.

As discussed above, the band structure of tetralayer graphene can be tuned by applying a perpendicular displacement field D that breaks the valley symmetry. In the QH regime, the LL spectrum and the symmetries of the QH states can be tuned by D as well. To study the effects of D in the QH regime, we measure $R_{xx}(n, B)$ at large D. One representative data set is shown in Fig. 5.10a taken at $D = 170$ mV/nm. Comparing to the data at $D = 0$, one salient difference is the emergence of the crossing feature indicated by the green dotted ring in Fig. 5.10a, which is absent at $D = 0$. The crossing feature indicated by the yellow dotted ring in Fig. 5.10a is also present at $D = 0$ in Fig. 5.8, and can be attributed to the crossings between the zero-LLs of the light-mass band, $(b, 0)$, $(b, -1)$, and the first-LL of the heavy-mass band, $(B, 1+)$. Moreover, the QH states at $\nu = 2$, 6, and 10 are resolved at lower B field than that at $D=0$, indicating the presence of large LL gaps.

To understand these features, we calculate the LL spectrum with an interlayer potential $\triangle$ involved. The potentials applied to each layer from the top to the bottom are $+\triangle/2$, $+\triangle/6$, $-\triangle/6$, $-\triangle/2$ so that the potential differences between two adjacent layers are $\triangle/3$. The calculated results are plotted in Fig. 5.10b, with the corresponding features indicated by green and yellow dotted rings, respectively, and the filling factors by numbers. As shown in Fig. 5.10b, red solid and blue dashed lines indicate the LLs from the K and K' valleys, respectively, which are split by D. The features indicated by the green dotted ring and the yellow dotted ring can be attributed to the crossings of the first-LL of the heavy-mass band with the zero-LLs of the light-mass band from the K' and K valleys, respectively. We also note that the experimental data at $D = 170$ mV/nm is best accounted for by applying $\triangle = 45$ meV, which corresponds to an effective displacement field ~ 45 mV/nm, considering the thickness of tetralayer graphene; the difference between these two values is attributed to screening that reduces the effective interlayer potential.

5.4   Conclusion

As shown by the above results, the electronic transport properties of Bernal-stacked tetralayer graphene at zero and high magnetic fields are non-trivial. At B=0, $R_{xx}(n)$ displays three peaks at $D = 0$ due to the Lifshitz transitions, which can be tuned by the displacement field. Moreover, we suggest that the inter-band scattering may play an important role in the transport of tetralayer graphene. At high magnetic field, the rich LL crossings between the two BLG-like bands are observed, and can be tuned by the perpendicular displacement field as well. By comparing the experimental and calculated

data, we are able to obtain the hopping parameters. Our results provide insight into the understanding of the band structure of tetralayer graphene, and the interplay among the competing symmetries and displacement and magnetic fields.

Chapter 6

Weak Localization and Electron-electron Interactions in Few-layer Black Phosphorus Devices

Graphene's massless linear energy dispersion provides graphene a number of unique material properties, such as high optical transparency [12], high mechanical strength [13] and high thermal conductivity [14], which make graphene an ideal platform for optical, scanned probe, mechanical and thermal measurements and applications. However, the gapless band structure of graphene is a two-edged sword — it endows graphene with high mobility but also makes it unsuitable for direct digital applications. Therefore, researchers soon started to explore other 2-dimensional (2D) semiconductors. One of the latest additions

to the family of 2D materials is phosphorene, which is single- or few- atomic layers of black phosphorus (BP) [15]. Few-layer phosphorene (FLP) has been a highly attractive candidate for electronics, thermal and optoelectronics applications, as well as a model system for interesting physics such as anisotropic quantum Hall effect [25] due to its high mobility [17], direct band gap that is tunable by thickness or strain [17–23], and large in-plane anisotropy [23,24]. Unlike graphene, single layer phosphorene is a semiconductor with a direct bandgap ~ 2 eV; with each added layer, the gap is reduced, eventually reaching ~ 0.3 eV [21] for bulk BP.

In this chapter, I will present magnetotransport studies on hexagonal boron nitride (hBN)-encapsulated FLP devices. Section 6.1 describes the fabrication and characterization of the devices. Section 6.2 presents the weak localization on FLP in low magnetic field, from which we extract the electron dephasing lengths. In section 6.3 and 6.4, we study the dependences of dephasing lengths on temperature and charge density, respectively.

6.1   Device fabrication and charaterization

To fabricate hBN-encapsulated FLP devices, we use the dry transfer technique detailed in chapter 3 . The optical image of a typical device is shown in Figure 6.1a. The devices are measured in a pumped He^4 cryostat with a variable temperature insert. Here we present transport data from two different devices that are ~ 20 nm thick, with mobility up to 1700 cm^2/Vs.

FLP has a thickness-dependent band gap [23]. For FLP that are more than 5 layers, the gap is similar to that of bulk, ~ 0.3 eV [23]. Fig. 6.1b displays the two-terminal
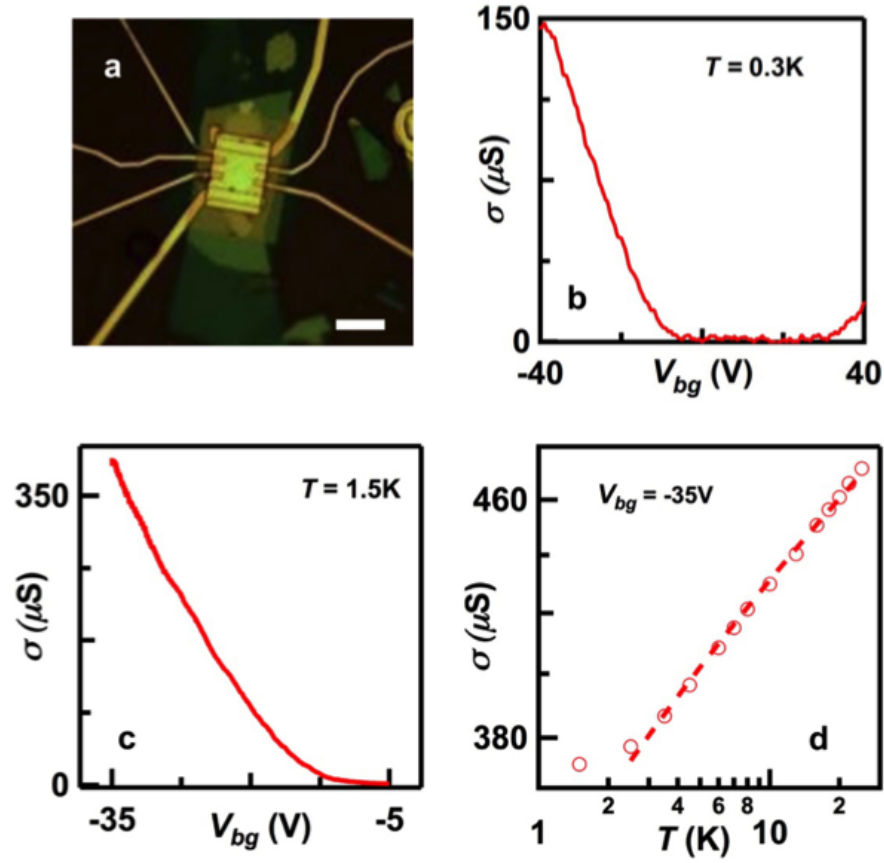
Figure 6.1: (a) An optical image of a typical hBN-encapsulated FLP device with hall bar geometry and a top gate. Scale bar: 10 μm. (b) Two-terminal conductivity as a function of back gate voltage of device A at $T = 0.3$ K. (c) Four-terminal conductivity as function of back gate voltage of device B at $T = 1.5$ K. (d) The conductivity of device B as function of temperature taken at $V_{bg} = $ -35 V. The dashed line is a fit to equation 6.1.

conductivity σ of device A as a function of applied gate voltage (V_g) at $T = 300$ mK, and Fig. 6.1c displays the four-terminal conductivity of device B at $T = 1.5$ K. $\sigma \sim 0$ for both devices, when the Fermi level is within the band gap. For $V_g < $ -15V, σ increases linearly (device A) or superlinearly (device B) with V_g, indicating hole mobility of ~ 500 cm^2/Vs and 1700 cm^2/Vs, respectively. Conductivity of electron-doped regime is significantly lower, which is likely due to the formation of Schottky barriers at electrode-BP interfaces. Hence we focus on transport properties in the p-doped regime.

In the highly p-doped regime, device conductivity significantly exceeds σ_q, where $\sigma_q = e^2/h \sim 39$ μS is the conductance quantum, thus the device is in the metallic regime (here h is Planck's constant, e the electron charge). However, σ decreases slightly with T. This is a signature of electron interactions in disordered 2D thin films. In fact, σ is expected to exhibit a logarithmic dependence on T,

$$\sigma = \sigma_0 + C\frac{2e^2}{\pi h}ln(\frac{T}{T_0})$$ (6.1)

where σ_0 is the "intrinsic" metallic conductivity, T_0 a characteristic temperature estimated to be $\hbar/k_B\tau_0$, k_B the Boltzmann's constant, τ_0 the electron scattering time, and C a dimensionless constant that is of order unity depending on the scattering mechanism [94]. This logarithmic dependence is borne out by experimental data from device B, shown as circles in Fig. 6.1d. At charge density $n \sim -1.75 \times 10^{16}$ m^{-2}, $\sigma_0 \sim 0.4$ mS, and using effective mass $m^\star \sim 0.26m_e$ [28] , τ_0 is estimated from Drude model to be $\sim$0.21 ps, yielding $T_0 \sim$ 36 K. The dashed line is a fit to equation 6.1 with $C \sim 1.6$ as the fitting parameter, in agreement with theory.
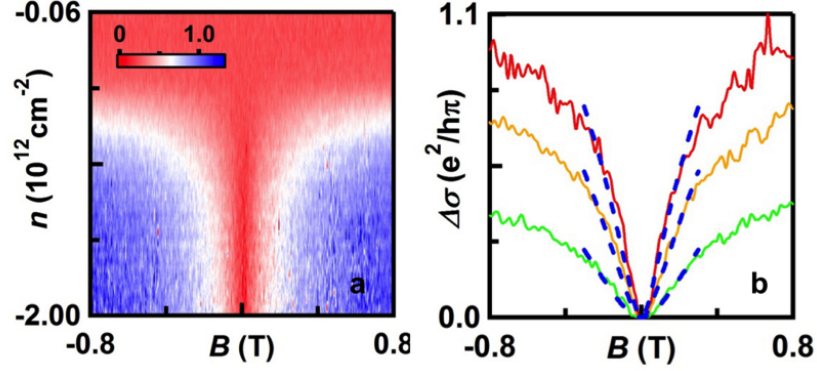
Figure 6.2: Weak localization data from device A. (a). Normalized conductivity $\triangle\sigma$ in units of $e^2/\pi h$ vs. carrier density and magnetic field. Note that below -0.38 × 10 ^{12} cm^{-2} the device no longer displays the suppression of weak localization. This is attributed to the device entering the insulating state. (b) Solid lines: line traces $\triangle\sigma(B)$ at -1.8, -1, and -0.7 × 10 ^{12} cm^{-2}, respectively (top to bottom). Dotted lines: fits to the data using equation 6.2.

6.2 Weak localization in perpendicular B field

To further explore the inelastic scattering mechanism, we employ weak localization (WL) measurements by applying a perpendicular magnetic field B. As detailed in chapter 2, WL is the quantum correction to the classical conductivity of a diffusive system [36, 37]. In a 2D system, due to multiple inelastic scatterings, electrons in a closed trajectory interfere constructively with the time-reversed path, resulting in enhanced backscattering and hence lower conductivity. Application of a small B destroys the interference, thus conductivity increases. WL has been widely applied to 2D systems for measuring the inelastic scattering time, characterized by the dephasing time τ_ψ. When the elastic scattering time is much shorter than the inelastic scattering time, the change in magnetoconductance induced by B

is given by [37, 95]

$$\triangle\sigma = \sigma(B) - \sigma(B = 0) = -\frac{e^2}{\pi h}[ln(\frac{B_\psi}{B}) - \Psi(\frac{1}{2} + \frac{B_\psi}{B})] \qquad (6.2)$$

where σ is the device conductivity, h Planck's constant, e the electron charge, Ψ the digamma function, $B_\psi = \frac{\hbar}{4eL_\psi^2}$ the magnetic field required to destroy phase coherence. $L_\psi = \sqrt{D\tau_\psi}$, and D is the diffusion coefficient.

Figure 6.2a displays the normalized conductivity $\triangle\sigma$ in units of $e^2/(\pi h)$ (color) as a function of n (vertical axis) and B (horizontal axis). As B is swept from -0.8 T to +0.8 T, $\triangle\sigma$ displays positive magnetoconductivity with a minimum at $B = 0$ T, consistent with the time reversal symmetry breaking of phase coherent back scattering. The magnitude of $\triangle\sigma$ is relatively large (> 1) when the device is highly doped, and small (< 0.1) when the Fermi level is close to the band edge. Representative line traces $\triangle\sigma(n)$ are shown as solid lines in Fig. 6.2b, and the dashed lines are fits using equation 6.2. Satisfactory agreement between the data and equation 6.2 are obtained. From the fitting parameter B_ψ, we obtain $L_\psi \sim 75$ nm at $n = -1.8 \times 10^{12}$ cm^{-2}. Using $D = \frac{\hbar}{4m^*}\frac{\sigma}{\sigma_q} \sim 4.3 \times 10^{-4}$ m^2/s, the inelastic scattering time is estimated to be $\tau_\psi \sim 13$ ps, which is two orders of magnitude longer than the elastic scattering time τ_0. This is consistent with the applicability condition of equation 6.2, and establishes that charge transport in these FLP devices is diffusive but phase coherent over tens of nanometers. Similar calculations yield that, at $n = -1.0$ and -0.7×10^{12}cm^{-2}, $L_\psi \sim 60$ nm and 40 nm and $\tau_\psi \sim 8.4$ ps and 3.7 ps, respectively.
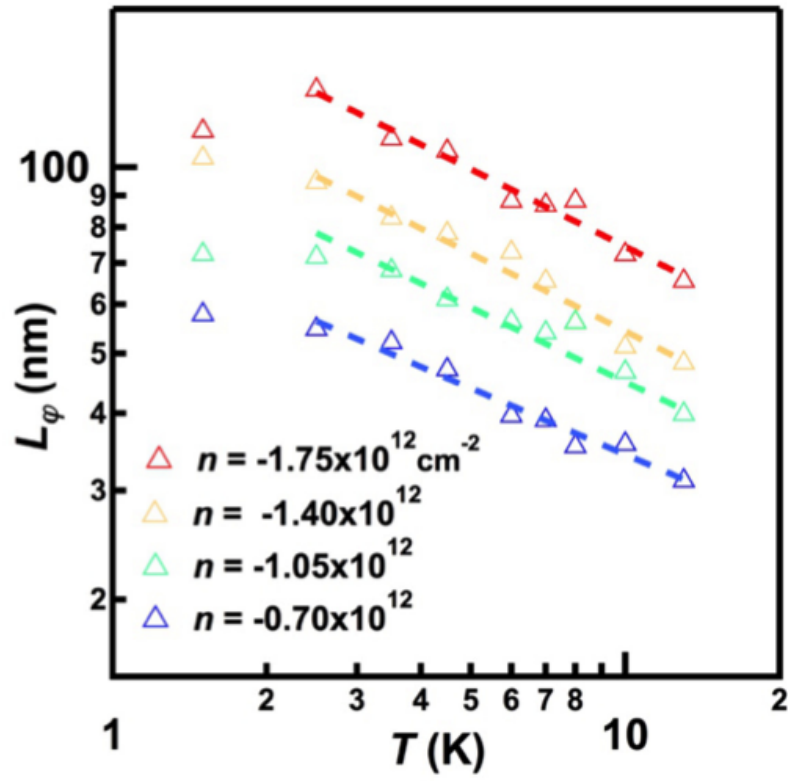
Figure 6.3: Temperature dependence of dephasing length of device B at different hole densities. Dashed lines are fits to power-law dependence $T^{-0.4}$

6.3 Dependence of dephasing lengths on temperature

To explore the scattering mechanism, we examine the temperature dependence of L_ψ in device B. In general, the dephasing time $\tau_\psi \sim T^{-\alpha}$, where the exponent α depends on the scattering mechanisms. In particular, $\alpha \sim 3$ for electron-phonon scattering. On the other hand, if electron-electron interaction is the dominant mechanism, two separate processes may occur depending on the impurity density of the system [37, 96]—the first involves direct scattering between electrons and large momentum transfer, with a rate that scales with $(k_B T)^2$, so $\alpha = 2$; the second process involves small momentum transfer, and considers not individual collision events but instead the interaction of an electron with the fluctuating electromagnetic environment produced by the movement of other electrons. The latter process is similar to that in the Nyquist noise, with a rate that scales linearly with $k_B T$ in 2D, hence $\alpha = 1$ [37].

Figure 6.3 displays $L_\psi(T)$ at four different hole densities. As expected, L_ψ increases as T decreases from 15 K to 2 K, then saturates for $T < 2$K. We fit the data points above 2 K to a power law dependence $L_\psi \sim T^{-\beta}$. The measured values of $\beta = \alpha/2$ are found to be $\sim 0.4 \pm 0.02$ for all densities, which is close to the value of $\beta = 0.5$ or $\alpha = 1$ expected from the theory of electronic interactions with small momentum transfer. Quantitatively, the Altshuler-Aronov-Khmelnitsky theory predicts $\frac{\hbar}{\tau_\psi} = \frac{k_B T}{\sigma/\sigma_q} ln(\sigma/\sigma_q)$ [37]. Combined with the expression for D, the dephasing length is given by

$$L_\psi = \frac{\hbar\sigma}{\sigma_q}[ln(\sigma/\sigma_q)4m^*k_B T]^{-1/2} \tag{6.3}$$

From equation 6.1, σ exhibits a weak logarithmic dependence on T, thus L_ψ should scale with $T^{-1/2}ln(T)$, and the $ln(T)$ term accounts for the observed deviation of β from the
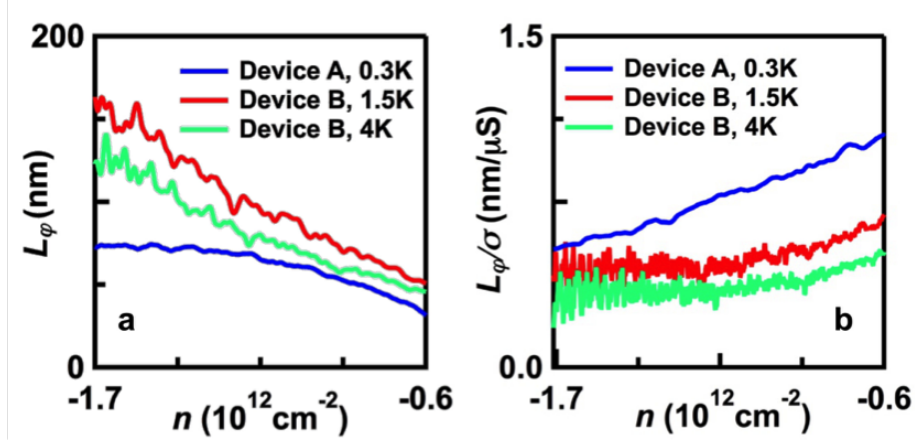
Figure 6.4: (a) The dependence of dephasing length L_ψ on carrier density from Device A at 0.3 K(blue), and Device B at 1.5 K (red) and 4 K (green) respectively. (b) $L_\psi/\sigma(n)$ for the devices, where σ is taken from $B = 0$ measurements.

expected value of 0.5. Thus the $L_\psi(T)$ data establish that the main dephasing mechanism at low temperatures arises from electron-electron interactions with small momentum transfer, though the saturation of L_ψ at $T < 2$ K may suggest a different mechanism at ultra-low temperatures.

6.4 Dependence of dephasing lengths on carrier density

Lastly, we explore the dependence of L_ψ on charge density. Fig. 6.4a plots $L_\psi(n)$ for device A at $T = 0.3$ K, and that for device B at $T = 1.5$ K and 4 K. Clearly, L_ψ is strongly dependent on carrier density, varying by almost 1 order of magnitude from 30 nm to 110 nm when n increases from 0.5 to 2×10^{12} cm^{-2}. In fact, L_ψ appears to have a power-law dependence on n, $L_\psi \sim n^p$, where p appears to be less than 1 for device A at $T = 300$ mK, and ~ 1.5 and 2 for device B at $T = 1.5$ K and 4 K, respectively.

Such $L_\psi(n)$ dependence can be readily understood from equation 6.3 , which shows that $L_\psi(n)$ should be slightly superlinear in σ, and the latter is in turn linear or superlinear in n. This is explicitly verified by plotting L_ψ/σ for device A at $T = 0.3$ K and device B at $T = 1.5$K and 4 K, respectively (Fig.6.4b). All 3 curves are relatively independent of n at relatively high hole density. The slight rises in the curves at lower carrier density are attributed to the larger Schottky barriers and increasing contact resistance towards the band edge. This deviation is largest in the two-terminal data of Device A, and much smaller but still present in the *invasive* four-terminal data of Device B. Taken together, these results again confirm that inelastic scattering processes at low temperature in FLP are dominated by electron-electron interactions

6.5 Conclusion

In short, we have observed the weak localization in hBN-encapsulated FLP devices. The dephasing length is measured to be ~ 30 to 100 nm, and exhibits power-law dependences on temperature and charge density. Our results demonstrate that the main dephasing mechanism in these few-layer BP devices is the electron-electron interactions. A recent work [97] on FLP devices on Si/SiO_2 substrates reported similar results as ours. The similarities between the results from devices on different substrates suggest that, at low temperatures, scattering in these systems with mobility 500-2000 cm^2/Vs is dominated by disorder-mediated electron-electron interactions, and not limited by substrates. Further studies are warranted to reveal scattering mechanisms in higher mobility samples.

Chapter 7

Conclusion and Outlook

In this thesis, I have presented our comprehensive electronic transport studies of high quality bi- and tetra-layer graphene devices as well as few-layer phosphorene (FLP) devices. Few-layer graphene with competing symmetries (valley, spin and orbital) still remains a fascinating platform to study the quantum Hall effect (QHE), allowing the observations of intricate quantum phases with transitions that can be tuned by a combination of electric and magnetic fields.

Its unique electronic properties make few-layer graphene an ideal platform to study the novel physical phenomena that are difficult to realize in conventional or semiconductor two-dimensional electron gas (2DEG) systems. One such phenomenon is the interplay between superconductivity (SC) and the QHE with the promise of realizing exotic topological states such as Majorana fermions [98–100]. For a 2DEG system in the quantum Hall (QH) regime, supercurrent can only flow along the edge states of the 2DEG. Due to the chiral nature, however, edge states with opposite momenta are located on the opposite

edges of the 2DEG system, and coupled by the unconventional Andreev bound states [98] at the QH/superconductors (SCs) interfaces. In classical physics picture, unconventional Andreev bound states can be viewed as alternative skipping orbits of electrons and holes. At a perfectly transparent QH/SCs interface, the bound states become a neutral mixture of electrons and holes, similar to the Majorana mode [98]. In conventional 2DEG systems, making transparent QH/SCs interfaces is challenging because the 2DEG is buried underneath the thick GaAs layers. Graphene is an ideal candidate for studying the interplay between SC and the QH states for the following reasons. Firstly, due to its gapless band structure, graphene can make good contacts to most metals including SCs, leading to high transparency at graphene/SCs interfaces. Secondly, hexagonal boron nitride (hBN) enables us to realize graphene devices with high mobility, hence to realize the QH states at lower magnetic field than the upper critical field of SCs. The fascinating physical properties of few-layer graphene have made graphene an ideal platform to explore novel quantum phases and topological states.

An unexpected application of graphene is making ohmic contacts to 2D semiconductors. For example, one of the bottlenecks in electronic and optoelectronic studies of transition metal dicalcogenides (TMD), such as MoS_2, WSe_2, is the formation of Schottky barriers at metal-TMD interfaces. A recent work shows that this problem can be partially solved by using graphene as contacts to TMD with tunable work function, allowing the observation of quantum oscillations in few-layer MoS_2 devices [101]. Thus graphene provides a route for tunable contacts to 2D semiconductors.

In addition to the QHE in few-layer graphene, we also reported weak localization in hBN-encapsulated FLP devices, and demonstrated that the dominant source of phase dephasing in FLP is the electron-electron interactions at low temperatures. However, since black phosphorus has a large lattice anisotropy [23, 102, 103], the dependence of scattering mechanisms on the crystallographic orientations still remains unclear. A recent work [104] reported that in FLP, the dephasing lengths' dependence on temperature is similar to that observed in quasi-one-dimensional systems such as carbon nanotubes. Therefore, the effects of large anisotropy on the scattering and dephasing mechanisms await further explorations. Moreover, it is also of significant interest to study the anisotropic QHE in FLP devices. The experiments so far were mostly focused on the FLP flakes $\sim 10-30$ nm thick. The quantum transport, including weak localization, Shubnikov-de Haas oscillation and the QHE, in very thin FLP flakes (down to monolayer) still needs further studies.

As discussed in the thesis, the magnetotransport study of two-dimensional (2D) materials has grown explosively in the past few years, and remains one of the most active frontiers in condensed matter research. The family of 2D materials has been growing almost continuously for the past seven years, and each new 2D material brings forth new physical properties that may be tuned by thickness, strain, electric and magnetic fields, etc. These exciting 2D materials provide the possibility of realizing novel phenomena such as 2D superconductivity and spin superfluid. Moreover, it would be interesting to combine different 2D materials to study novel physical phenomena, for example, the unconventional Andreev reflection between 2D superconductors and graphene.

Bibliography

[1] A.K. Geim and K.S. Novoselov. The rise of graphene (editorial). *Nat. Mat.*, 6:183, 2007.

[2] Mildred S Dresselhaus. Fifty years in studying carbon-based materials. *Physica Scripta*, 2012(T146):014002, 2012.

[3] K. S. Novoselov, A. K. Geim, S. V. Morozov, D. Jiang, Y. Zhang, S. V. Dubonos, I. V. Grigorieva, and A. A. Firsov. Electric field effect in atomically thin carbon films. *Science*, 306(5696):666–669, 2004.

[4] P. R. Wallace. The band theory of graphite. *Phys. Rev.*, 71:622–634, May 1947.

[5] Riichiro Saito, Gene Dresselhaus, and Mildred S Dresselhaus. *Physical Properties of Carbon Nanotubes*. World Scientific Publishing, 1998. ISBN 978-1-86094-093-4 (hb) ISBN 978-1-86094-223-5 (pb).

[6] S. Iijima et al. Helical microtubules of graphitic carbon. *Nature*, 354(6348):56–58, 1991.

[7] K. S. Novoselov, A. K. Geim, S. V. Morozov, D. Jiang, M. I. Katsnelson, I. V. Grigorieva, S. V. Dubonos, and A. A. Firsov. Two-dimensional gas of massless dirac fermions in graphene. *Nature*, 438(7065):197–200, 2005.

[8] Yuanbo Zhang, Yan-Wen Tan, Horst L. Stormer, and Philip Kim. Experimental observation of the quantum hall effect and berry's phase in graphene. *Nature*, 438:201–204, 2005.

[9] D. C. Tsui, H. L. Stormer, and A. C. Gossard. Two-dimensional magnetotransport in the extreme quantum limit. *Phys. Rev. Lett.*, 48:1559–1562, May 1982.

[10] Kirill I. Bolotin, Fereshte Ghahari, Michael D. Shulman, Horst L. Stormer, and Philip Kim. Observation of the fractional quantum hall effect in graphene. *Nature*, 462:196–199, 2009.

[11] Xu Du, Ivan Skachko1, Fabian Duerr1, Adina Luican, and Eva Y. Andrei. Fractional quantum hall effect and insulating phase of dirac electrons in graphene. *Nature*, 462, 192-195.

[12] R. R. Nair, P. Blake, A. N. Grigorenko, K. S. Novoselov, T. J. Booth, T. Stauber, N. M. R. Peres, and A. K. Geim. Fine structure constant defines visual transparency of graphene. *Science*, 320(5881):1308–1308, 2008.

[13] Changgu Lee, Xiaoding Wei, Jeffrey W. Kysar, and James Hone. Measurement of the elastic properties and intrinsic strength of monolayer graphene. *Science*, 321(5887):385–388, 2008.

[14] Alexander A. Balandin, Suchismita Ghosh, Wenzhong Bao, Irene Calizo, Desalegne Teweldebrhan, Feng Miao, and Chun Ning Lau. Superior thermal conductivity of single-layer graphene. *Nano Letters*, 8(3):902–907, 2008. PMID: 18284217.

[15] Kaili Li, Yijun Yu, Guo Jun Ye, Qingqin Ge, Xuedong Ou, Hua Wu, Donglai Feng, Xian Hui Chen, and Yuanbo Zhang. Black phosphorus field-effect transistors. *Nat. Nanotechnol.*, 9:372–377, 2014.

[16] B. Radisavljevic, A. Radenovic, J. Brivio, V. Giacometti, and A. Kis. Single-layer mos2 transistors. *Nat. Nanotechnol.*, 6:147–150, 20011.

[17] Yuichi Akahama, Shoichi Endo, and Shin ichiro Narita. Electrical properties of black phosphorus single crystals. *Journal of the Physical Society of Japan*, 52(6):2148–2155, 1983.

[18] Y. Maruyama, S. Suzuki, K. Kobayashi, and S. Tanuma. Synthesis and some properties of black phosphorus single crystals. *Physica B+C*, 105(1):99 – 102, 1981.

[19] Han Liu, Adam T. Neal, Zhen Zhu, Zhe Luo, Xianfan Xu, David Tomnek, and Peide D. Ye. Phosphorene: An unexplored 2d semiconductor with a high hole mobility. *ACS Nano*, 8(4):4033–4041, 2014. PMID: 24655084.

[20] Yanlan Du, Chuying Ouyang, Siqi Shi, and Minsheng Lei. Ab initio studies on atomic and electronic structures of black phosphorus. *Journal of Applied Physics*, 107(9), 2010.

[21] Robert W. Keyes. The electrical properties of black phosphorus. *Phys. Rev.*, 92:580–584, Nov 1953.

[22] Douglas Warschauer. Electrical and optical properties of crystalline black phosphorus. *Journal of Applied Physics*, 34(7):1853–1860, 1963.

[23] Tran Vy, Soklaski Ryan, Liang Yufeng, and Yang Li. Layer-controlled band gap and anisotropic excitons in few-layer black phosphorus. *Phys. Rev. B*, 89:235319, 2014.

[24] Fengnian Xia, Han Wang, and Yichen Jia. Rediscovering black phosphorus as an anisotropic layered material for optoelectronics and electronics. *Nat. Commun.*, 5(4485), 2014.

[25] Likai Li andFangyuan Yang andGuo Jun Ye, Zuocheng Zhang, Zengwei Zhu, Wenkai Lou, Xiaoying Zhou, Liang Li, Kenji Watanabe, Takashi Taniguchi, Kai Chang,

Yayu Wang andXian Hui Chen, and Yuanbo Zhang. Quantum hall effect in black phosphorus two-dimensional electron system. *Nat. Nanotechnol.*, 11(6):593–597, 2016.

[26] Qihang Liu, Xiuwen Zhang, L. B. Abdalla, Adalberto Fazzio, and Alex Zunger. Switching a normal insulator into a topological insulator via electric field with application to phosphorene. *Nano Letters*, 15(2):1222–1228, 2015. PMID: 25607525.

[27] Jimin Kim, Seung Su Baik, Sae Hee Ryu, Yeongsup Sohn, Soohyung Park, Byeong-Gyu Park, Jonathan Denlinger, Yeonjin Yi, Hyoung Joon Choi, and Keun Su Kim. Observation of tunable band gap and anisotropic dirac semimetal state in black phosphorus. *Science*, 349(6249):723–726, 2015.

[28] Nathaniel Gillgren, Darshana Wickramaratne, Yanmeng Shi, Tim Espiritu, Jiawei Yang, Jin Hu, Jiang Wei, Xue Liu, Zhiqiang Mao, Kenji Watanabe, Takashi Taniguchi, Marc Bockrath, Yafis Barlas, Roger K Lake, and Chun Ning Lau. Gate tunable quantum oscillations in air-stable and high mobility few-layer phosphorene heterostructures. *2D Materials*, 2(1):011001, 2015.

[29] Gen Long, Denis Maryenko, Junying Shen, Shuigang Xu, Jianqiang Hou, Zefei Wu, Wing Ki Wong, Tianyi Han, Jiangxiazi Lin, Yuan Cai, Rolf Lortz, and Ning Wang. Quantum hall effect in ultrahigh mobility two-dimensional hole gas of black phosphorus, 2015.

[30] N.W. Ashcroft and N.D. Mermin. *Solid State Physics*. Saunders College, Philadelphia, 1976.

[31] Edward McCann and Mikito Koshino. The electronic properties of bilayer graphene. *Reports on Progress in Physics*, 76(5):056503, 2013.

[32] Edward McCann. Asymmetry gap in the electronic band structure of bilayer graphene. *Phys. Rev. B*, 74:161403, Oct 2006.

[33] Anya L. Grushina, Dong-Keun Ki, Mikito Koshino, Aurelien A. L. Nicolet, Clment Faugeras, Edward McCann, Marek Potemski, and Alberto F. Morpurgo. Insulating state in tetralayers reveals an evenodd interaction effect in multilayer graphene. *Nat. Commun.*, 6(6419), 2015.

[34] Chun Hung Lui, Zhiqiang Li, Zheyuan Chen, Paul V. Klimov, Louis E. Brus, and Tony F. Heinz. Imaging stacking order in few-layer graphene. *Nano Letters*, 11(1):164–169, 2011. PMID: 21121668.

[35] Mikito Koshino and Edward McCann. Landau level spectra and the quantum hall effect of multilayer graphene. *Phys. Rev. B*, 83:165443, Apr 2011.

[36] Shinobu Hikami, Anatoly I. Larkin, and Yosuke Nagaoka. Spin-orbit interaction and magnetoresistance in the two dimensional random system. *Progress of Theoretical Physics*, 63(2):707–710, 1980.

[37] B L Altshuler, A G Aronov, and D E Khmelnitsky. Effects of electron-electron collisions with small energy transfers on quantum localisation. *Journal of Physics C: Solid State Physics*, 15(36):7367, 1982.

[38] G Bergmann. Weak localization in thin films. *Physica Scripta*, 1986(T14):99, 1986.

[39] Supriyo Datta. *Electronic Transport in Mesoscopic Systems*. Cambridge Studies in Semiconductor Physics and Microelectronic Engineering. Cambridge, 1995.

[40] K. v. Klitzing, G. Dorda, and M. Pepper. New method for high-accuracy determination of the fine-structure constant based on quantized hall resistance. *Phys. Rev. Lett.*, 45:494–497, Aug 1980.

[41] L. D. Landau. Zur Theorie der phasenumwandlungen II. *Phys. Z. Sowjetunion*, 11:26–35, 1937.

[42] K. S. Novoselov, E. McCann, S. V. Morozov, V. I. Fal'ko, M. I. Katsnelson, U. Zeitler, D. Jiang, F. Schedin1, and A. K. Geim. Unconventional quantum hall effect and berry's phase of 2π in bilayer graphene. *Nat. Phy.*, 2:177–180, 2006.

[43] Xu Du, Ivan Skachko, Anthony Barker1, and Eva Y. Andrei. Approaching ballistic transport in suspended graphene. *Nat. Nanotechnol.*, 3, 491495.

[44] C. R. Dean, A. F. Young, I. Meric, C. Lee, L. Wang, S. Sorgenfrei, K. Watanabe, T. Taniguchi, P. Kim, K. L. Shepard, and J. Hone. Boron nitride substrates for high-quality graphene electronics. *Nat. Nanotechnol.*, 5, 722726.

[45] L. Wang, I. Meric, P. Y. Huang, Q. Gao, Y. Gao, H. Tran, T. Taniguchi, K. Watanabe, L. M. Campos, D. A. Muller, J. Guo, P. Kim, J. Hone, K. L. Shepard, and C. R. Dean. One-dimensional electrical contact to a two-dimensional material. *Science*, 342(6158):614–617, 2013.

[46] K.I. Bolotin, K.J. Sikes, Z. Jiang, M. Klima, G. Fudenberg, J. Hone, P. Kim, and H.L. Stormer. Ultrahigh electron mobility in suspended graphene. *Solid State Communications*, 146(9-10):351 – 355, 2008.

[47] J. Moser, A. Barreiro, and A. Bachtold. Current-induced cleaning of graphene. *Applied Physics Letters*, 91(16), 2007.

[48] S. Das Sarma, Shaffique Adam, E. H. Hwang, and Enrico Rossi. Electronic transport in two-dimensional graphene. *Rev. Mod. Phys.*, 83:407–470, May 2011.

[49] Andrea C. Ferrari. Raman spectroscopy of graphene and graphite: Disorder, electronphonon coupling, doping and nonadiabatic effects. *Solid State Communications*, 143:47 – 57, 2007. Exploring grapheneRecent research advances.

[50] Gang Liu, Jairo Velasco Jr, Wenzhong Bao, and Chun Ning Lau. Fabrication of graphene p-n-p junctions with contactless top gates. *Applied Physics Letters*, 92(20), 2008.

[51] Lei Jing, Jairo Velasco Jr., Philip Kratz, Gang Liu, Wenzhong Bao, Marc Bockrath, and Chun Ning Lau. Quantum transport and field-induced insulating states in bilayer graphene pnp junctions. *Nano Letters*, 10(10):4000–4004, 2010. PMID: 20863070.

[52] J. Velasco Jr, L. Jing, W. Bao, Y. Lee, P. Kratz, V. Aji, M. Bockrath, C. N. Lau, C. Varma, R. Stillwell, D. Smirnov, Fan Zhang, J. Jung, and A. H. MacDonald. Transport spectroscopy of symmetry-broken insulating states in bilayer graphene. *Nat. Nanotechnol.*, 7:156160, 2011.

[53] Andres Castellanos-Gomez, Leonardo Vicarelli, Elsa Prada, Joshua O Island, K L Narasimha-Acharya, Sofya I Blanter, Dirk J Groenendijk, Michele Buscema, Gary A Steele, J V Alvarez, Henny W Zandbergen, J J Palacios, and Herre S J van der Zant. Isolation and characterization of few-layer black phosphorus. *2D Materials*, 1(2):025001, 2014.

[54] Yanmeng Shi, Nathaniel Gillgren, Timothy Espiritu, Son Tran, Jiawei Yang, Kenji Watanabe, Takahashi Taniguchi, and Chun Ning Lau. Weak localization and electron-electron interactions in few layer black phosphorus devices. *2D Materials*, 3(3):034003, 2016.

[55] Joshua O Island, Gary A Steele, Herre S J van der Zant, and Andres Castellanos-Gomez. Environmental instability of few-layer black phosphorus. *2D Materials*, 2(1):011002, 2015.

[56] Xiaomu Wang, Aaron M. Jones, Kyle L. Seyler, Vy Tran, Yichen Jia, Huan Zhao, Han Wang, Li Yang, Xiaodong Xu, and Fengnian Xia. Transport spectroscopy of symmetry-broken insulating states in bilayer graphene. *Nat. Nanotechnol.*, 10:517521, 2015.

[57] Hui Zhu, Stephen McDonnell, Xiaoye Qin, Angelica Azcatl, Lanxia Cheng, Rafik Addou, Jiyoung Kim, Peide D. Ye, and Robert M. Wallace. Al2o3 on black phosphorus by atomic layer deposition: An in situ interface study. *ACS Applied Materials & Interfaces*, 7(23):13038–13043, 2015. PMID: 26016806.

[58] Yongjin Lee, Jairo Velasco, David Tran, Fan Zhang, W. Bao, Lei Jing, Kevin Myhro, Dmitry Smirnov, and Chun Ning Lau. Broken symmetry quantum hall states in dual-gated aba trilayer graphene. *Nano Letters*, 13(4):1627–1631, 2013. PMID: 23527578.

[59] Petr Stepanov, Yafis Barlas, Tim Espiritu, Shi Che, Kenji Watanabe, Takashi Taniguchi, Dmitry Smirnov, and Chun Ning Lau. Tunable symmetries of integer and fractional quantum hall phases in heterostructures with multiple dirac bands. *Phys. Rev. Lett.*, 117:076807, Aug 2016.

[60] Eduardo V. Castro, K. S. Novoselov, S. V. Morozov, N. M. R. Peres, J. M. B. Lopes dos Santos, Johan Nilsson, F. Guinea, A. K. Geim, and A. H. Castro Neto. Biased bilayer graphene: Semiconductor with a gap tunable by the electric field effect. *Phys. Rev. Lett.*, 99:216802, Nov 2007.

[61] Yanmeng Shi, Yongjin Lee, Shi Che, Ziqi Pi, Timothy Espiritu, Petr Stepanov, Dmitry Smirnov, Chun Ning Lau, and Fan Zhang. Energy gaps and layer polarization of integer and fractional quantum hall states in bilayer graphene. *Phys. Rev. Lett.*, 116:056601, Feb 2016.

[62] Jeroen B. Oostinga, Hubert B. Heersche, Xinglan Liu, Alberto F. Morpurgo, and Lieven M. K. Vandersypen. Gate-induced insulating state in bilayer graphene devices. *Nat. Mater.*, 7:151157, 2007.

[63] A. B. Kuzmenko, I. Crassee, D. van der Marel, P. Blake, and K. S. Novoselov. Determination of the gate-tunable band gap and tight-binding parameters in bilayer graphene using infrared spectroscopy. *Phys. Rev. B*, 80:165406, Oct 2009.

[64] Wenzhong Bao, Jairo Velasco, Fan Zhang, Lei Jing, Brian Standley, Dmitry Smirnov, Marc Bockrath, Allan H. MacDonald, and Chun Ning Lau. Evidence for a spontaneous gapped state in ultraclean bilayer graphene. *Proceedings of the National Academy of Sciences*, 109(27):10802–10805, 2012.

[65] Kin Fai Mak, Chun Hung Lui, Jie Shan, and Tony F. Heinz. Observation of an electric-field-induced band gap in bilayer graphene by infrared spectroscopy. *Phys. Rev. Lett.*, 102:256405, Jun 2009.

[66] Yuanbo Zhang, Tsung-Ta Tang, Caglar Girit, Zhao Hao, Michael C. Martin, Alex Zettl, Michael F. Crommie, Y. Ron Shen, and Feng Wang. Direct observation of a widely tunable bandgap in bilayer graphene. *Nature*, 459:820823, 2009.

[67] Fengnian Xia, Damon B. Farmer, Yu-ming Lin, and Phaedon Avouris. Graphene field-effect transistors with high on/off current ratio and large transport band gap at room temperature. *Nano Letters*, 10(2):715–718, 2010. PMID: 20092332.

[68] Thiti Taychatanapat and Pablo Jarillo-Herrero. Electronic transport in dual-gated bilayer graphene at large displacement fields. *Phys. Rev. Lett.*, 105:166601, Oct 2010.

[69] K. Zou and J. Zhu. Transport in gapped bilayer graphene: The role of potential fluctuations. *Phys. Rev. B*, 82:081407, Aug 2010.

[70] A. F. Young, C. R. Dean, I. Meric, S. Sorgenfrei, H. Ren, K. Watanabe, T. Taniguchi, J. Hone, K. L. Shepard, and P. Kim. Electronic compressibility of layer-polarized bilayer graphene. *Phys. Rev. B*, 85:235458, Jun 2012.

[71] R. T. Weitz, M. T. Allen, B. E. Feldman, J. Martin, and A. Yacoby. Broken-symmetry states in doubly gated suspended bilayer graphene. *Science*, 330(6005):812–816, 2010.

[72] J. Velasco Jr, Y. Lee, Z. Zhao, Lei Jing, P. Kratz, Marc Bockrath, and C. N. Lau. Transport measurement of landau level gaps in bilayer graphene with layer polarization control. *Nano Letters*, 14(3):1324–1328, 2014.

[73] Benjamin E. Feldman, Jens Martin, and Amir Yacoby. Broken-symmetry states and divergent resistance in suspended bilayer graphene. *Nat. Phys.*, 5, 889893.

[74] Wenzhong Bao, Zeng Zhao, Hang Zhang, Gang Liu, Philip Kratz, Lei Jing, Jairo Velasco, Dmitry Smirnov, and Chun Ning Lau. Magnetoconductance oscillations and evidence for fractional quantum hall states in suspended bilayer and trilayer graphene. *Phys. Rev. Lett.*, 105:246601, Dec 2010.

[75] A. Kou, B. E. Feldman, A. J. Levin, B. I. Halperin, K. Watanabe, T. Taniguchi, and A. Yacoby. Electron-hole asymmetric integer and fractional quantum hall effect in bilayer graphene. *Science*, 345(6192):55–57, 2014.

[76] Patrick Maher, Lei Wang, Yuanda Gao, Carlos Forsythe, Takashi Taniguchi, Kenji Watanabe, Dmitry Abanin, Zlatko Papić, Paul Cadden-Zimansky, James Hone, Philip Kim, and Cory R. Dean. Tunable fractional quantum hall phases in bilayer graphene. *Science*, 345(6192):61–64, 2014.

[77] Dong-Keun Ki, Vladimir I. Falko, Dmitry A. Abanin, and Alberto F. Morpurgo. Observation of even denominator fractional quantum hall effect in suspended bilayer graphene. *Nano Letters*, 14(4):2135–2139, 2014.

[78] Kayoung Lee, Babak Fallahazad, Jiamin Xue, David C. Dillen, Kyounghwan Kim, Takashi Taniguchi, Kenji Watanabe, and Emanuel Tutuc. Chemical potential and quantum hall ferromagnetism in bilayer graphene. *Science*, 345(6192):58–61, 2014.

[79] J. Martin, B. E. Feldman, R. T. Weitz, M. T. Allen, and A. Yacoby. Local compressibility measurements of correlated states in suspended bilayer graphene. *Phys. Rev. Lett.*, 105:256806, Dec 2010.

[80] Y. Zhao, P. Cadden-Zimansky, Z. Jiang, and P. Kim. Symmetry breaking in the zero-energy landau level in bilayer graphene. *Phys. Rev. Lett.*, 104:066801, Feb 2010.

[81] H. J. van Elferen, A. Veligura, E. V. Kurganova, U. Zeitler, J. C. Maan, N. Tombros, I. J. Vera-Marun, and B. J. van Wees. Field-induced quantum hall ferromagnetism in suspended bilayer graphene. *Phys. Rev. B*, 85:115408, Mar 2012.

[82] Z. Jiang, Y. Zhang, H. L. Stormer, and P. Kim. Quantum hall states near the charge-neutral dirac point in graphene. *Phys. Rev. Lett.*, 99:106802, Sep 2007.

[83] Jairo Velasco Jr, Yongjin Lee, Kevin Zhang, Fan andMyhro, David Tran, Michael Deo, Dmitry Smirnov, Allan MacDonald, and Chun Ning Lau. Competing ordered states with filling factor two in bilayer graphene. *Nature Communications*, 4(4550), 2014.

[84] E. V. Gorbar, V. P. Gusynin, Junji Jia, and V. A. Miransky. Broken-symmetry states and phase diagram of the lowest landau level in bilayer graphene. *Phys. Rev. B*, 84:235449, Dec 2011.

[85] E. V. Gorbar, V. P. Gusynin, V. A. Miransky, and I. A. Shovkovy. Coexistence and competition of nematic and gapped states in bilayer graphene. *Phys. Rev. B*, 86:125439, Sep 2012.

[86] J. Lambert and R. Côté. Quantum hall ferromagnetic phases in the landau level $n = 0$ of a graphene bilayer. *Phys. Rev. B*, 87:115415, Mar 2013.

[87] Yafis Barlas, R. Côté, K. Nomura, and A. H. MacDonald. Intra-landau-level cyclotron resonance in bilayer graphene. *Phys. Rev. Lett.*, 101:097601, Aug 2008.

[88] Fan Zhang, Jeil Jung, Gregory A. Fiete, Qian Niu, and Allan H. MacDonald. Spontaneous quantum hall states in chirally stacked few-layer graphene systems. *Phys. Rev. Lett.*, 106:156801, Apr 2011.

[89] Z. Papić and D. A. Abanin. Topological phases in the zeroth landau level of bilayer graphene. *Phys. Rev. Lett.*, 112:046602, Jan 2014.

[90] Youngwook Kim, Dong Su Lee, Suyong Jung, Viera Skkalov, T. Taniguchi, K. Watanabe, Jun Sung Kim, and Jurgen H. Smet. Fractional quantum hall states in bilayer graphene probed by transconductance fluctuations. *Nano Letters*, 15(11):7445–7451, 2015.

[91] Y. Lee, D. Tran, K. Myhro, J. Velasco, N. Gillgren, C. N. Lau, Y. Barlas, J. M. Poumirol, D. Smirnov, and F. Guinea. Competition between spontaneous symmetry breaking and single-particle gaps in trilayer graphene. *Nat. Commun.*, 5, 2014.

[92] I. M. Lifshitz. Anomalies of electron characteristics of a metal in the high pressure region. *Soviet Physics JEPT*, 11(5):1130–1135, November 1960.

[93] A. A. Avetisyan, B. Partoens, and F. M. Peeters. Stacking order dependent electric field tuning of the band gap in graphene multilayers. *Phys. Rev. B*, 81:115432, Mar 2010.

[94] Tsuneya Ando, Alan B. Fowler, and Frank Stern. Electronic properties of two-dimensional systems. *Rev. Mod. Phys.*, 54:437–672, Apr 1982.

[95] G Bergmann. Weak localization in thin films. *Physica Scripta*, 1986(T14):99, 1986.

[96] Hidetoshi Fukuyama and Elihu Abrahams. Inelastic scattering time in two-dimensional disordered metals. *Phys. Rev. B*, 27:5976–5980, May 1983.

[97] Yuchen Du, Adam T Neal, Hong Zhou, and Peide D Ye. Weak localization in few-layer black phosphorus. *2D Materials*, 3(2):024003, 2016.

[98] F. Amet, C. T. Ke, I. V. Borzenets, J. Wang, K. Watanabe, T. Taniguchi, R. S. Deacon, M. Yamamoto, Y. Bomze, S. Tarucha, and G. Finkelstein. Supercurrent in the quantum hall regime. *Science*, 352(6288):966–969, 2016.

[99] Peter Rickhaus, Markus Weiss, Laurent Marot, and Christian Schnenberger. Quantum hall effect in graphene with superconducting electrodes. *Nano Letters*, 12(4):1942–1945, 2012. PMID: 22417183.

[100] Gil-Ho Lee, Ko-Fan Huang, Dmitri K. Efetov, Di S. Wei, Sean Hart, Takashi Taniguchi, Kenji Watanabe, Amir Yacoby, and Philip Kim. Inducing superconducting correlation in quantum hall edge states, 2016.

[101] Xu Cui, Gwan-Hyoung Lee, Young Duck Kim, Ghidewon Arefe, Pinshane Y. Huang, Chul-Ho Lee, Daniel A. Chenet, Xian Zhang, Lei Wang, Fan Ye, Filippo Pizzocchero, Bjarke S. Jessen, Kenji Watanabe, Takashi Taniguchi, David A. Muller, Tony Low, Philip Kim, and James Hone. Multi-terminal transport measurements of mos2 using a van der waals heterostructure device platform. *Nat. Nanotechnol.*, 10:534–540, 2015.

[102] Jingsi Qiao, Xianghua Kong, Zhi-Xin Hu, Feng Yang, and Wei Ji. High-mobility transport anisotropy and linear dichroism in few-layer black phosphorus. *Nat. Commun.*, 5(4475), 2014.

[103] Zhenghe Jin, Jeffrey T. Mullen, and Ki Wook Kim. Highly anisotropic electronic transport properties of monolayer and bilayer phosphorene from first principles. *Applied Physics Letters*, 109(5), 2016.

[104] N. Hemsworth, V. Tayari, F. Telesio, S. Xiang, S. Roddaro, M. Caporali, A. Ienco, M. Serrano-Ruiz, M. Peruzzini, G. Gervais, T. Szkopek, and S. Heun. Dephasing in strongly anisotropic black phosphorus. *Phys. Rev. B*, 94:245404, Dec 2016.